Measurement of Soil in Sugar Cane Using Non-destructive Techniques

by

Thavashen Padayachee

A dissertation submitted in fulfilment of the
academic requirements for the degree of
Master of Science
in the
School of Pure and Applied Physics
University of Natal
Durban

December 2001

For my family

Preface

The experimental work described herein was carried out in the Applied Physics Group, School of Pure and Applied Physics, University of Natal, Durban from January 2000 to December 2001, under the supervision of Professor Michael J. Alport.

This study represents original work by the author and has not been submitted in any form to another university or institution. Where use was made of the work of others, it has been duly acknowledged in the text.

Acknowledgements

Abstract

The soil being delivered with sugar cane consignments, from the cane fields to the factories, has been a recent cause for concern in the South African sugar industry. The soil impurities increase the wear of processing machinery, reduce extraction efficiency, and represents an unnecessary transport of material. The cost due to soil was estimated at R63 million (about US$ 8 million) over the 1996/97-season. The need to reduce costs, due to the unwanted soil component, has been given a high priority.

Ashing is currently used by the sugar industry to estimate the amount of soil in cane. Although simple to implement, the method is destructive, requires long processing times and limited to small sample sizes.

In recent times, non-destructive techniques have become more prominent in industry. Hence, the decision to apply such techniques to the soil in cane-problem. This dissertation describes an experimental investigation into *Dual-Energy Transmission (DuET)* and *X-ray Imaging* for quantifying the amount of soil in cane.

DuET can determine the relative concentrations of the components of a binary mixture by measuring the transmission of low- and high-energy gamma photons through the mixture. The principle of *DuET* was successfully demonstrated with aqueous solutions of ferric chloride. Experimentally-determined mass attenuation coefficients of water and ferric chloride were compared to theoretical values. *DuET* was then applied to dried, shredded sugar cane spiked with various amounts of soil. Results showed large variations in the predicted soil concentrations. These variations

were attributed to radiation scatter and incomplete volume sampling by the radioactive source. However, new experimental arrangements are expected to improve the technique: initial test results are given of a sample holder that continuously rotates a sample up and down through the source-detector axis.

An alternative approach to processing *DuET*-spectra, using the discrete wavelet transform coupled with an artificial neural network, is also introduced.

X-ray Imaging was the second technique investigated. A literature survey revealed that this technique had not previously been applied to the soil in cane-problem. The present work constituted an initial investigation to determine the feasibility of applying X-ray imaging to measure the amount of soil in cane. The soil/cane-samples, that were used for *DuET*, were imaged using a commercial mammography unit, and the resulting radiographs were analysed using image processing techniques. Although the results are promising, a more comprehensive investigation is foreseen.

Table of Contents

List of Acronyms and Abbreviations

ADC	Analog-to-Digital Converter
ANN	Artificial Neural Network
cps	Counts per second
DuET	Dual-Energy Transmission
DWT	Discrete Wavelet Transform
EDS	Energy-Dispersive Spectroscopy
IDL	Integrated Data Language
INAA	Instrumental Neutron Activation Analysis
max	Maximum
MCA	Multichannel Analyser
min	Minimum
MLP	Multi-layer perceptron
MSE	Mean squared error
NECSA	Nuclear Energy Corporation of South Africa
PMT	Photomultiplier Tube
ROI	Region-of-interest
SEM	Scanning Electron Microscope
SMRI	Sugar Milling Research Institute
UND	University of Natal (Durban)
WCM	Wavelet Coefficient Matrix
XCT	X-ray Computed Tomography
XRF	X-ray Fluorescence

List of Symbols

Z	Atomic number
τ	Probability per unit length for photoelectric absorption
σ_c	Probability per unit length for Compton scattering
κ	Probability per unit length for pair production
μ'	Linear attenuation coefficient
μ	Mass attenuation coefficient
ρ	Density of medium
B	Build-up factor
t_I	Integration time
$\overline{x}$	Mean value of quantity, x
M	True mean of population
s^2	Variance of sample
s	Standard deviation of sample
σ^2	Variance of population
σ	Standard deviation of population
σ_X	Error in quantity, X
$\Re^2$	Square of the correlation coefficient
L_0	Counts recorded by detector for unattenuated low-energy beam
H_0	Counts recorded by detector for unattenuated high-energy beam
L	Counts recorded by detector for transmitted low-energy beam through sample
H	Counts recorded by detector for transmitted high-energy beam through sample
μ_L	Mass attenuation coefficient at low-energy
μ_H	Mass attenuation coefficient at high-energy
R	Ratio of μ_L to μ_H
σ_R	Error in R
$[A]$	Percentage concentration of material A
r	Relative error (fractional standard deviation)
x	Independent variable of model
y	Dependent variable of model
a, b, c, c_0, c_1	Fitting parameters used by various models
$\lvert x \rvert$	Absolute value of x
I_p	Integrated pixel intensity

Outline of Dissertation

This dissertation describes an experimental investigation of non-destructive techniques for determining the amount of soil in sugar cane. The work focussed on *Dual-Energy Transmission (DuET)*[1] and *X-ray Imaging*.

Chapter 1 begins with a brief overview of the South African sugar industry, followed by a description of the soil in cane-problem and its impact on the sugar industry. Since this problem is not restricted to the South African sugar industry, also included is an overview of international efforts into investigating solutions to the problem. Brief introductions to *DuET* and X-ray imaging, and their applications are given.

Chapter 2 provides background theory to the concepts that are used in this work: interaction of gamma rays with matter, attenuation of gamma rays, gamma spectroscopy, and counting statistics and error propagation. The chapter concludes with theory to obtain the relative concentrations of the components of a binary mixture from a *DuET*-measurement.

Chapter 3 describes the soil- and sugar cane-samples that were used for this work.

Chapter 4 presents results of the elemental analysis of four soil-types and sugar cane using *Energy Dispersive Spectroscopy*. Differences in elemental composition between soil and cane would, in general, enhance the capabilities of *DuET* and X-ray imaging.

Chapter 5 describes the experimental investigation of the soil in cane-problem using *DuET*. The principle of *DuET* is demonstrated using aqueous solutions of various concentrations of ferric chloride. The technique was then applied to binary mixtures of soil and dried, shredded sugar cane. A method of scanning the entire sample volume is proposed; initial results are presented.

---

[1] http://www.scantech.com.au/tech/tet/default.htm

Chapter 6 presents an alternative to conventional peak-fitting for analysing *DuET*-spectra through the use of the *Discrete Wavelet Transform* (*DWT*) and *Artificial Neural Networks* (*ANN*s). Brief descriptions of the *DWT* and *ANN*s are provided. This method was used to determine the concentration of ferric chloride in aqueous solutions using the *DuET*-spectra recorded in **Chapter 5**. In addition, the method was applied to *DuET*-spectra of the soil in cane-samples. Comparisons of the results of the *DWT-ANN* method with standard regression are given.

Chapter 7 describes the application of X-ray imaging to the soil in cane-problem. The soil/cane-samples, that were analysed with *DuET*, were used for this study.

Chapter 8 presents results of the ashing of the samples that were used for *DuET* and X-ray imaging.

Chapter 9 summarises the results of this investigation. Areas requiring further work are also listed.

1. Introduction

1.1. The South African Sugar Industry

South Africa is one of the world's leading producers of sugar[2]. The sugar industry combines the agricultural task of sugar cane cultivation with the factory activity of producing raw and refined sugar, syrups, specialised sugars and other by-products.

An average of about 2.5 million tons of sugar is produced per season. About half of this sugar is marketed in Southern Africa, and the remainder is exported to markets in other parts of Africa, North America, the Middle East and Asia.[1]

Over the 1999/2000 financial year, it was estimated that the South African sugar industry contributed R1.3 billion (about US$ 0.16 billion, assuming R8/$US) to the country's foreign exchange earnings (based on actual sales and selling prices).[1]

The South African sugar industry is an important contributor to the national economy considering its agricultural and industrial investments, foreign exchange earnings, low import cost-component, its high employment and its ties with major suppliers, support industries and customers. Therefore, any identified problem affects the sugar industry and the whole country.

---

[2] The University of Natal is uniquely situated in KwaZulu-Natal, which is the main sugar cane growing province in South Africa.

1.2. The Soil in Cane-Problem

1.2.1. Overview of the Problem

The South African sugar industry has identified a major problem: the soil that is delivered with the sugar cane consignments is having a negative impact on the industry. The problem is, however, a global one. The sugar industries of Brazil and Australia have already invested much effort into investigating the problem. Any effort is justified in light of the loss in revenue due to the soil. The soil impurities increase the wear of processing machinery, reduce extraction efficiency, and result in the unnecessary transport of material to and from the mills[2].

Over the 1996/97-season, it was estimated that approximately 250,000 tons of soil were delivered with cane to South African sugar factories. This amount of material requires an additional 12,500 twenty-ton truckloads for delivery to the factories. The soil served no positive function and ended up with the waste products, which would have required another 12,500 twenty-ton truckloads for transport out of the factory.[2]

Over the years, the amount of soil in cane has been increasing. This has been attributed to the change in harvesting practices from manual to mechanical. **Figure 1** shows the amount of soil delivered to South African sugar cane factories from 1979 to 1996.

For the 1996/97-season, the South African industrial average value for soil in cane was about 1.19 %. However, on a monthly basis, much higher soil levels were found during the rainy season, with a maximum of 2.11 % in January 1997. The seasonal average for individual factories varied between 0.53 % and 2.22 %. Occasionally, soil levels as high as 20 % were measured from individual consignments.[2]

Direct and indirect costs due to the soil were estimated at R63 million (about US$ 8 million) over the 1996/97-season in South Africa.[2]

2
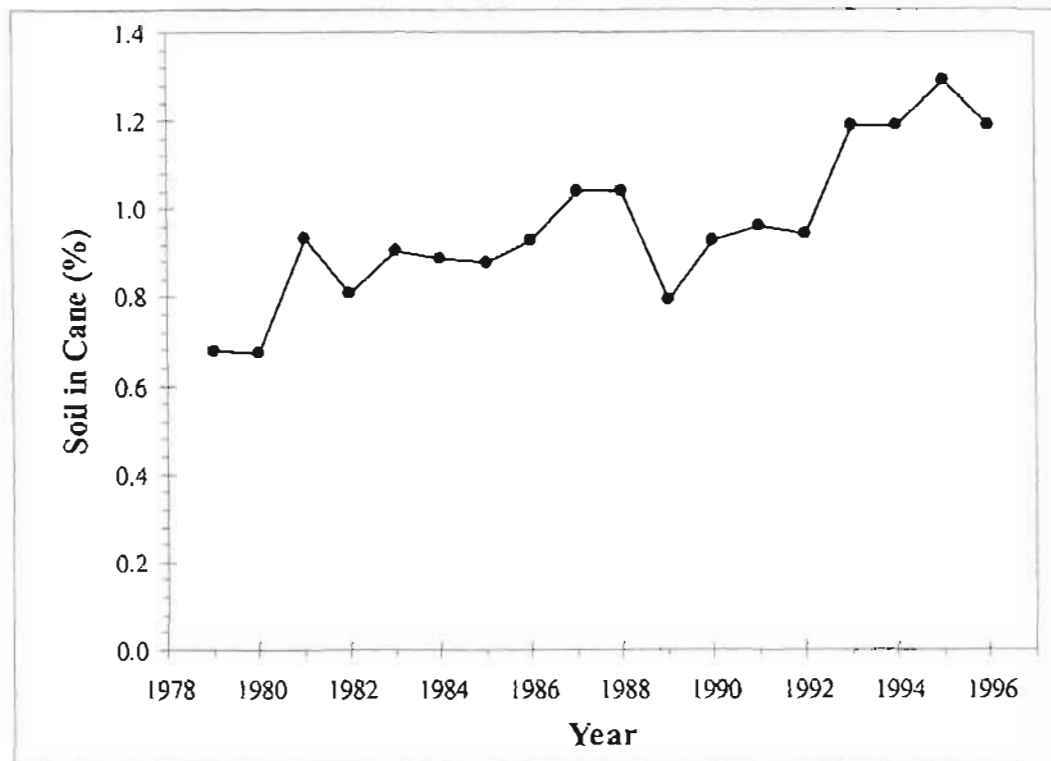
Figure 1: Percentage soil concentration delivered with sugar cane to South African factories from 1979 to 1996.[1] The amount of soil has been steadily increasing with time, and is attributed to the change in harvesting practices from manual to mechanical.

1.2.2. Harvesting and Loading of Sugar Cane

In South Africa, harvesting mostly involves manual cutting of the cane in the fields. Thereafter, the cane is usually laid in rows on the ground, where the tops of the stalks are removed. The cane is then piled into a bundle by a mobile hydraulic grab, driving along the rows, and in so doing also scoops up soil.[2]

1.2.3. The Source of the Soil

There are two distinct forms in which the soil arrives with the cane at the factory.

The first form is fine sand adhering to the cane stalks. This situation is, however, aggravated by rain or flooding, dependent upon soil-type and almost impossible to avoid.

The second form is loose soil that is collected with the cane from the fields (§1.2.2), and is, to some extent, avoidable since it is mainly influenced by harvesting practices.

3

1.2.4. The Effect of Soil on Factory Equipment and Processes

In the sugar cane factory, the soil has a negative effect on the various processes such as cane preparation, diffusion, milling, clarification, filtration and steam generation. Soil is directly responsible for the severe wear on a significant number of components (for example, the cane knives).[2]

In summary, the unwanted influence of soil on factory equipment and processes can be divided into four categories[2]:

1. it causes excessive wear of processing equipment;
2. it leads to an increase in sucrose loss, which translates to a loss in revenue;
3. it decreases factory efficiency due to choking of the chutes and breakdowns;
4. it requires additional equipment and/or processes, which would otherwise not be necessary.

1.2.5. Soil Removal Systems

The best method of reducing soil in cane is by avoiding the collection of soil during harvesting and loading, that is, by leaving the soil in the fields. However, some soil will always be associated with cane, especially during rainy periods.[2]

Dry cleaning methods remove only loose soil. These methods are quite ineffective during wet periods when more soil particles adhere to the cane. Wet cleaning during rainy periods is necessary but is expensive and sucrose losses are high.[2]

1.2.6. Ashing

The technique, currently applied by South African sugar factories to estimate soil in cane, is the *Ashing Method* (see **Appendix A** for details). A small sample of the cane consignment is incinerated in an oven. The mass of the residue, termed *ash*, is then expressed as a percentage of the original sample mass; this resulting quantity is termed *total ash*, and gives an indication of the soil content of the sample.

4

The total ash content of delivered cane is used as an incentive to farmers to provide clean cane – the less the total ash concentration, the greater the monetary value of the bonus given to the farmer.[3]

Although ashing is accepted as a method to estimate soil content, it has problems associated with long processing times and sampling issues. Therefore, any successor to ashing must obtain comparable results in a shorter period of time.

Implementing ashing measurements in the South African factories is also not simple due to lack of manpower or facilities. Therefore, ashing is not performed equally frequently at all the factories – some factories ash samples more periodically than others. This prevents reasonable comparison of results across factories.

In addition, the measurement of the total ash content requires a knowledge of or an assumption of a multitude of factors including delivered cane tonnage, cane variety, location, time of year and rainfall levels. Therefore, estimating the soil concentration from the ash content cannot be reliably accomplished since all the variables must be separately identified and handled accordingly. A soil monitoring device, that uses a technique independent of the above-mentioned factors, will facilitate quantifying soil in cane. This would provide a standard means of determining soil concentration which can be used by all factories.

1.2.7. Requirements of a Soil Monitor

The ideal soil monitoring device should be able to determine the soil content of an entire sugar cane consignment before the cane is processed by the factories. The amount of cane in each consignment can then be determined, and the farmers remunerated accordingly. Such a system should be:

1. Non-destructive (the cane must not be altered in a way that reduces its grade)
2. On-line (cane consignment must be analysed for soil before being processed)
3. Fast
4. Accurate
5. Low-cost (including capital and maintenance costs).

---

[3] Private communication: Solly Archary, *SMRI*

5

Although the ideal situation would demand a measuring apparatus that is auditable so that financial penalties can be levied, some Australian mills have found that the monitoring function alone acts as an effective deterrent to cane farmers to exercise more diligence during harvesting.[4]

1.3. Overview of International Efforts into the Soil in Cane-Problem

The problem of soil in cane is not localised to South Africa. Brazil and Australia have already realised the negative impact of soil on their industries, and are investing much effort into minimising its effects. Soil in sugar cane is estimated to cost the Australian sugar cane industry more than $30 million a year[3], and as a reminder, the cost estimate for the South African industry over the 1996/97-season was R63 million (about US$ 8 million).

The various methods, being used or considered to quantify the amount of soil in delivered cane, are described below.

1.3.1. Visual Examination

This method, usually applied in Australian mills, involves visual inspection of the consignments. It is, however, subjective and prone to large errors.[4]

1.3.2. Weighing impurities

The Brazilian method of direct determination by weighing impurities after manual separation from large samples (~500 kg) was reported to be very accurate. The method does not exhibit sample heterogeneity-problems but is "time-consuming and laborious".[4]

1.3.3. Natural Radioactivity of Soil

By utilising the fact that soil has a higher content of natural radionuclides (thorium, uranium and potassium) than sugar cane, soil monitors were developed by the *CSIRO* in Australia[3]. Field trials of this device at Tully Mill in Queensland, Australia have

---

[4] Private communication: James Asbury, *Scantech Limited*, j.asbury@scantech.com.au

shown that the soil content of sugar cane were obtained with a 0.4 % average deviation for soil concentrations between 0.6 % and 6.0 %. Further investigation of this technique is described in [4].

1.3.4. Scandium as a Soil Tracer

The use of scandium (*Sc*) as a soil tracer is described in [5]. The concentration of *Sc* in soil- and cane-samples were obtained via *Instrumental Neutron Activation Analysis* (*INAA*): samples were irradiated by neutrons in a reactor, and the induced sample radioactivity was measured. This method was described as being more accurate than ashing but was not quantified.

Concern over sampling was expressed in [5]. Cane samples were extracted from various points from a 14-ton truckload. However, there was a large spread in the amount of soil determined across the samples. Basically, if a technique that provides accurate determination of soil in cane has been identified, then the only limitation is the manner in which the truckloads are sampled (unless a means of analysing the entire truckload quickly is developed).

1.3.5. Silicon as a Soil Tracer

INAA can also be used to take advantage of the *Si*-content of soil using the nuclear reaction[6]

$$^{28}Si\ (n,\ p)\ ^{28}Al. \tag{1}$$

The sample is irradiated with neutrons. After a ^{28}Si-atom (of soil) captures a neutron, it is transformed to radioactive ^{28}Al, which has a half-life of 2.3 minutes. The consequent decay of ^{28}Al results in the emission of a 1.78 MeV-gamma ray and a stable ^{28}Si-nucleus. By counting the number of emitted gamma rays (with the aid of a gamma-spectroscopy unit, described under §2.3), the concentration of *Si*, and consequently the soil content, can be deduced. The half-life of the reaction is relatively short (2.3 minutes) so results can be obtained fairly quickly.

An implementation of *INAA* requires access to a nuclear reactor, which is clearly impractical for an on-line application. An alternative would be to use commercially-available and more portable neutron sources, for example, *Am / Be* or ^{252}Cf.

1.3.6. Soil Tracers determined via X-ray Fluorescence

The non-destructive analytical technique of *Energy Dispersive X-ray Fluorescence (ED-XRF)* was applied to determine the relative concentrations of *Al, Fe, Si, Ti* and *Zr* in soils from a sugar cane growing region[7]. It was discovered that the above-mentioned elements appear in much higher concentrations in the soils than in sugar cane.

1.4. Dual-Energy Transmission

Dual-Energy Transmission (DuET) was one of the techniques investigated for the soil in cane-problem for the present work. Low- and high-energy gamma beams are transmitted through a *binary* mixture, and the transmitted photons are counted by an energy-sensitive detector. Then, by comparing the transmitted counts to that recorded in the absence of the sample, the relative concentrations of the components of the mixture are obtained. The principle of *DuET* is depicted in **Figure 2** below. For the soil in cane-problem, the binary mixture is composed of soil particles embedded in sugar cane. The theory, to obtain the relative concentrations of the components of a binary mixture, is developed in §2.5.

The *DuET*-technique has been applied to a wide variety of industrial problems. It is most prominently used commercially in the coal industry, where it is used to measure the ash content of coal[8]-[10]. These *DuET*-systems usually employ the 60 keV and 662 keV gamma-lines of ^{241}Am and ^{137}Cs, respectively, for the low- and high-energy beams.

DuET was used as a non-destructive method to obtain the purity of gold alloys[11]. A variant of *DuET* using three gamma lines is also described in [11]. This technique can be used to determine the relative concentrations of the constituents of a three-component mixture. The multi-gamma emitter, ^{152}Eu, was used.

In [12], dual-energy transmission using gamma rays was compared to simultaneous neutron/gamma ray transmission to estimate the wool yield of raw wool. *DuET* is reported to be superior to the neutron/gamma-method.

Transmitted low-energy beam, L Transmitted high-energy beam, H

Material 1   Material 2

Incident low-energy beam, L_0 Incident high-energy beam, H_0

Radioactive source
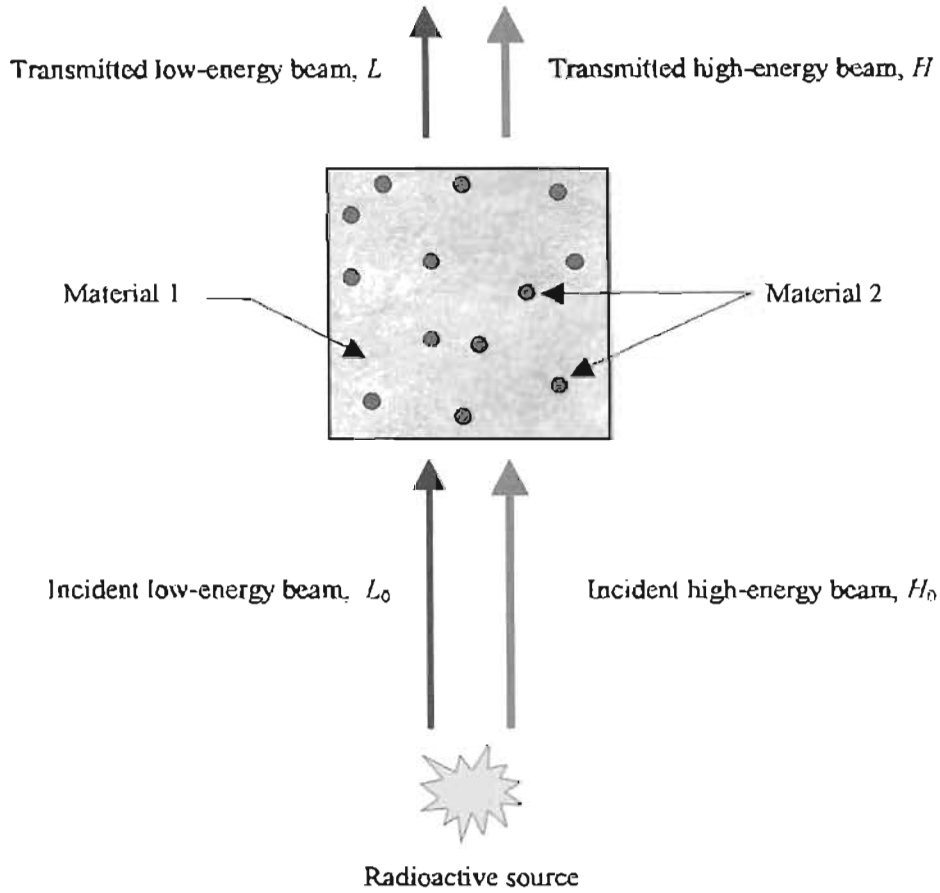
Figure 2: Principle of *DuET*. The low- and high-energy beams are transmitted through the binary mixture, and counted by an energy-sensitive detector. The relative concentrations of the two components can thereafter be determined.

The technique of *Dual-energy X-Ray Absorptiometry* (*DXA*), with two X-ray beams of different energies, has been developed to estimate the mass and density of bone. *DXA* enables physicians to track diseases that deteriorate bone tissue (for example, osteoporosis). Some *DXA*-images[13] are shown in **Figure 3** below.

(a)   *(b)*
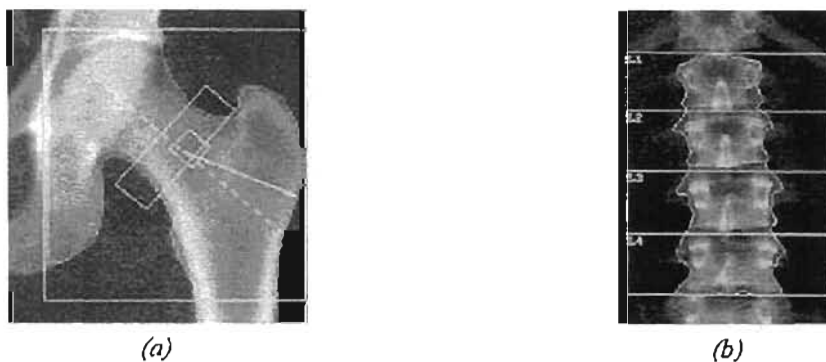
Figure 3: *DXA*-images of *(a)* the hip, and *(b)* the lumbar spine.[13]

1.5. X-ray Imaging

Since its discovery in 1895 by Wilhelm Roentgen, X-rays have been used in a number of applications: its most notable use being a medical diagnostic tool. The "X-ray picture", known formally as the *radiograph*, has enabled medical practitioners to diagnose problems earlier, and ultimately save and enhance patients' lives.

Recently, however, the capabilities of X-ray radiography have been extended with it moving out of the clinical wards of hospitals to the world of industry. It is becoming commonplace to use X-rays for "seeing" through anything from luggage at airports, to looking for contraband passing across borders or to identifying cracks in airplane components. The list of applications is numerous and continues to grow.

Due to the recent popularity of using X-rays for industrial applications, it seemed that such technology would be appropriate for quantifying the amount of soil in cane. In addition, the literature survey that was carried out indicated that X-ray imaging had not been attempted previously for this problem. Since soil contains more elements with high-atomic numbers that sugar cane (as reported in [7]), the soil particles would stop more low-energy X-rays than the cane. Thus, it was expected that the soil will show up more distinctly than the sugar cane on the X-ray radiographs.

Figure 4 shows *MobileSearch*[5], a truck-mounted, mobile X-ray detection system that can be used for inspecting containers, vehicles or any large item where mobility is necessary. Upon completion of the inspection process, the X-ray unit can be easily stored for over-the-road transport to the next site.

MobileSearch uses transmission and backscattering of X-rays to image objects. Both methods complement each other: backscattering enables detection of materials with low-density and low-atomic numbers while X-ray transmission (the conventional approach) is used to "see" through dense materials (like vehicles).

---

[5] A product of *American Science & Engineering. Inc.*: http://www.AS-E.com
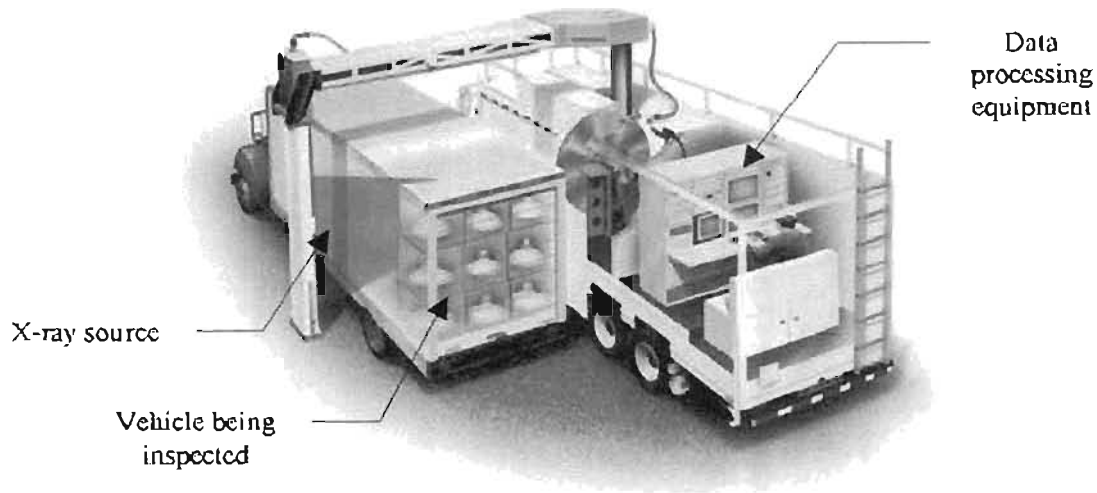
Figure 4: *MobileSearch*, a product employing X-ray technology for imaging vehicles and large containers where mobility is essential.

Some results of *MobileSearch* are shown below. **Figure 5(a)** is an X-ray image of a van, and **Figure 5(b)** is an image of a car with cocaine simulant in the rear compartment.

(a)   (b)
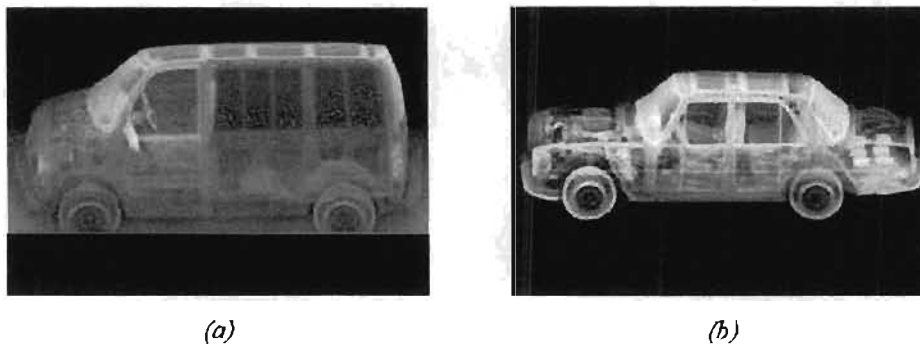
Figure 5: X-ray images obtained with *MobileSearch* of (a) a van and (b) a car with cocaine simulant in the rear compartment. Since *MobileSearch* uses X-ray backscattering, it enables the identification of materials with low-density, such as the cocaine simulant in (b).

An implementation of X-ray imaging, similar to *MobileSearch*, could be the ideal soil monitor (§1.2.7). It is envisaged that trucks, carrying sugar cane from the fields, can be scanned before the cane is transferred to the factories for processing.

2. Background Theory

2.1. Interaction of Gamma Rays with Matter

The three major interaction mechanisms of gamma rays with matter are[14]:

1. Photoelectric Absorption

2. Compton Scattering

3. Pair Production.

All of the above processes result in partial or complete transfer of gamma photon energy to electron energy: the incident photon either disappears or is scattered.

2.1.1. Photoelectric Absorption

In the process of photoelectric absorption, an incident gamma photon is absorbed by an atom. The atom then ejects a *photoelectron* from one of its bound shells. The most tightly bound shell, the *K*-shell, is the most likely origin of the photoelectron for gamma rays with sufficient energy. The interaction occurs directly with an atom, and cannot occur with free electrons.[14]

If the incident gamma ray has energy E, then the ejected photoelectron will possess an energy E_e, given by

$$E_e = E - E_b,$$
(2)

where E_b represents the binding energy of the photoelectron in its original shell.[14]

For low-energy gamma rays, photoelectric absorption is the predominant process. The process is also enhanced for absorber materials with high atomic number, Z. The probability of photoelectric absorption per atom, τ, over all ranges of gamma energy E and Z cannot be expressed simply in a closed form; a rough approximation is[14]

$$\tau \cong k \frac{Z^n}{E^3},$$
(3)

where k represents a constant, Z is the absorber's atomic number, E is the incident photon energy, and n varies between 4 and 5 over the energy region of interest.

2.1.2. Compton Scattering

Compton scattering is an interaction between an incident gamma photon and an electron in the absorbing material. The photon is deflected through an angle θ, with respect to its original direction, after transferring a portion of its energy to the electron (assumed to be initially at rest). The process is depicted in **Figure 6**.
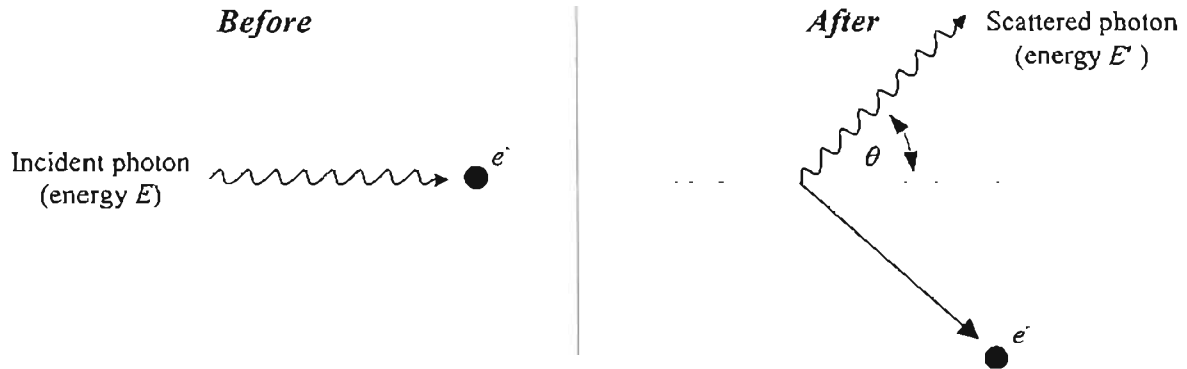
Figure 6: The concept of Compton scattering. An incident gamma photon, possessing energy E, interacts with an electron, and is then deflected through angle θ. The scattered photon has a lower energy of E' while the electron carries off the remaining energy.

Since all scattering angles are possible, the energy transferred to the electron can vary from zero to a large fraction of the incident photon's energy. The relationship between energy transfer and scattering angle θ can be derived by considering conservation of momentum and energy in the interaction[14]:

$$E' = \frac{E}{\left[1 + \dfrac{E}{m_0 c^2}(1 - \cos\theta) \right]}, \tag{4}$$

where E represents the energy of the incident photon, E' the energy of the scattered photon, and $m_0 c^2 = 0.511$ MeV is the rest mass energy of an electron. For small values of θ, the electron carries off little energy. Some of the original energy is always retained by the photon, even in the extreme case of "backscatter" when $\theta = \pi$.

The probability of Compton scattering per atom, σ_C, of the absorber is dependent upon the number of electrons that serve as scattering targets. Therefore, σ_C varies linearly with the atomic number, Z, of the absorber.[14]

2.1.3. Pair Production

The third process of pair production is only energetically possible if the incident gamma energy exceeds *twice* the rest mass energy of an electron, that is, for photon energies greater than 1.022 MeV. This interaction occurs in the Coulomb field of the nucleus; the incident photon disappears and is consequently replaced by an electron-positron pair. Excess photon energy above 1.022 MeV goes into kinetic energy shared by the electron and positron.[14]

The lifetime of the positron is short as it will be annihilated after slowing down in the absorber – this results in two annihilation photons being created as secondary products of pair production.[14]

The probability of pair production per nucleus, κ, varies approximately as the *square* of the atomic number of the absorber.[14]

2.1.4. *XCOM*

XCOM, described in [15], is a computer program that enables the calculation of photon cross-sections for photoelectric absorption, Compton scattering and pair production, as well as total attenuation coefficients in any element, compound or mixture for energies from 1 keV to 100 GeV.

To calculate the cross-sections for a specific material, *XCOM* requires the elements and/or compounds comprising the material, together with the relative concentration of each of the constituents.

XCOM is prominently used[16] as a means to compare experimental and theoretical cross-sections. The current work used *XCOM* exclusively for calculating theoretical cross-sections.

2.1.5. Comparison of Interaction Mechanisms

The relative importance of the above-mentioned interactions for different absorber materials and photon energies is illustrated in **Figure 7**. The lines, marked $\sigma_C = \tau$ and $\sigma_C = \kappa$, show the values of atomic number, Z and energy, E for which the two neighbouring effects are just equal.

For a fixed Z, the dominant process for low-energy (~0.01 MeV) photons is photoelectric absorption, while Compton scattering dominates for high-energy (~1 MeV) photons. The *DuET*-technique exploits this distinction.
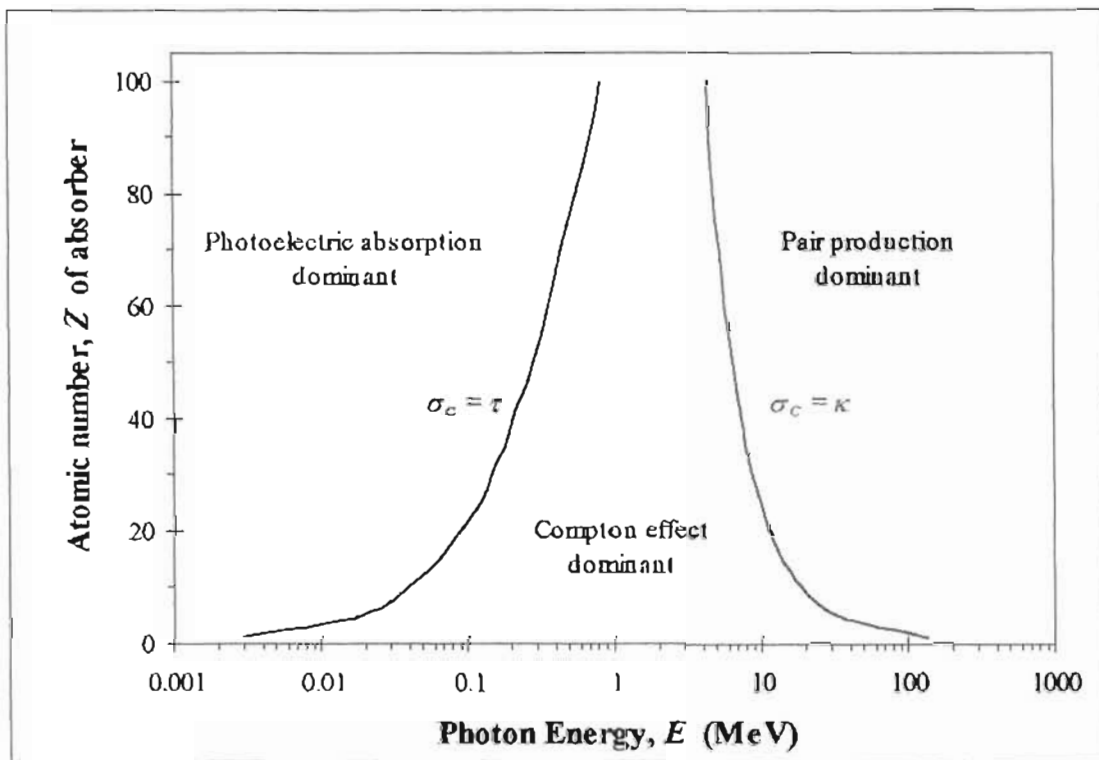
Figure 7: Comparison of the relative importance of photoelectric absorption, Compton scattering and pair production. The lines, marked $\sigma_C = \tau$ and $\sigma_C = \kappa$, show the values of Z and E for which the two neighbouring effects are just equal. This plot was created using cross-sections calculated by *XCOM* [15].

2.2. Attenuation of Gamma Rays

2.2.1. Attenuation Coefficients

Consider the experiment illustrated in **Figure 8** below. A collimated source of mono-energetic gamma rays is counted by a detector after being transmitted through an absorber of thickness, x.
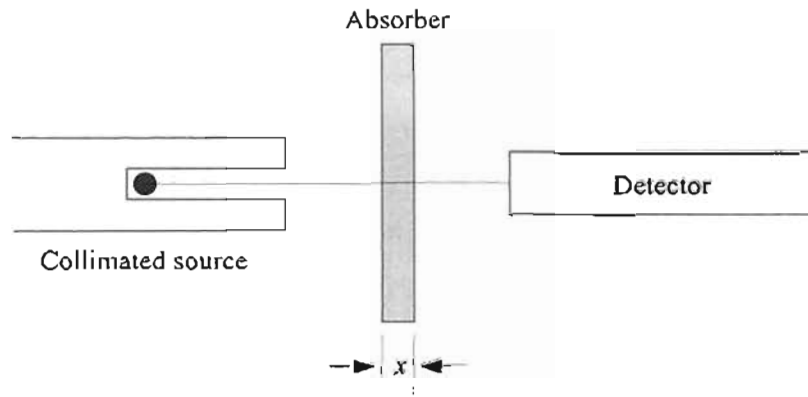
Figure 8: Attenuation of gamma rays by an absorber of thickness, x. This experimental arrangement illustrates a "narrow beam"-geometry: the incident beam is highly collimated such that only gamma rays that escape interaction in the absorber are counted by the detector.

In the absorber, each of the interaction processes (§2.1) removes gamma ray photons from the incident beam, either by absorption or by scattering away from the detector direction. Each process can be characterised by a fixed probability of occurrence per unit path length in the absorber (τ, σ_C or κ). The *sum* of these probabilities, μ', is simply the probability per unit path length that the gamma photon is removed from the beam:[14]

$$\mu' = \tau \text{ (photoelectric)} + \sigma_C \text{ (Compton)} + \kappa \text{ (pair production)}. \qquad (5)$$

μ' is called the *linear attenuation coefficient*.

In **Figure 8**, the number of transmitted photons, I, is given by the relation

$$\frac{I}{I_0} = exp\left(-\mu' x\right), \qquad (6)$$

where I_0 represents the number of recorded counts if the absorber was absent.[14]

Equation (6) is one of the many forms of the *Beer-Lambert Law*[17], which expresses the linear relationship between absorbance and concentration of an absorber of electromagnetic radiation.

In practice, the linear attenuation coefficient is quite cumbersome to use as it varies with the density of the absorber, even though the absorber material is the same. Therefore, the *mass attenuation coefficient, μ,* is more widely used, and is defined as

$$\mu = \frac{\mu'}{\rho},$$

(7)

where ρ represents the density of the absorber.[14]

For a given gamma energy, μ is *independent* of the physical state of a given absorber and depends only on its elemental composition: for example, μ is the same for water whether present in liquid or vapour form.[14]

The mass attenuation coefficient of a compound or mixture of elements can be calculated from

$$\mu_{compound\,/\,mixture} = \sum_i w_i \left(\frac{\mu'}{\rho} \right)_i = \sum_i w_i \mu_i,$$

(8)

where w_i represents the weight fraction of element i in the compound or mixture while μ_i is the mass attenuation coefficient of element i.[14]

In terms of the mass attenuation coefficient, (6) becomes:

$$\frac{I}{I_0} = exp(-\mu\rho x).$$

(9)

2.2.2. Build-up

The experimental arrangement of **Figure 8** illustrates a "narrow beam"-geometry: the incident beam is highly collimated such that only gamma rays that escape interaction in the absorber are counted by the detector.

In practice, however, strong beam collimation is often absent. This situation, depicted in **Figure 9**, is termed a "broad beam"-geometry. The detector can now react to both *direct* and *scattered* photons.
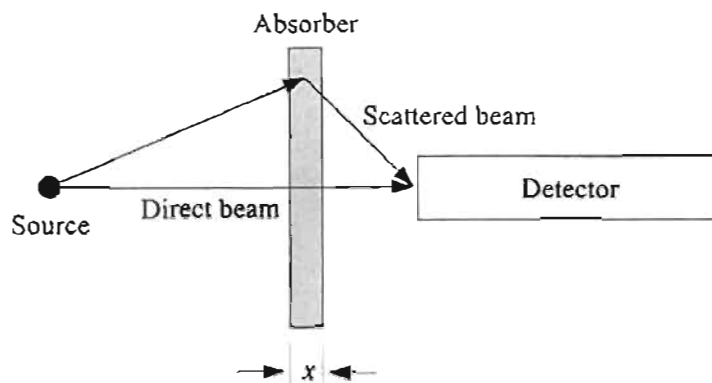
Figure 9: Attenuation of gamma rays by an absorber of thickness, *x*. The above arrangement is termed a "broad beam"-geometry since the source is not strongly collimated. Hence, the detector can react to both the direct beam through the sample, and also to the scattered beam emanating from the sample and surrounding material. The relation, expressed by (9), is not valid in this situation.

Consequently, the measured counts are greater due to counting of the scattered photons as well. Therefore, values for μ determined from **(9)**:

$$\mu = \frac{1}{\rho x} \ln\left(\frac{I_0}{I}\right), \tag{10}$$

will be smaller than they should be, and therefore, equation **(9)** must be modified to take this into account. The usual method is to modify **(9)** in such a manner to retain the exponential behaviour while catering for the additional contribution from scatter:[14]

$$\frac{I}{I_0} = B(x, E) \cdot \exp(-\mu \rho x), \tag{11}$$

where $B(x, E)$ is called the *build-up factor* and is dependent upon the absorber thickness, the energy E of the incident photons and the specific geometry being used. I refers to the total number of photons (direct and scattered) counted by the detector.

2.3. Gamma Spectroscopy

Figure 10 is a block diagram of a typical gamma spectroscopy system for counting the number of gamma rays of specific energies being emitted by a radioactive source. Such an arrangement was used for the investigation of *DuET*. Descriptions of the various components of the system are given below.

```
                        ┌──────────────┐
                        │ High Voltage │
                        │   Supply     │
                        └──────────────┘
                               │
                               ▼
   ●          ┌───────────────────┐        ┌──────────────┐
Radioactive   │ NaI (Tl)-detector │ ─────► │ Preamplifier │
  Source      └───────────────────┘        └──────────────┘
                                                   │
                                                   ▼
                                           ┌──────────────┐
                                           │   Linear     │
                                           │  Amplifier   │
                                           └──────────────┘
                                                   │
                                                   ▼
                                           ┌──────────────┐
                                           │ Multichannel │
                                           │  Analyser    │
                                           │   (MCA)      │
                                           └──────────────┘
```
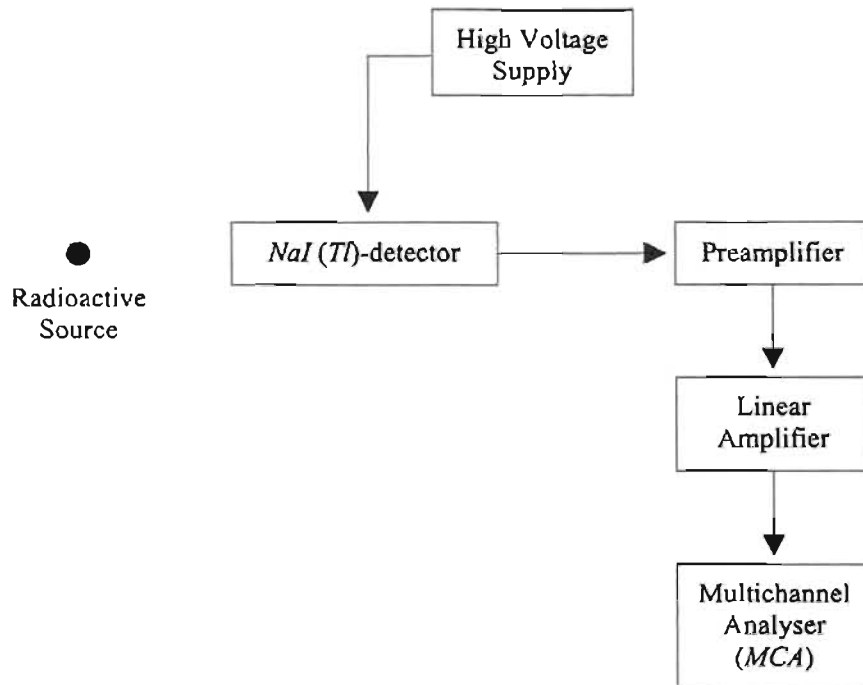
Figure 10: Block diagram of a gamma spectroscopy system for counting the number of gamma photons of specific energies emanating from a radioactive source.

2.3.1. *NaI (Tl)*-detector

The detector essentially consists of two components:

1. thallium-activated sodium iodide crystal, *NaI (Tl)*

2. photomultiplier tube (*PMT*).

Incident gamma rays from the source interact with the *NaI (Tl)*-crystal producing pulses of visible light. These pulses fall upon the *photocathode* of the *PMT*, which converts as many of the incident light pulses as possible to low-energy electrons, called *photoelectrons*.

19

The photocathode produces only a few photoelectrons, and this number is too small to constitute a detectable electrical signal. The *electron multiplier section* of the *PMT* is therefore responsible for providing an efficient collection geometry for the photoelectrons, and also to amplify their number. Consequently, a typical scintillation pulse will result in about $10^7 - 10^{10}$ electrons; this is sufficient to serve as a charge signal for the original scintillation event. This charge is conventionally collected at the anode (or output stage) of the multiplier structure.[14]

The result is that the detector has produced a voltage pulse with an amplitude that is proportional to the energy deposited in the crystal by the incident gamma photon.

2.3.2. High Voltage Supply

The high voltage supply provides the potential for the operation of the *PMT* of the detector.

2.3.3. Preamplifier

The *PMT* produces a small voltage pulse; the role of the *preamplifier* is, therefore, to provide the first stage in pulse amplification while attempting to minimise the addition of noise to the pulse.

2.3.4. Linear Amplifier

The main function of the *linear amplifier* is to increase the amplitude of the voltage pulses from the preamplifier. The *amplification factor* or *gain* varies with application, and is normally adjusted to provide the required range of pulse amplitudes for acceptance by the next component of the system.

2.3.5. Multichannel Analyser

The basic function of the *multichannel analyser* (*MCA*) is implemented using an analog-to-digital converter (*ADC*) and memory (**Figure 11**). The *ADC* converts an incoming analog signal (the pulse amplitude from the linear amplifier) to a corresponding digital number. The *MCA*'s memory can be imagined as a stack of addressable locations, ranging from the first address on the left through to some

maximum location number (say, 2048) on the right. The memory locations are commonly referred to as *channels*.[14]
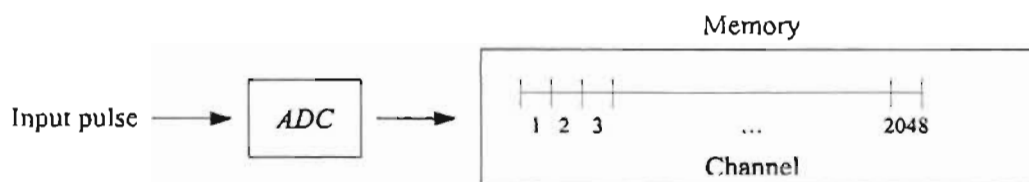
Figure 11: Simplified block diagram of an *MCA*. An incoming analog pulse from the linear amplifier is processed by the *ADC*, producing a digital number. The memory location, corresponding to the digital number, is then accessed, and its content is incremented by one.

Once a pulse has been processed by the *ADC*, the control circuits of the *MCA* seek out the memory location corresponding to the digitised amplitude, and the content of that address is then incremented by one. For example, if the memory consists of 2048 channels and the input voltage pulse ranges from 0 V to 10 V, then a pulse with a peak voltage of 2.5 V will fall into channel 512, and the content of this channel will be raised by one count.

The contents of the memory are displayed to produce a *pulse height spectrum*, which is a plot of the number of counts per channel versus channel (or energy, if the system is calibrated). For this project, the *PCA II*-software[6] was used to visualise the *MCA*'s memory. The spectra, which were recorded for *DuET*, consisted of 2048 channels. **Figure 12** shows a normalised *pulse height spectrum* of ^{137}Cs.

The time, over which the detector system is set to count, is termed the *integration time, t_i*. The *PCA II*-software enabled the user to set the integration time[7] for a counting measurement.

---

[6] *PCA II* ver. 2.20, *Tennelec/Nucleus, Inc.*, 1993

[7] The *"live time"*-setting in *PCA II* was used.

2.3.6. Radioactive Source

For this investigation of *DuET*, standard laboratory sources of ^{137}Cs were used. This radioisotope is one of the most commonly-used sources due to its well-known decay scheme and long half-life of 30 years.

A radioactive ^{137}Cs-nucleus decays through the emission of a β^-–particle. This results in an excited ^{137m}Ba-daughter[8]. Due to selection rules, the only path to the ground state is by radiating a 662 keV-gamma ray. The result is stable ^{137}Ba.

However, competing with gamma emission is another processes, called *internal conversion*[18], where the nucleus de-excites by transferring its energy directly to an atomic electron, which is ejected from the atom, and appears in the laboratory as a free electron. The atom is then left with a vacancy in one of the electronic shells. The vacancy is quickly filled from electrons in higher shells, resulting in the emission of *characteristic X-rays*. With respect to ^{137}Cs, these X-rays have energies of the order of 30 keV. Low-resolution detectors, like the *NaI*-detector, cannot separate each of the low-energy X-rays. In practice, the *NaI*-detector counts all the X-ray energies to form a single, broad low-energy peak. Therefore, for convenience, the current work on *DuET* used the most probable emission of 32.2 keV to represent the low-energy beam while the 662 keV-line represented the high-energy beam (**Figure 12**).

In **Figure 12**, the low- and high-energy peaks from ^{137}Cs are labelled "32.2 keV" and "662 keV", respectively; the area under these two peaks correspond to the number of photons that escaped interaction within the sample. The method of obtaining peak areas is described in **Appendix B**.

---

[8] "^{137m}Ba" refers to the (excited) metastable state of barium. [18]

Owing to the use of lead (*Pb*) for detector shielding during the recording of the spectrum below (**Figure 12**), the characteristic X-rays of *Pb* (~74 and ~84 keV [17]) were also detected due to interaction of the 662 keV-line with the shielding. The location of the *Compton edge*, which represents the maximum energy imparted to an electron in the Compton interaction, is also indicated on **Figure 12**.
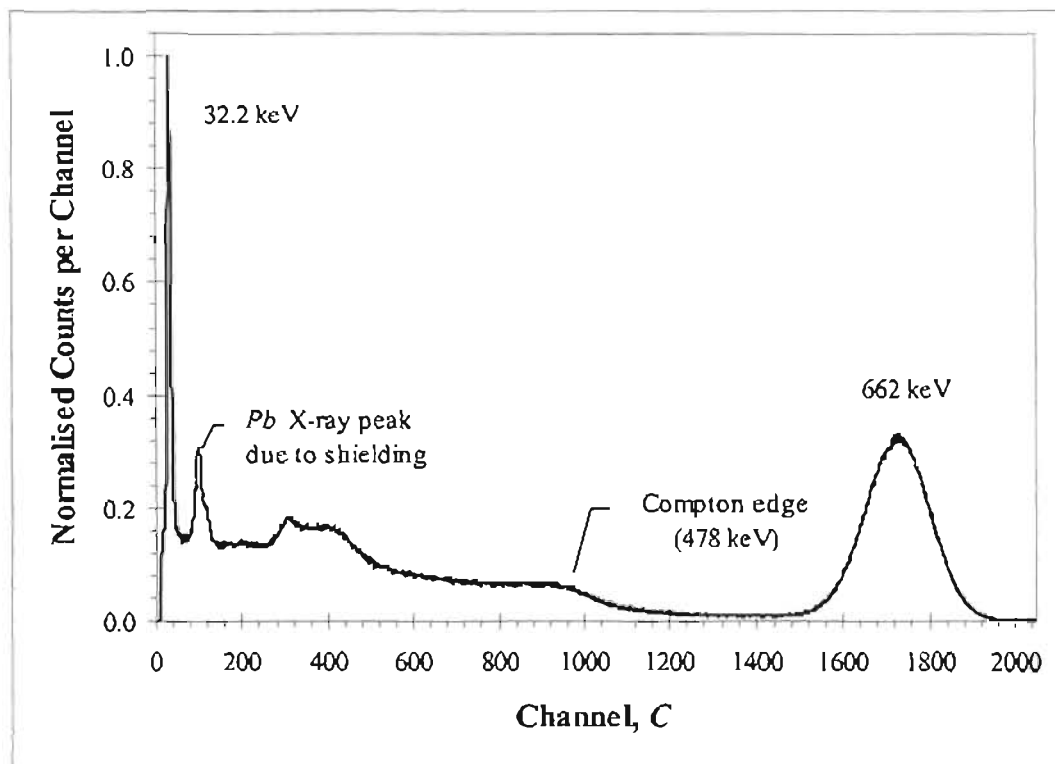
Figure 12: A normalised pulse height spectrum of [137]*Cs* recorded with a *NaI (Tl)*-detector. The low- and high-energy peaks, used in this work, are labelled "32.2 keV" and "662 keV", respectively. The 32.2 keV-line is actually a multiplet of X-rays. A peak, corresponding to the detection of characteristic X-rays from the lead shielding, can also be seen; this was due to the 662 keV-photons interacting with the shielding. The Compton edge, which is the maximum energy imparted to the electron in the Compton interaction, is also indicated on the spectrum.

2.4. Counting Statistics and Error Analysis

The process of radioactive decay is statistical: it cannot be said with certainty that a specific atom is going to decay. Therefore, the fundamental concepts of statistics must be understood to analyse data recorded from the counting of emissions from radioactive atoms.

2.4.1. Definitions

Table 1: Definitions of mean, variance and standard deviation for the sample and population, assuming N measurements of a random variable x.

Quantity	Sample	Population
Mean	$\bar{x} = \dfrac{1}{N} \sum\limits_{i=1}^{N} x_i$	$M = \lim\limits_{N \to \infty} \bar{x}$
Variance	$s^2 = \dfrac{1}{N-1} \sum\limits_{i=1}^{N} (x_i - \bar{x})^2$	$\sigma^2 = \lim\limits_{N \to \infty} s^2$
Standard deviation	s	σ

The true mean, variance and standard deviation (M, σ^2, σ) refer to the actual quantities exhibited by a random system. However, estimates of these values, as represented by $\bar{x}$, s^2 and s, can be determined from a finite set of measurements.

24

2.4.2. The Poisson Distribution

Under the conditions that are thought to apply to all radioactive decays, that is,[14]

1. all the nuclei are identical,

2. all the nuclei are independent, and

3. each nucleus has a definite and constant probability of decay in a unit time interval,

a distribution function, $P(x)$, can be derived that describes the probability of observing x counts in one observation period. The distribution of the values about the true mean, M, has a *Poisson distribution* given by

$$P(x) = \frac{M^x}{x!} e^{-M} . \tag{12}$$

Figure 13 shows a Poisson distribution for a random variable x with a true mean of $M = 50$.
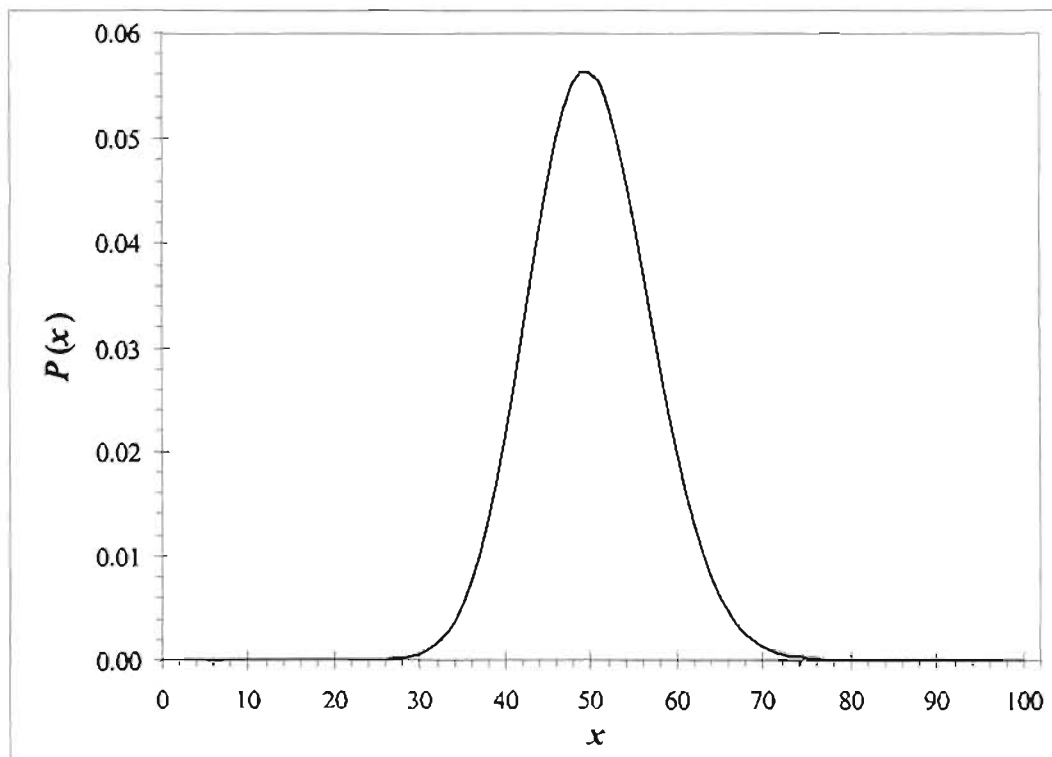
Figure 13: Theoretical Poisson distribution for a true mean of 50.

25

2.4.3. The Meaning of σ

If the mean of a Poisson distribution is $\gtrsim 20$, the distribution then becomes symmetrical, and assumes the characteristics of a *normal* or *Gaussian distribution*, which has the property that 68 % of the total area of the distribution lies within one standard deviation, $\pm \sigma$, of the mean.

For a Poisson distribution,

$$\sigma = \sqrt{M} \ . \tag{13}$$

Therefore, since x has a high probability of being close to M, then

$$\sigma = \sqrt{x} \ , \tag{14}$$

and one can say that a single measurement is 68 % likely to be within $\pm\sqrt{x}$ of the true mean. When plotting experimental results, it is customary to include error bars of length σ_i on each point x_i.

Equation (14) applies only to *raw numbers of events*, and not to calculated quantities such as rates or differences between numbers of counts (which is dealt with in §2.4.5).

2.4.4. Relative Error, r

The *relative error*, r, for a random variable x is defined as

$$r = \frac{\sigma_x}{\overline{x}} \ , \tag{15}$$

where σ_x is the standard deviation and $\overline{x}$ is the mean of x. The relative error is also known as the *fractional standard deviation*[14].

2.4.5. Error Propagation

Often encountered is the situation where a desired value is a function of several measured values, each having finite statistical uncertainties. If $u = u(x, y, z, ...)$ is a function of independent random variables, $x, y, z, ...$, then there will be a certain spread in u associated with the spreads in $x, y, z, ...$

By applying Probability Theory, the following general formula, named the *error propagation formula*[14], can be derived:

$$\sigma_u^2 = \left(\frac{\partial u}{\partial x} \cdot \sigma_x \right)^2 + \left(\frac{\partial u}{\partial y} \cdot \sigma_y \right)^2 + \left(\frac{\partial u}{\partial z} \cdot \sigma_z \right)^2 + ... \tag{16}$$

which relates σ_u, the expected uncertainty in a calculation of u, to the corresponding uncertainties $\sigma_x, \sigma_y, \sigma_z, ...$ of the variables $x, y, z, ...$

The random variables $x, y, z, ...$ must each be normally distributed with the uncertainties $\sigma_x, \sigma_y, \sigma_z, ...$ small enough so that the differentials accurately describe the variations in u.

Equation (16) is applicable to almost all situations in nuclear measurements. For example, if

$$u = \frac{x}{y}, \tag{17}$$

where x and y are the results of two counting experiments, then applying (16) gives

$$\left(\frac{\sigma_u}{u} \right)^2 = \left(\frac{\sigma_x}{x} \right)^2 + \left(\frac{\sigma_y}{y} \right)^2, \tag{18}$$

and incorporating equation (14) yields

$$\sigma_u = u \sqrt{\frac{1}{x} + \frac{1}{y}} . \tag{19}$$

2.4.6. Correlation Coefficient and $\mathfrak{R}^2$

The *linear Pearson correlation coefficient*, $\mathfrak{R}$, is a measure of how well a set of experimental data can be represented by a specific model, and is given by[9]

$$\mathfrak{R} = \frac{N\sum(XY) - (\sum X)(\sum Y)}{\sqrt{\left[N\sum X^2 - (\sum X)^2\right]\left[N\sum Y^2 - (\sum Y)^2\right]}}, \qquad (20)$$

where $X = \{x_1, x_2, ..., x_N\}$ and $Y = \{y_1, y_2, ..., y_N\}$ represent independent and dependent data sets, respectively, and N is the number of elements of each set.

$\mathfrak{R}$ is a dimensionless quantity that varies from -1 to $+1$ inclusive. A more convenient quantity to use is $\mathfrak{R}^2$ since $0 \le \mathfrak{R}^2 \le 1$. The closer the value of $\mathfrak{R}^2$ to unity, the smaller the overall deviation between the two data sets being compared.

2.5. Obtaining Relative Concentrations from a *DuET*-measurement

The theory, for obtaining the relative concentrations of the components of a binary mixture via *DuET*, is developed below.[19]

For the dual-energy arrangement shown in **Figure 2**, with a binary sample of thickness x and density ρ, and assuming a build-up factor of unity, the number of counts recorded for the transmitted low- and high-energy beams is given by

$$L = L_0 \exp\left(-\rho\mu_L x\right) \qquad (21)$$

$$H = H_0 \exp\left(-\rho\mu_H x\right) \qquad (22)$$

using equation (9). L and L_0 refer to the number of transmitted and unattenuated counts, respectively, for the low-energy beam. Similarly, H and H_0 represent the respective quantities for the high-energy beam. μ_L and μ_H represent the mass attenuation coefficients for the sample at the low- and high-energies, respectively.

---

[9] *Microsoft Excel 2000* Online Help; Microsoft Corporation; 1999

Solving equations **(21)** and **(22)** for ρx, and equating the resulting expressions yields

$$R \equiv \frac{\mu_L}{\mu_H} = \frac{\ln\left(\dfrac{L}{L_0}\right)}{\ln\left(\dfrac{H}{H_0}\right)}, \tag{23}$$

where R represents the ratio of the low-energy mass attenuation coefficient to that of the high-energy coefficient for the mixture. R is independent of density and thickness of the sample, and can be obtained directly from experimental measurements of L, L_0, H and H_0.

Since the mixture is composed of two components, then μ_L and μ_H can be further decomposed using **(8)**:

$$\mu_L = w_1 \cdot \mu_{L1} + w_2 \cdot \mu_{L2}$$
$$\mu_H = w_1 \cdot \mu_{H1} + w_2 \cdot \mu_{H2} \tag{24}$$

where μ_{L1}, μ_{L2}, μ_{H1} and μ_{H2} represent the *individual* mass attenuation coefficients for each of the two components ("1" and "2") at the low- and high-energies, and w_i represents the fractional concentration of component i such that $\sum w_i = 1$.

Thus, applying **(24)** to **(23)** and taking into account that $w_1 + w_2 = 1$, yields

$$R = \frac{\mu_{L1} + w_2 \cdot (\mu_{L2} - \mu_{L1})}{\mu_{H1} + w_2 \cdot (\mu_{H2} - \mu_{H1})}, \tag{25}$$

which can be written in the more convenient form:

$$R = \left(\frac{\mu_{L1}}{\mu_{H1}}\right) \left[\frac{1 + \left(\dfrac{\mu_{L2}}{\mu_{L1}} - 1\right) \cdot w_2}{1 + \left(\dfrac{\mu_{H2}}{\mu_{H1}} - 1\right) \cdot w_2}\right]. \tag{26}$$

Making w_2 the subject of the formula, (26) gives

$$w_2 = \frac{\left(\dfrac{\mu_{L1}}{\mu_{H1}}\right) - R}{\left(\dfrac{\mu_{H2}}{\mu_{H1}} - 1\right) \cdot R - \left(\dfrac{\mu_{L1}}{\mu_{H1}}\right)\left(\dfrac{\mu_{L2}}{\mu_{L1}} - 1\right)} \, . \tag{27}$$

This enables the calculation of w_2, the fractional concentration of component "2", from R. The values of $\left(\dfrac{\mu_{L1}}{\mu_{H1}}\right)$, $\left(\dfrac{\mu_{L2}}{\mu_{L1}}\right)$ and $\left(\dfrac{\mu_{H2}}{\mu_{H1}}\right)$ can be determined experimentally from calibration measurements using known concentrations of components "1" and "2".

A single *DuET*-spectrum of a sample provides the number of counts under the low- and high-energy peaks. The values for L_0 and H_0 are obtained from a *DuET*-spectrum recorded in the absence of a sample. Each of the four measured quantities have uncertainties associated with them. The uncertainty, associated with a *single* calculation of R, can be derived from (16):

$$\sigma_R = \left| \ln\left(\frac{H}{H_0} \right) \right|^{-1} \sqrt{\frac{1}{L} + \frac{1}{L_0} + R^2 \left(\frac{1}{H} + \frac{1}{H_0} \right)} \, . \tag{28}$$

3. Description and Preparation of Samples

3.1. Sugar Cane

Sugar cane stalks were provided by the *Sugar Milling Research Institute (SMRI)*[10]. These stalks were cleaned with a dampened cloth, wiped dry, shredded, sealed in plastic bags, and then frozen.

When required, the frozen cane was dried in a *light box*, a closed wooden enclosure fitted with light bulbs on the interior, for about 4 hours.

The dried cane was then milled in a coffee grinder to produce a fine mixture. A picture of a sample of shredded sugar cane is shown in **Figure 14**.
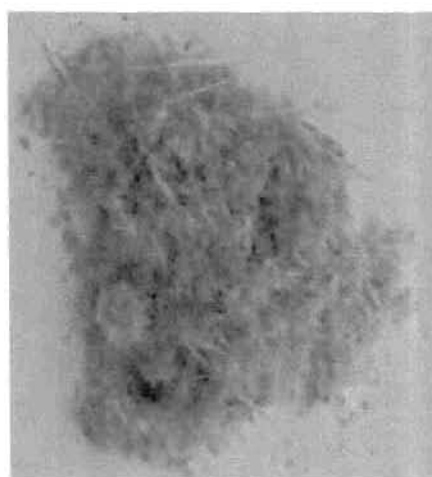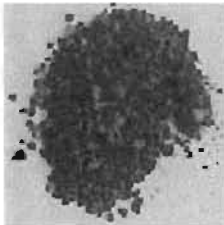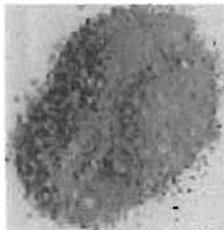
Figure 14: Picture of a shredded sugar cane-sample.

---

[10] *Sugar Milling Research Institute*, University of Natal, Durban, 4041, South Africa: http://www.smri.org

3.2. Soil

Four soil samples, also provided by *SMRI*, were available (**Table 2**). These soil samples were extracted from various cane fields[11].

Table 2: Soil samples.

Soil	Physical Description	Image of soil sample
Empangeni	Dark, coarse grains	
Heatonville	Dark, coarse grains	
Leaf	Light, coarse grains	
Umhloti	Red, clayey, fine grains	

The elemental composition of the above soil samples were determined using *Energy Dispersive Spectroscopy*, described in **Chapter 4**.

---

[11] Courtesy of Arlindo Mendes

3.3. Soil in Cane-Samples

For a two-component mixture consisting of materials A and B, the *percentage concentration* of material A, denoted by $[A]$, is given by

$$[A] = \frac{m_A}{m_A + m_B} \times 100, \tag{29}$$

where m_A and m_B are the masses of A and B, respectively.

Various amounts of *Empangeni*-soil and dried, shredded cane were mixed to produce a range of soil concentrations from 0 % (no soil) to 41.9 %.

The samples were stored in plastic containers, known as *polytops*. The *polytops* were cylindrical, with an internal base diameter of 51 mm and a height of 56 mm (including lid). A picture of a *polytop* with a cane sample is shown in **Figure 15**.
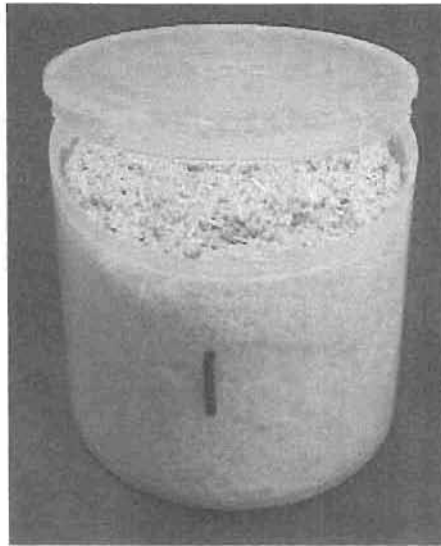
Figure 15: A picture of a *polytop* with a sugar cane-sample. Assigning a height to the sample is quite difficult unless the sample is compressed. For this investigation, the soil/cane-samples were left uncompressed, and the approximate heights of the various samples ranged from about 35 mm to 50 mm.

It was assumed that the *polytops* would not significantly attenuate any incident radiation considering that they were made of low-Z elements, which would indicate low mass attenuation coefficients.

4. Elemental Composition of Sugar Cane and Soil determined via Energy Dispersive Spectroscopy

4.1. Introduction

The elemental compositions of the soil samples (**Table 2**) and sugar cane were determined *quantitatively* using a *Scanning Electron Microscope (SEM)* at the *EM Unit* (University of Natal). The aim of this investigation was to compare the variations in composition of the four soils and sugar cane since the sensitivity of *DuET* is determined by differences in mass attenuation coefficients between the components of the binary mixture. It was expected that the soil samples would have elements with higher atomic numbers (resulting in higher μ-values) than the sugar cane.

The *SEM* uses the technique of *Energy Dispersive Spectroscopy (EDS)*. Electrons strike the sample after being accelerated across a high voltage. The incident electrons excite the atoms of the sample. The excited atoms return to the ground state by emitting *characteristic X-rays*, which are unique to an element. The X-rays are counted by an energy-sensitive detector, and elements present in the sample are identified by subsequent analysis of the energy spectrum.

The applied high voltage determines the maximum energy possessed by the electrons before striking the sample: if the voltage is 20 kV, the maximum energy attained by the electrons is 20 keV immediately before hitting the sample. Consequently, it is not possible for characteristic X-rays more energetic than 20 keV to be emitted. The accelerating voltage thus restricts the elements that can be identified.

For light (low Z) elements, the penetration depth of the electrons is approximately 8 – 10 μm, and for heavier elements, the depth is about 5 – 8 μm [12]. Therefore, *EDS* is only capable of analysing a thin, superficial layer of a sample.

In general, only elements above boron ($Z = 5$) in the Periodic Table can be detected.

---

[12] Private communication: Dr. Fiona Graham, *EM Unit* (University of Natal)

4.2. Apparatus

The *EDS*-system that was used consisted of the following:

1. *Hitachi S-520 SEM*

2. *Oxford Instruments'* X-ray detector

3. *LINK ISIS*-software

4.3. Sample Preparation

The four soil samples (**Table 2**) were mounted on graphite disks. The shredded sugar cane sample was frozen prior to the measurements, and since the elemental analysis is performed under vacuum, it was necessary to dry the cane sample before being mounted.

Figure 16 shows high-magnification images of the *Heatonville-* and *Umhloti*-soil samples.

(a)   (b)
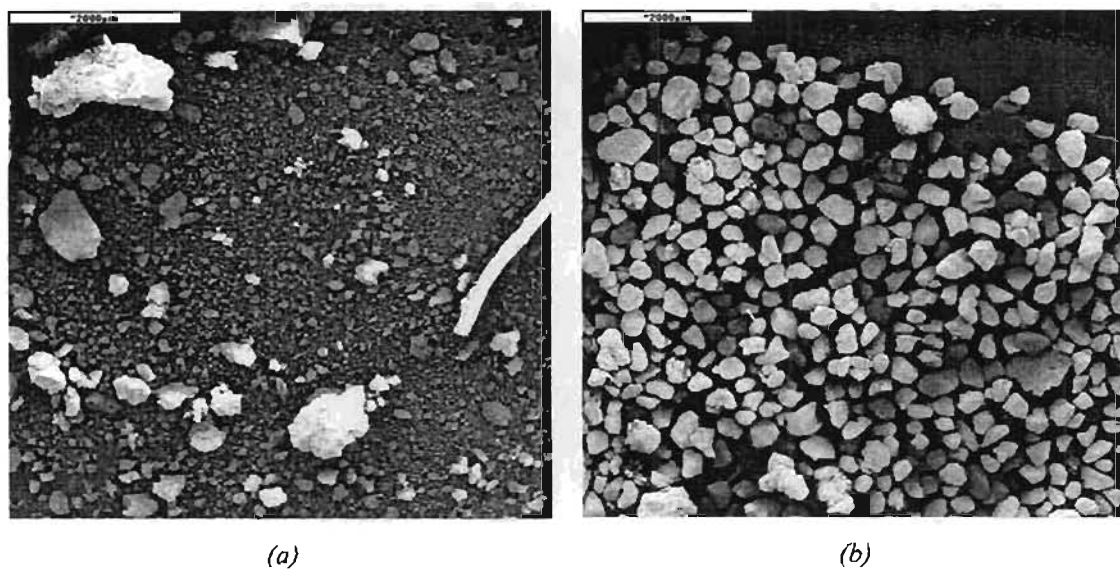
Figure 16: High-magnification image of the *(a) Heatonville*-soil sample, and *(b) Umhloti*-soil sample. The images were obtained using the camera attached to the *SEM*.

4.4. Method

Each of the graphite disks, with the samples, was in turn mounted on the *SEM*-sample platform. The chamber was then evacuated, and the accelerating voltage of the *SEM* was set to 20 kV.

The microscope was adjusted to obtain a field-of-view (the area of the sample seen by the microscope) of approximately 3 mm × 4 mm.

All spectra were recorded with the *LINK ISIS*-software, and the integration time was ~100 s per sample. For each sample, the analysis was performed five times (at various sample locations) to average out any elemental inhomogeneities.

4.5. Analysis

An *EDS*-spectrum is a plot of the count rate (in cps [13]) vs. X-ray Energy (in keV). **Figure 17** and **Figure 18** are examples of *EDS*-spectra, obtained for the *Heatonville*-soil sample and shredded sugar cane, respectively.

The positions of the peaks in the *EDS*-spectrum are indicative of the elements present in the sample, while the peak areas indicate the concentration of the elements. The spectra were analysed using *LINK ISIS* to obtain the relative concentrations of the elements in the samples. The results are tabulated in **Table 3** and **Table 4**.

---

[13] Counts per second
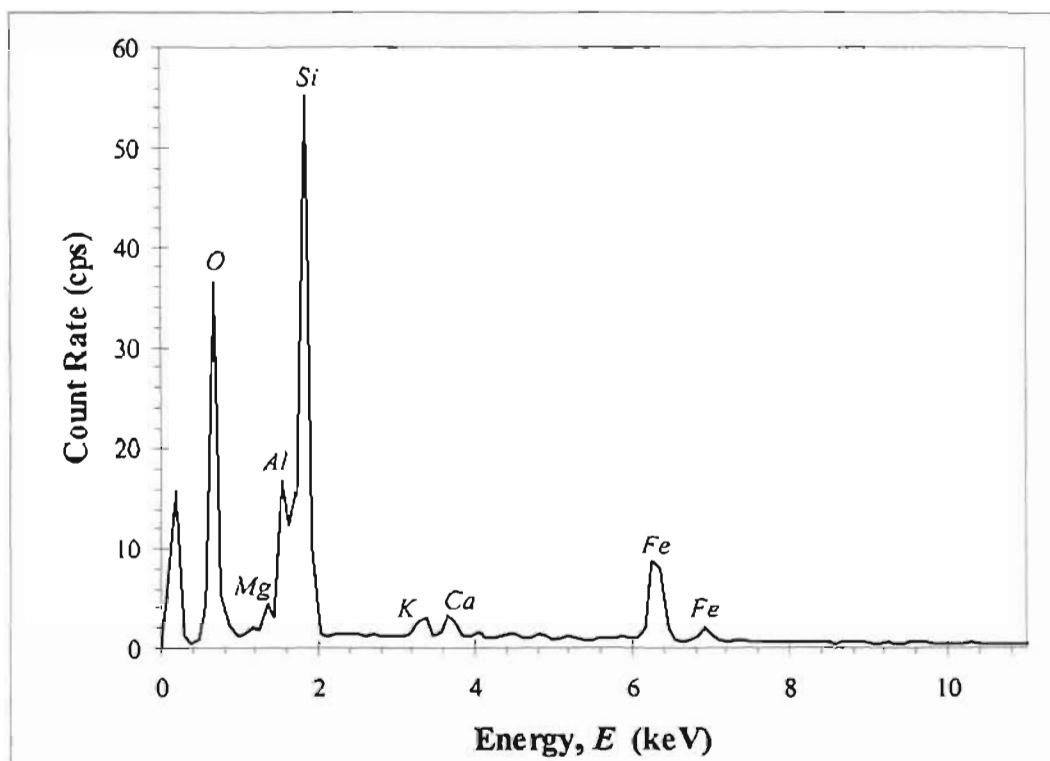
Figure 17: An *EDS*-spectrum of the *Heatonville*-soil sample, recorded with the *LINK ISIS*-software. This spectrum is a plot of count rate vs. X-ray Energy. The position of the peaks indicate the elements in the sample, and the peak areas correspond to the concentration of the various elements. The major elements of the sample were *O, Al, Si* and *Fe*.
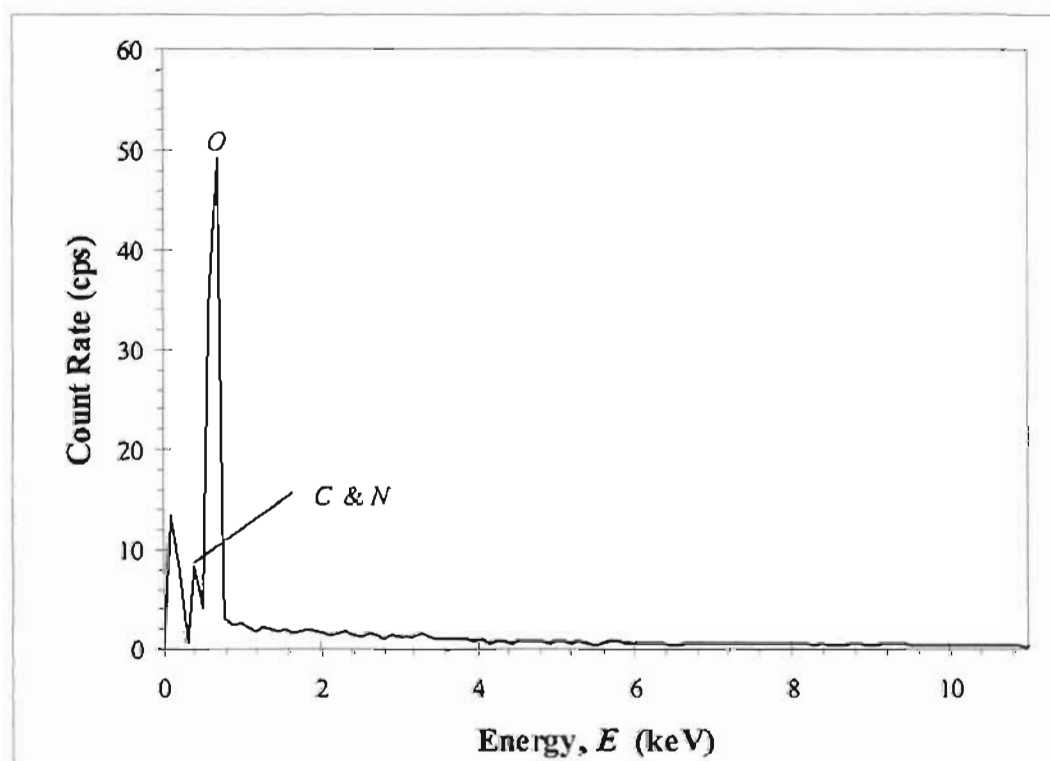
Figure 18: An *EDS*-spectrum of the shredded sugar cane-sample, recorded with the *LINK ISIS*-software. This spectrum is a plot of count rate vs. X-ray Energy. The position of the peaks indicate the elements in the sample, and the peak areas correspond to the concentration of the various elements. The major elements of the sample were *C, N* and *O*.

37

Table 3: Relative elemental concentrations of the soil samples by atomic weight (%). Minimum (*Min*), mean and maximum (*Max*) concentrations are listed. The mean concentrations for the four soils are plotted in **Figure 19**.

Element	Heatonville			Umhloti			Umgeni			Leaf		
	Min	Mean	Max	Min	Mean	Max	Min	Mean	Max	Min	Mean	Max
O	63.2	64.5	65.9	66.2	67.1	67.5	68.3	68.7	69.1	66.4	67.1	67.4
Na	0.4	0.5	0.7	0.0	0.0	0.0	0.0	0.0	0.0	0.0	0.0	0.0
Mg	0.7	0.9	1.2	0.0	0.0	0.0	0.0	0.0	0.0	0.0	0.0	0.0
Al	5.7	6.1	6.4	2.6	3.0	3.3	3.8	4.1	4.4	7.3	7.7	8.0
Si	19.0	19.6	20.1	25.0	26.2	27.6	23.4	24.0	24.6	20.3	21.0	21.5
K	0.7	0.7	0.8	0.2	0.3	0.3	0.2	0.2	0.3	1.2	1.3	1.4
Ca	0.7	0.8	0.9	0.0	0.0	0.0	0.0	0.0	0.0	0.0	0.0	0.0
Ti	0.2	0.3	0.3	0.3	0.3	0.4	0.3	0.3	0.4	0.2	0.3	0.6
Mn	0.0	0.0	0.0	0.0	0.0	0.0	0.0	0.0	0.0	0.0	0.0	0.0
Fe	6.1	6.5	7.2	2.9	3.2	3.6	2.4	2.6	2.6	2.5	2.6	2.7
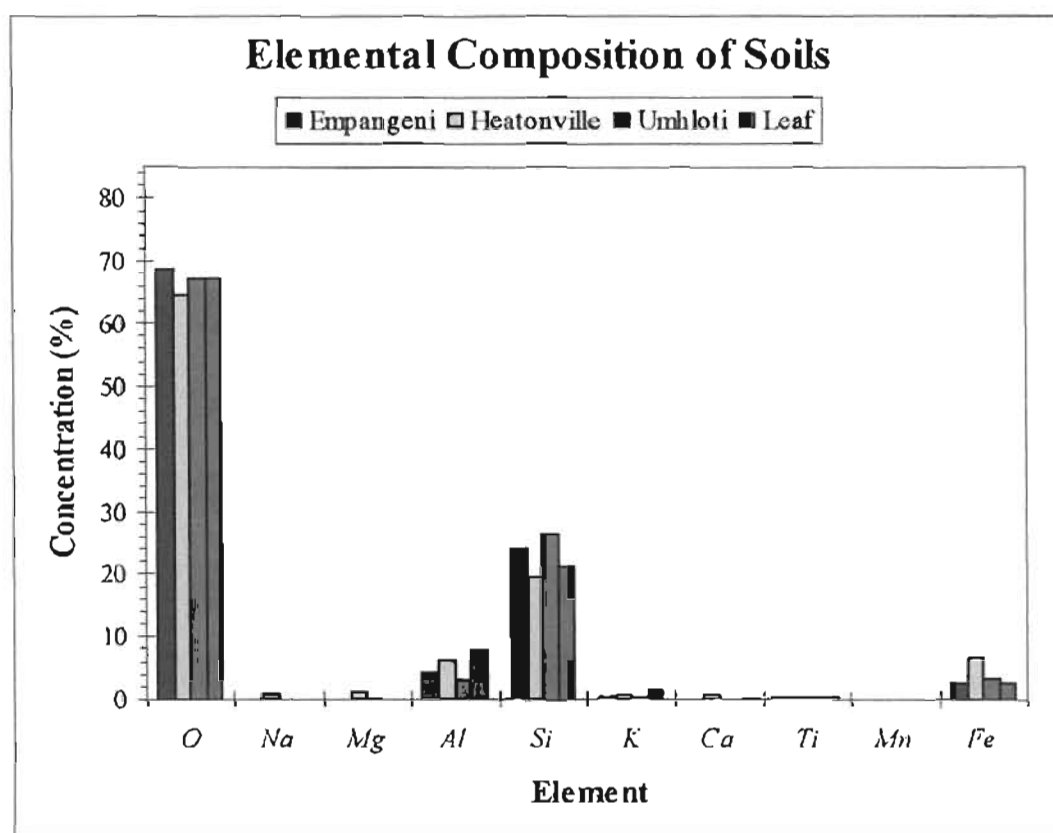
Figure 19: Mean elemental composition of four soil-types determined via *EDS*. The elemental composition of the soils are quite similar. Common elements are *O, Al, Si* and *Fe*.

Table 4: Relative elemental concentrations of shredded sugar cane by atomic weight (%). This data has been plotted in **Figure 20**.

Sugar Cane			
Element	**Min**	**Mean**	**Max**
C	12.9	14.3	17.8
N	17.9	18.5	19.2
O	67.8	71.7	81.7
Al	0.0	0.0	0.0
Si	0.0	0.0	0.0
Cl	0.0	0.0	0.0
K	0.0	0.1	0.2
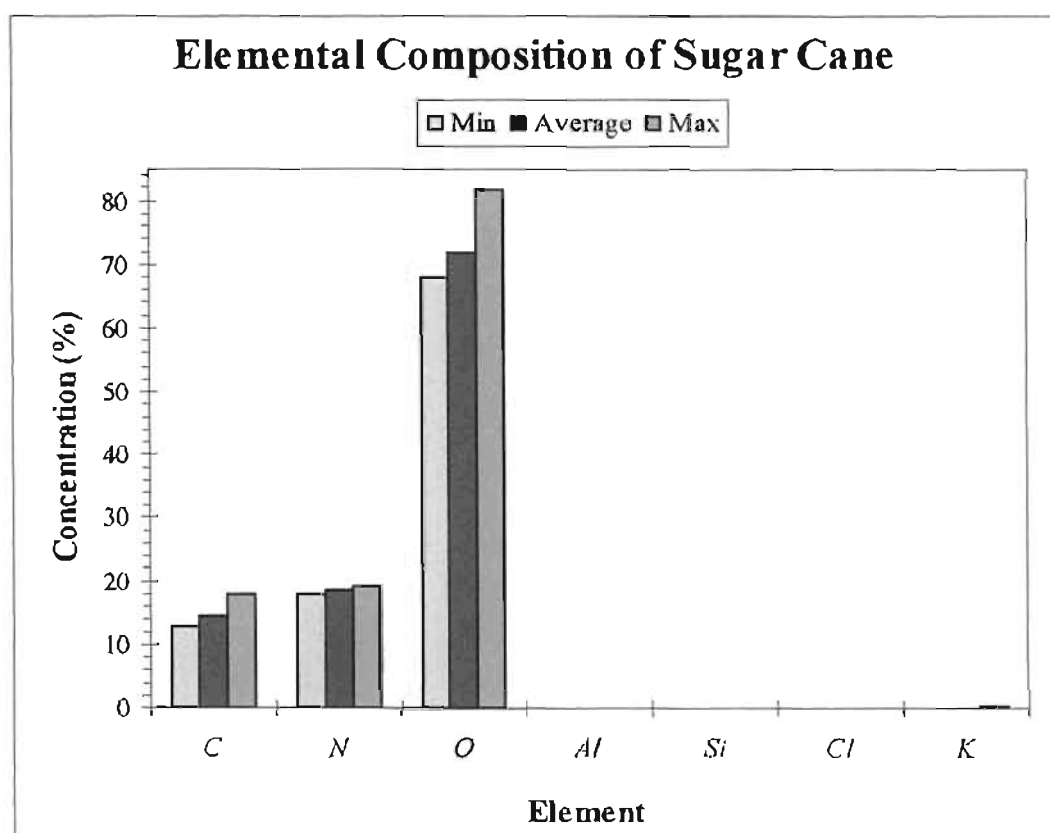
Figure 20: Elemental composition of sugar cane determined via *EDS*. Five random locations of the sugar cane were selected for analyses. From the resulting spectra, the minimum, mean and maximum concentrations of the various elements were determined. The major elements are C, N and O.

4.6. Summary

The major elements of the four soil samples were O, Al, Si and Fe. Although the soils have similar elemental compositions, the *Heatonville*-sample was found to have approximately twice as much Fe as the other soil-types.

For the sugar cane sample, the major elements were C, N and O. This was expected since cane is an organic material. Trace concentrations of potassium were also detected. This natural presence of K in the sugar cane has been reported[14] to interfere with the technique of using natural radioactivity as a soil indicator (§1.3.3).

Using average concentrations of elements present in the sugar cane and soil samples, theoretical mass attenuation coefficients were determined using *XCOM*. **Figure 21** shows a plot of μ as a function of energy for sugar cane and *Empangeni*-soil (which was the soil-type used for *DuET* and X-ray imaging).
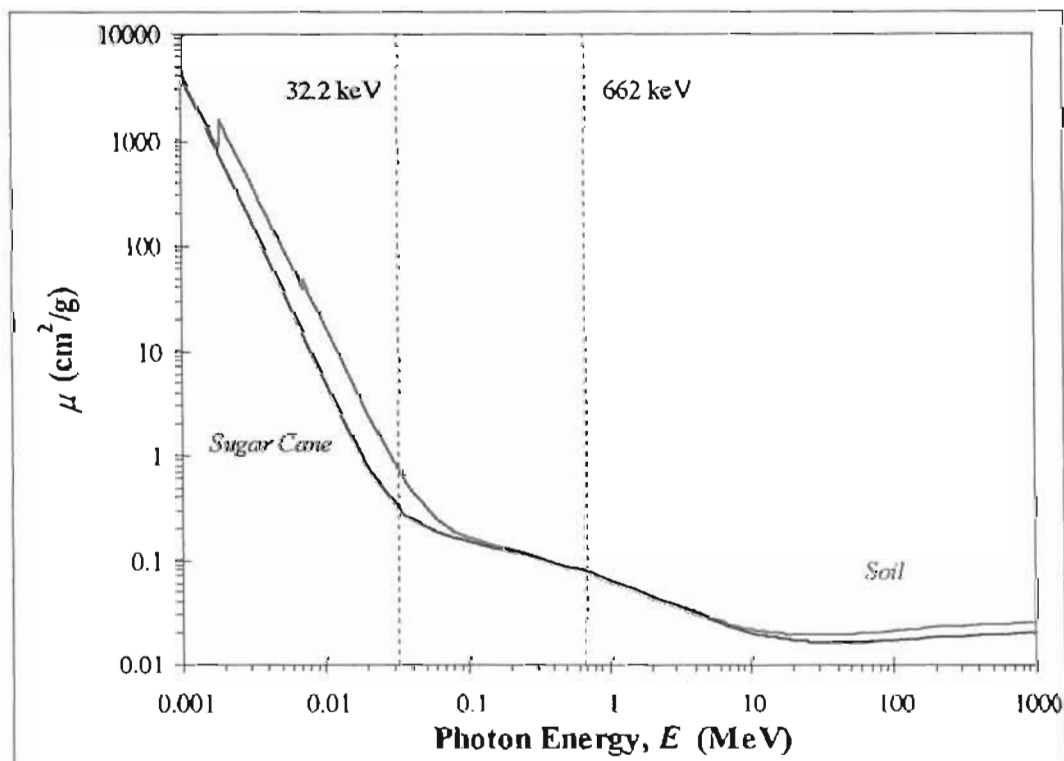
Figure 21: Mass attenuation coefficients as a function of energy for sugar cane and *Empangeni*-soil. These coefficients were obtained using *XCOM*. The μ-values of the soil appear to be greater than those of sugar cane across the energy range. The energies of interest, with respect to *DuET* for the current work, are labelled "32.2 keV" and "662 keV".

From **Figure 21**, the mass attenuation coefficients of the *Empangeni*-soil appear to be greater than corresponding values for sugar cane; this is expected since the soil contains more high-Z elements.

The energies of interest (32.2 keV and 662 keV), with respect to this project, are also indicated on the plot. There is a distinct difference in μ (~ 0.43 cm^2/g) between that of soil and cane at 32.2. keV while there is virtually no difference at 662 keV. This variation in μ at two different energies is what *DuET* exploits to deduce the relative concentrations of the components of a binary mixture.

5. Dual-Energy Transmission

DuET was briefly introduced in §1.4. The theory, for obtaining the relative concentrations of the components of a binary mixture from a *DuET*-measurement, was described in §2.5.

5.1. Apparatus

A prototype *DuET*-system, named *Sugela*, was loaned to the University of Natal (*UND*) by the *Nuclear Energy Corporation of South Africa (NECSA)*. The unit was housed in a steel box (**Figure 22**), and consisted of:

1. Two 5 μCi ^{137}Cs-sources (total activity equivalent to 0.37 MBq)
2. 2" × 2" *Crismatec NaI (Tl)*-detector
3. High voltage supply
4. Integrated amplifier and multichannel analyser.

Sugela was supplied with a single radioisotope, namely ^{137}Cs, which is in contrast to commercial *DuET*-systems, which use ^{241}Am and ^{137}Cs (see §1.4). *Sugela* was designed with the single-source configuration since it presented a number of advantages, namely:

1. only a single source has to be purchased and registered with the Department of Health, thus reducing the overall cost of the system; and
2. it is easier to mount a single source co-axially with collimation than two separate sources.

Due to a software limitation, *Sugela* was unable to integrate for periods longer than 255 s. This was a serious drawback so the nuclear electronics of the in-house system was merged with *Sugela*, that is, the sources and encasing of *Sugela* were used with the nuclear electronics and software available at *UND* (listed in **Table 5**).

(a)   (b)
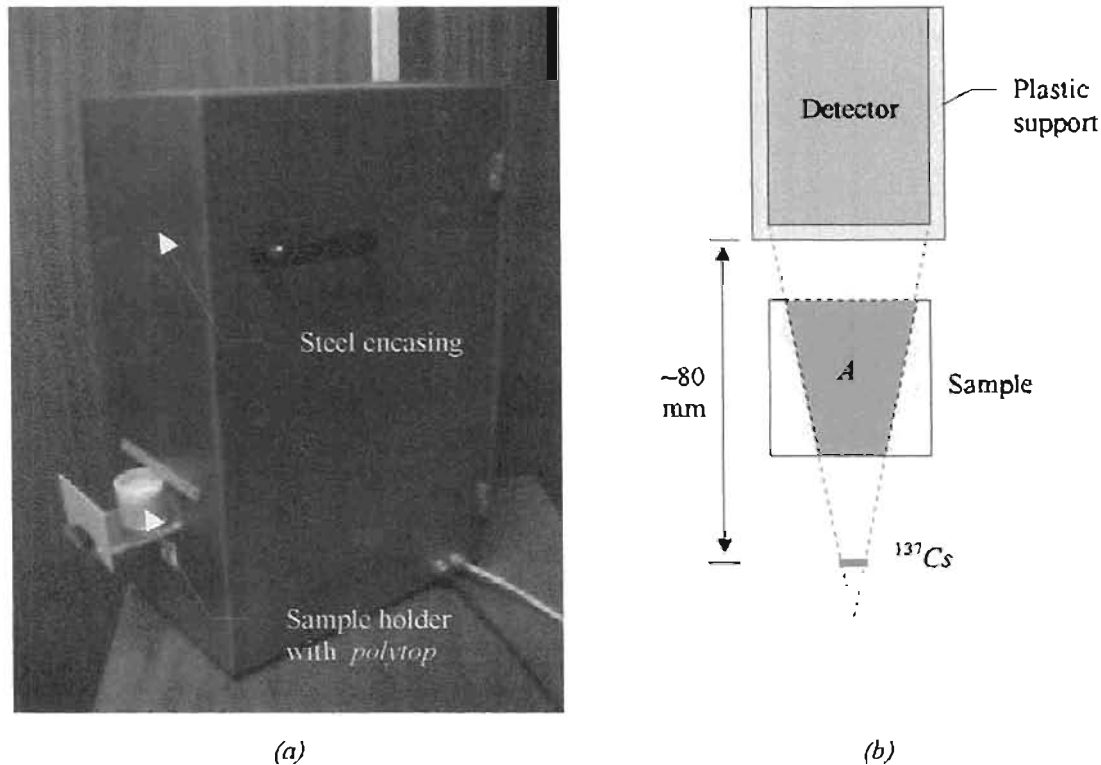
Figure 22: *(a)* A picture of *Sugela*, a prototype *DuET*-system, supplied by *NECSA*. *Sugela* utilises ^{137}Cs, in contrast to commercially-available *DuET*-systems, which use ^{241}Am and ^{137}Cs.

(b) Representation of the geometry within *Sugela*. The source was not collimated. Hence, the geometry is of the "broad beam"-type (see §2.2.2). The region, marked "*A*", indicates the volume of sample probed by the source. It was assumed that the plastic support would not significantly attenuate incident radiation. A detailed geometry is given in **Figure 36**.

Table 5: List of nuclear electronics, available at *UND*, that were used for *DuET*.

Power Supply	*The Nucleus, Inc - Quantum 8* Multichannel Pulse Height Analyzer Required detector potential = +1000 V
Detector	2" × 2" *Canberra NaI (Tl)* [Model 802-2×2] *Canberra PMT* [Model 2007]
Preamplifier	*Tennelec* TC145 Scintillation Preamplifier
Linear Amplifier	*Tennelec* TC240 Amplifier
Acquisition Card	*PCA II*

5.2. Preliminary Investigations

5.2.1. Background and Blank Spectra

Background spectra are recorded in the absence of the sample and source. Contributions to the background are due to natural radioactivity and products of cosmic interactions. A *blank spectrum* is obtained in the absence of a sample while the radioactive source is in place.

Background spectra are, in general, subtracted from sample spectra before any spectral processing (e.g. integration of peak area) is performed. Background- and blank-spectra are usually recorded over the same period as the sample spectra. **Figure 23** shows background- and blank-spectra recorded with a *NaI* (*Tl*)-detector.

Background spectra were not recorded for measurements involving *Sugela* since the sources were fixed. Due to *Sugela*'s steel encasing, it was assumed that the background contribution would be small. (This assumption was not verified.)
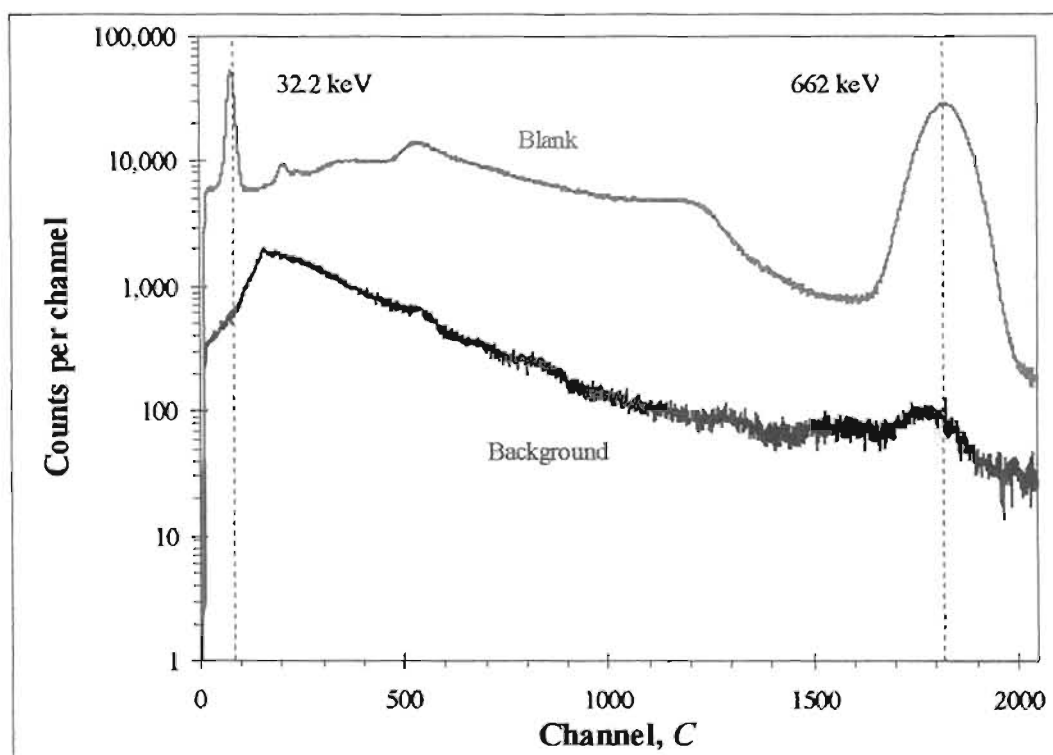
Figure 23: Background and blank spectra recorded with a *NaI* (*Tl*)-detector for an integration time of 1950 s. The blank spectrum was obtained with a [137]*Cs*-source. The low- and high-energy peaks that were used for this work are indicated on the plot.

44

All spectra were analysed in *IDL* [14]; the procedure is outlined in **Appendix B**. Values of L_0 and H_0 are obtained from the analysis of a blank spectrum.

5.2.2. Effect of Integration Time on Relative Error of R

The following investigation was carried out to briefly study the effect of integration time, t_I on the relative error of R for a single soil in cane-sample, containing 18.9 % soil. Fifty spectra, for each integration time, were recorded. The integration times ranged from 20 s to 1950 s per spectrum.

The R-value for each spectrum was determined from (23), using appropriately scaled values for L_0 and H_0. The standard deviation of the R-values for each integration time was evaluated. Then the relative error, r_R, for each integration time was obtained from equation (15).

Figure 24 shows a plot of r_R vs. t_I. As expected, the relative error drops with increasing integration times.
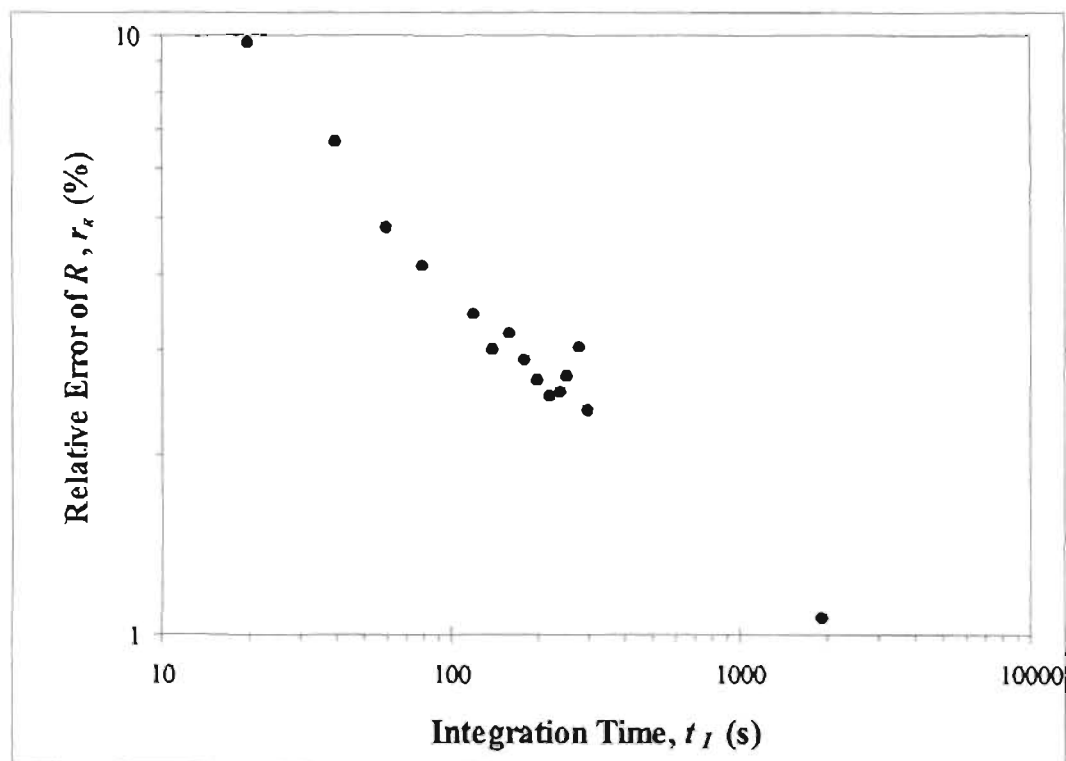
Figure 24: Variation of relative error of R, r_R with integration time, t_I. Fifty spectra were recorded for each integration time. The value of r_R decreases with increasing t_I.

---

[14] *IDL v5.4* released by *Research Systems, Inc.*: http://www.ResearchSystems.com

5.3. Demonstration of the Principle of *DuET*

5.3.1. Introduction

One of the first steps in testing a technique involves implementing it in a controlled environment. It was necessary to show that *DuET* was capable of relating an experimentally-determined quantity, R, to the concentration of one of the components in a binary mixture.

The first task was to choose an appropriate binary mixture for testing *DuET*. Liquids seemed an attractive choice due to their homogeneous nature. Mercury and bromine, being liquid elements and having differences in density, were initial choices. However, health risks and lack of availability encouraged the search for alternatives. Ferric chloride ($FeCl_3$) and water were finally chosen to represent the two components of the mixture. Various concentrations of $FeCl_3$, dissolved in water, constituted the test sample set for this initial investigation of *DuET*. **Appendix C** lists the chemical composition of the ferric chloride that was used for this work.
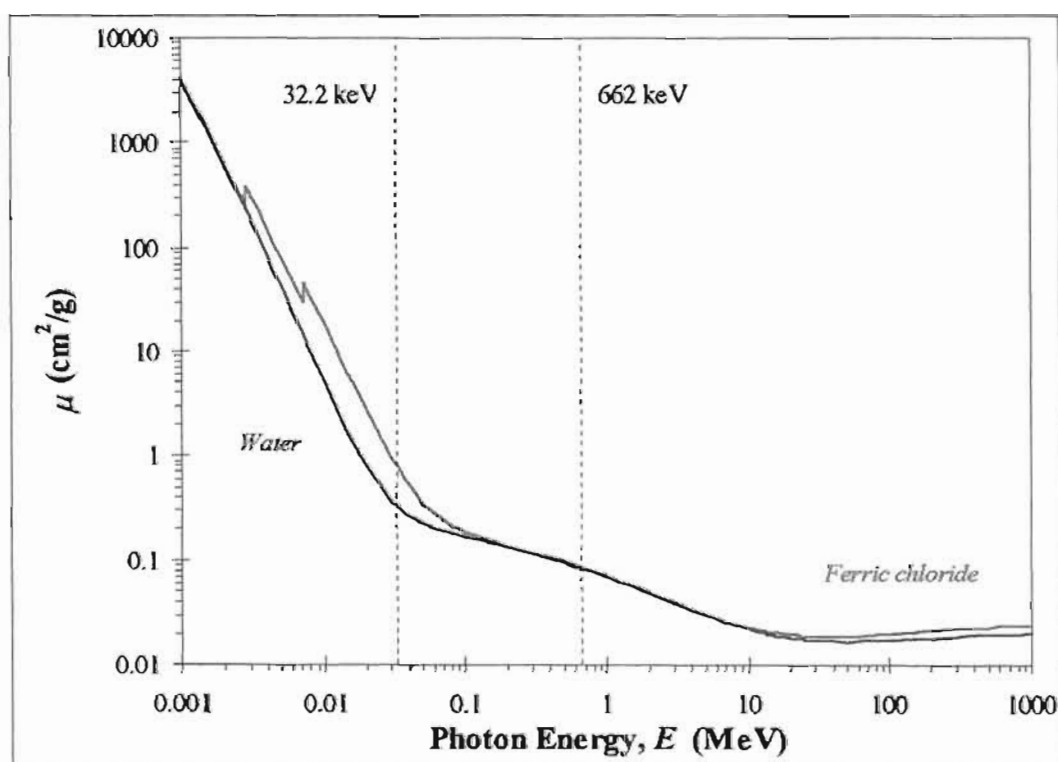
Figure 25: Mass attenuation coefficients as a function of energy for water and ferric chloride. These coefficients were obtained using *XCOM*. The μ-values for ferric chloride are generally greater than corresponding values for water.

46

One of the main requirements of the components for the binary test mixture was a significant difference in mass attenuation coefficients at the low-energy (32.2 keV, in our case). **Figure 25** above shows μ of $FeCl_3$ and water as a function of energy. The energies of interest are marked "32.2 keV" and "662 keV". There is a difference of about 0.47 cm^2/g between μ of water and $FeCl_3$ at 32.2 keV while the difference is quite small at 662 keV (~0.002 cm^2/g). This type of behaviour is similar to that seen in **Figure 21**, which compared μ of sugar cane and *Empangeni*-soil.

5.3.2. Experimental

Various amounts of $FeCl_3$ were weighed out and mixed with water. The samples were stored in *polytops*. Sample concentrations are listed in **Table 6**.

Table 6: Concentrations of aqueous $FeCl_3$-solutions used for *DuET*-measurements.

Mass of $FeCl_3$ (g)	Mass of Water (g)	[$FeCl_3$] (%)
0.80	80.54	1.0
1.63	83.53	1.9
2.48	80.86	3.0
4.21	80.07	5.0
6.80	80.11	7.8
8.82	76.37	10.4
13.80	80.42	14.6

Each of the samples was placed in the *Sugela*-unit (**Figure 22**). Forty spectra per sample, with an integration time of 1950 s per spectrum, were collected. The spectra were thereafter analysed in *IDL*.

Low- and high-energy count rates for the blank spectrum were about 435 cps and 1885 cps, respectively. Typical transmitted count rates varied between 40 and 150 cps for the low-energy. The high-energy transmitted count rate was about 1300 cps.

5.3.3. Determination of μ of Water and $FeCl_3$

The mass attenuation coefficients of water and $FeCl_3$ were determined from the recorded spectra, and then compared to semi-theoretical values predicted from *XCOM*. Adapting (24) gives

$$\mu = \left(1 - w_F\right) \cdot \mu_W + w_F \cdot \mu_F$$
$$= \left(\mu_F - \mu_W\right) \cdot w_F + \mu_W \tag{30}$$

where μ represents the mass attenuation coefficient of the mixture, the mass attenuation coefficients of water and $FeCl_3$ are represented by μ_W and μ_F, respectively. The fractional concentration of $FeCl_3$ is represented by w_F. Therefore, from a plot of μ vs. w_F, which is expected to be a straight line, values for μ_W and μ_F can be obtained from the slope and intercept.[16]

Equation (30) can be separately applied to determine μ for both low- and high-energy beams.

The height, x, of each of the samples was measured. The densities of the mixtures were calculated from the mass and volume of the samples. Then the mass attenuation coefficients of the mixtures were calculated from (10).

Using *IDL*'s LinFit-routine, a linear model of the form $y = a + bx$ was fitted to the data consisting of average μ-values for various w_F, as required by (30). Plots of μ_L vs. w_F and μ_H vs. w_F are shown in **Figure 26** and **Figure 27** for the low- and high-energy, respectively. The μ-values for water and ferric chloride were then deduced from a and b, the fitting parameters.
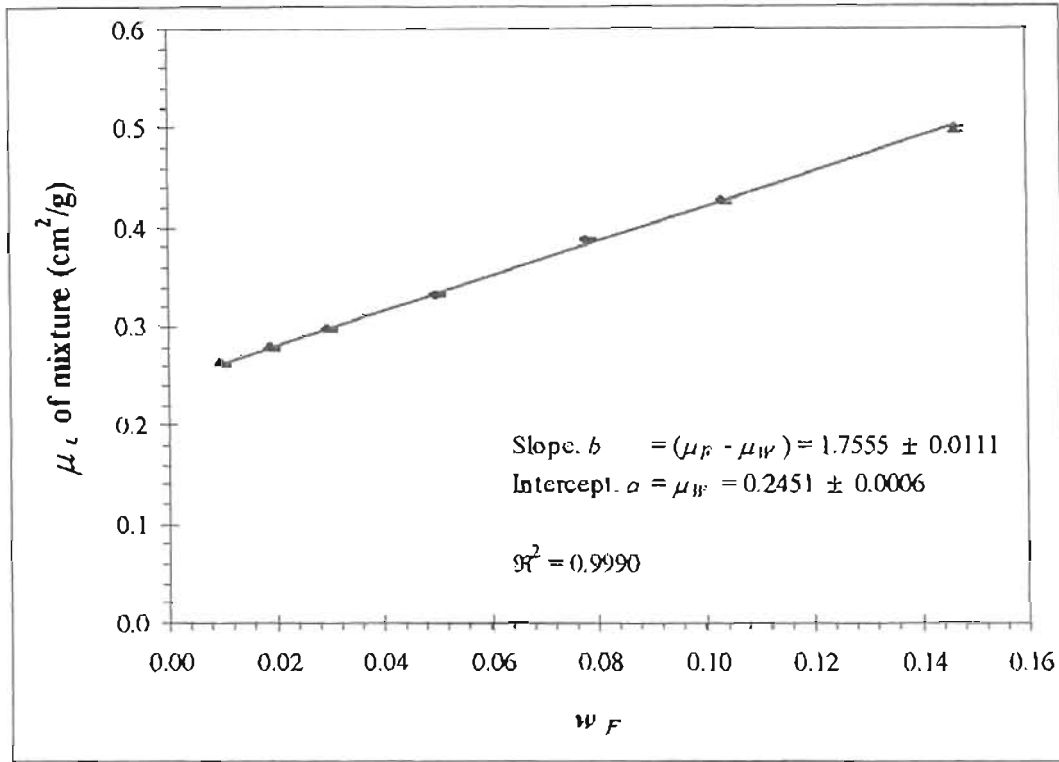
Figure 26: Plot of μ_L vs. w_F to determine the μ-values for water and ferric chloride at the low-energy. The μ-values can be determined from the slope and intercept. The $\mathfrak{R}^2$-value is quite high (0.9990) indicating good correlation between data and the linear model.
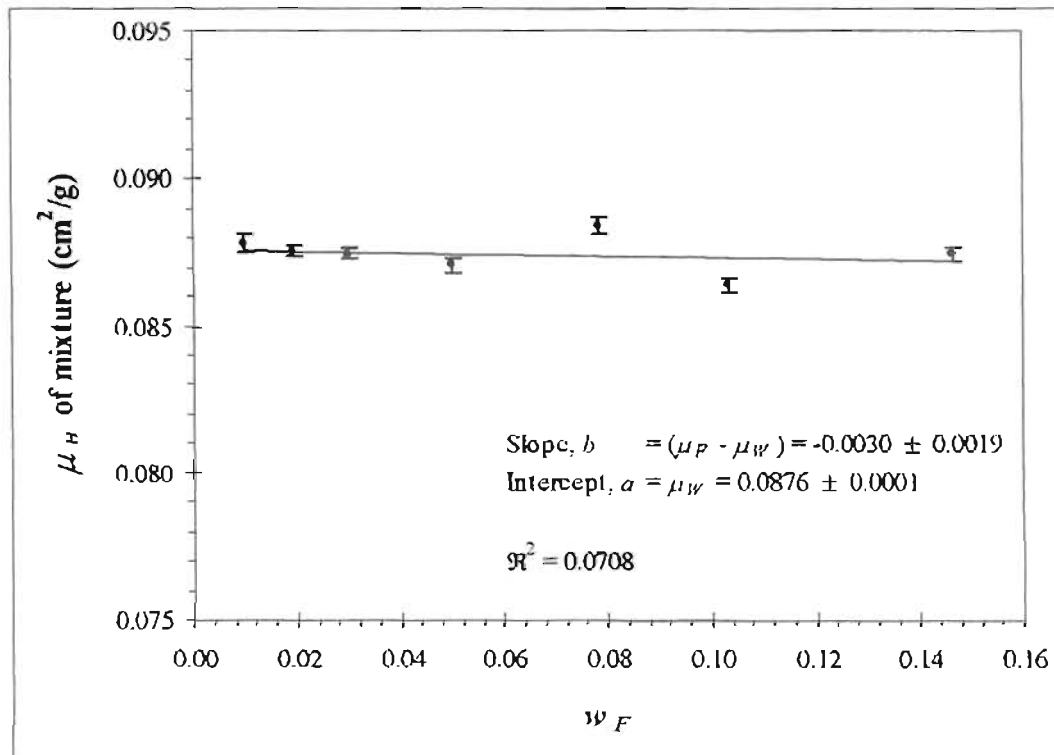
Figure 27: Plot of μ_H vs. w_F to determine the μ-values for water and ferric chloride at the high-energy. The μ-values can be determined from the slope and intercept. The low value of the slope (-0.0030) indicates that μ_H does not vary too much with concentration since the high-energy beam was expected not to be significantly attenuated. The $\mathfrak{R}^2$-value is low due to μ_H not varying linearly with concentration.

The uncertainties in the fitting parameters, as produced by LinFit, were used in calculating the uncertainties in the μ-values of water and ferric chloride. The experimentally-determined coefficients are compared with the semi-theoretical values in **Table 7**.

Table 7: Comparison of experimental μ with theoretical μ for water and ferric chloride. Theoretical μ-values are given in parentheses.

Energy	μ of Water (cm^2/g)	μ of *FeCl$_3$* (cm^2/g)
Low energy (32.2 keV)	0.2451 ± 0.0006 (0.3410)	2.0006 ± 0.0111 (0.8101)
High-energy (662 keV)	0.0876 ± 0.0001 (0.0858)	0.0846 ± 0.0019 (0.0841)

The experimental low-energy μ for water is 28.1 % smaller than the theoretical value of 0.3410 cm^2/g. For ferric chloride, the experimental μ-value at the low energy is 2.5 times greater than the theoretical value. For 662 keV, the experimental μ-values for water and *FeCl$_3$* are, respectively, 2.1 % and 0.6 % greater than the theoretical values.

The large differences in the values determined for μ of water and ferric chloride at the low energy indicate a problem. The "broad beam"-geometry could possibly contribute to the large deviation between experimental and theoretical values: the above analysis had implicitly assumed that the build-up factor was unity for the low- and high-energies. The low-energy peak, as recorded by the detector, is more susceptible to scattered photons than the high-energy peak because 662 keV photons can interact with the sample to produce lower-energy scattered photons that will be counted within the low-energy peak. However, it is unlikely that scattered photons from the 32.2 keV-line will affect the 662 keV peak. This accounts for the μ-values at 662 keV for water and ferric chloride being close to the theoretical values. Therefore, the assumption of the build-up factor being unity is valid for 662 keV where scatter does not influence the recorded counts significantly but does not hold for the low energy where there could be contributions to the peak area by scattered photons.

A second possible reason for the large deviation from theoretical μ-values at 32.2 keV could be due to the low-energy beam of ^{137}Cs being composed of multiple X-ray lines (§2.3.6). Therefore, the use of μ at 32.2. keV to represent the entire low-energy line may not be valid since each component of the multiplet would contribute counts with *unequal* fractions. **Table 8** shows three of the low-energy X-rays with their decay probabilities[15] and theoretical μ-values for $FeCl_3$. The μ-values decrease from 0.8317 cm²/g to 0.6203 cm²/g for increasing energy. Therefore, the measured value for μ could be vastly different from that expected. However, as can be seen from **Table 8**, the range of possible values of μ are still very much less than the experimental value of ~2 (see **Table 7**). High-resolution detectors, like an *HPGe-* or *Si (Li)*-detector, could be used to resolve the low-energy lines, and a more accurate value for μ could be calculated.

Table 8: Decay probabilities and μ-values for low-energy characteristic X-rays emitted by ^{137}Cs.

Energy, E (keV)	Decay probability, p	Theoretical μ of $FeCl_3$ (cm²/g)
31.8	0.0207	0.8317
32.2	0.0382	0.8101
36.4	0.0139	0.6203

5.3.4. Determination of Ferric Chloride-concentration ($[FeCl_3]$) via *DuET*

For this part of the investigation, the original data set, consisting of 40 spectra per sample, was split into two halves: a calibration set and a testing set. The first 20 recorded spectra per sample were added to the calibration set, and the remaining spectra constituted the testing set.

The calibration set was used to determine the fitting parameters of the model relating R to relative concentration, represented by equation **(26)**. Thereafter, the R-values, determined from the spectra of the testing set, were used to obtain the required

---

[15] Obtained from *Radiation Decay v2* by Charles Hacker (March 1997)

concentration of ferric chloride. In this way, the robustness of the calibration equation was tested.

The model, represented by (26), could be simply re-written as

$$R = a\left[\frac{1+(b-1)\,w_2}{1+(c-1)\,w_2}\right],$$ (31)

where w_2 represents the fractional concentration of component "2" (ferric chloride, in this case), and a, b and c are the fitting parameters, such that

$$a \equiv \left(\frac{\mu_{L1}}{\mu_{H1}}\right), \quad b \equiv \left(\frac{\mu_{L2}}{\mu_{L1}}\right), \quad c \equiv \left(\frac{\mu_{H2}}{\mu_{H1}}\right).$$

The R-value of each spectrum in the calibration set was determined from (23), and the 20 R-values per sample were then averaged. Equation (31) was then fitted to the data consisting of a mean R-value for each concentration of ferric chloride. The fitting was carried out using *IDL*'s CurveFit-routine, which computes a non-linear least squares fit to a user-supplied function. The standard deviations of the R-values were also required by CurveFit. The fitting parameters, obtained from CurveFit, are listed under **Table 9**.

Table 9: Fitting parameters for R as a function of $[FeCl_3]$. Theoretical values, as predicted from *XCOM* (see **Table 7**), are listed in parentheses.

Fitting Parameter	Value
$a \equiv \left(\dfrac{\mu_{L1}}{\mu_{H1}}\right)$	2.7543 ± 0.0018 (3.9744)
$b \equiv \left(\dfrac{\mu_{L2}}{\mu_{L1}}\right)$	9.9807 ± 0.0124 (2.3757)
$c \equiv \left(\dfrac{\mu_{H2}}{\mu_{H1}}\right)$	1.8316 ± 0.0065 (0.9803)

Using the fitting parameters from **Table 9**, the calibration equation relating R to $[FeCl_3]$ was then formulated; the calibration curve is shown in **Figure 28**. Correlation between the experimental data and the model yields an $\mathfrak{R}^2$-value of 0.9994, signifying that the model matched the data quite well.
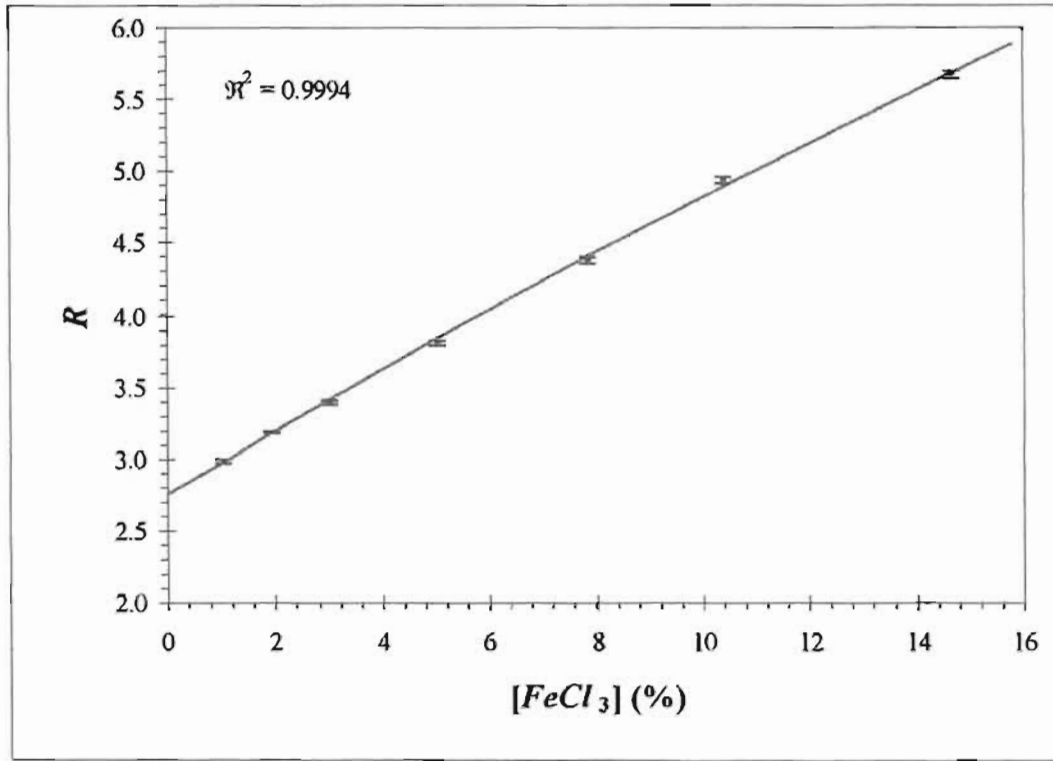
Figure 28: *DuET*-calibration curve for $[FeCl_3]$. The data points ($\bullet$) represent average R-values. obtained from the calibration set containing 20 spectra per sample, and the error bars represent standard deviations. The line (——) is a fit to the data using (31).

The next phase involved testing of the calibration equation. The inverse of equation (31), given by

$$w_2 = \frac{a-R}{(c-1)\cdot R - a(b-1)}, \tag{32}$$

was used to predict $[FeCl_3]$ corresponding to each R-value of the spectra in the test set. The results of the testing are shown in **Figure 29**.

Using the mean and standard deviations of the predicted $[FeCl_3]$-values, the relative error, r, was calculated. The variation of r with actual $[FeCl_3]$ is shown in **Figure 30** below. In general, the relative error tends to decrease with increasing concentration of $FeCl_3$.
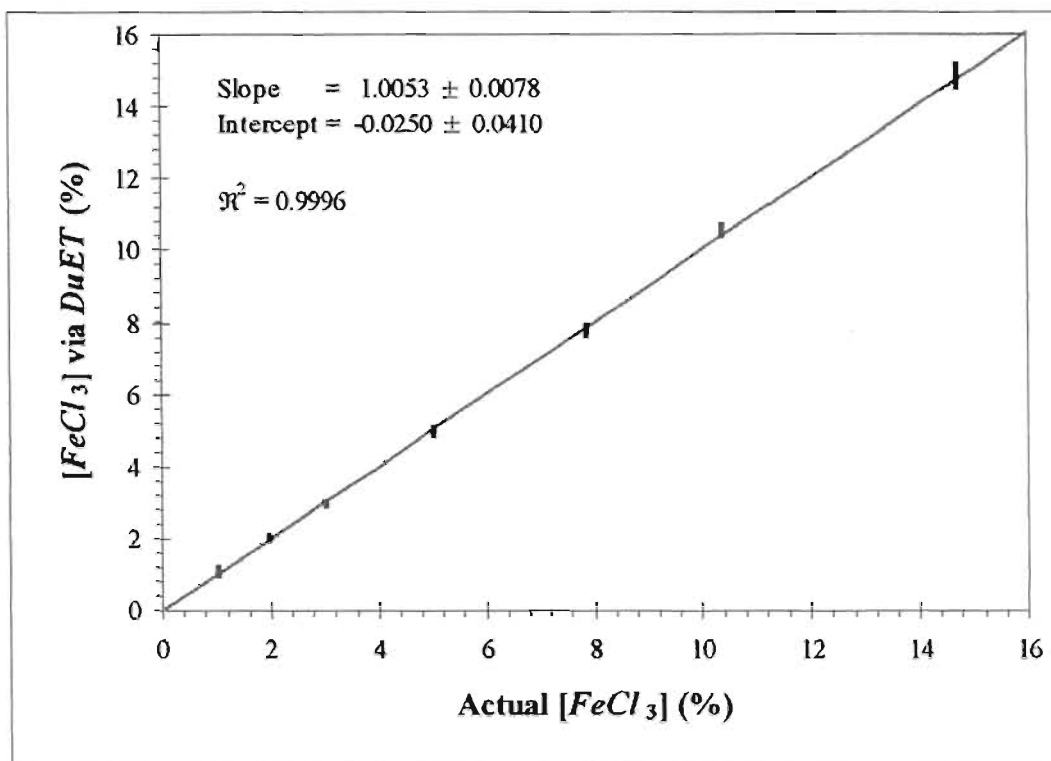
Figure 29: Comparison of the concentration of ferric chloride determined via *DuET* with the actual concentration. The set of *R*-values, calculated for the test spectra, was fed into equation (32) to predict values of [*FeCl₃*]. The line (—) represents a linear fit to the data with slope = 1.0053 and intercept = -0.0250. Ideally, the $\mathfrak{R}^2$-value and the slope would be unity, and the intercept would be zero.
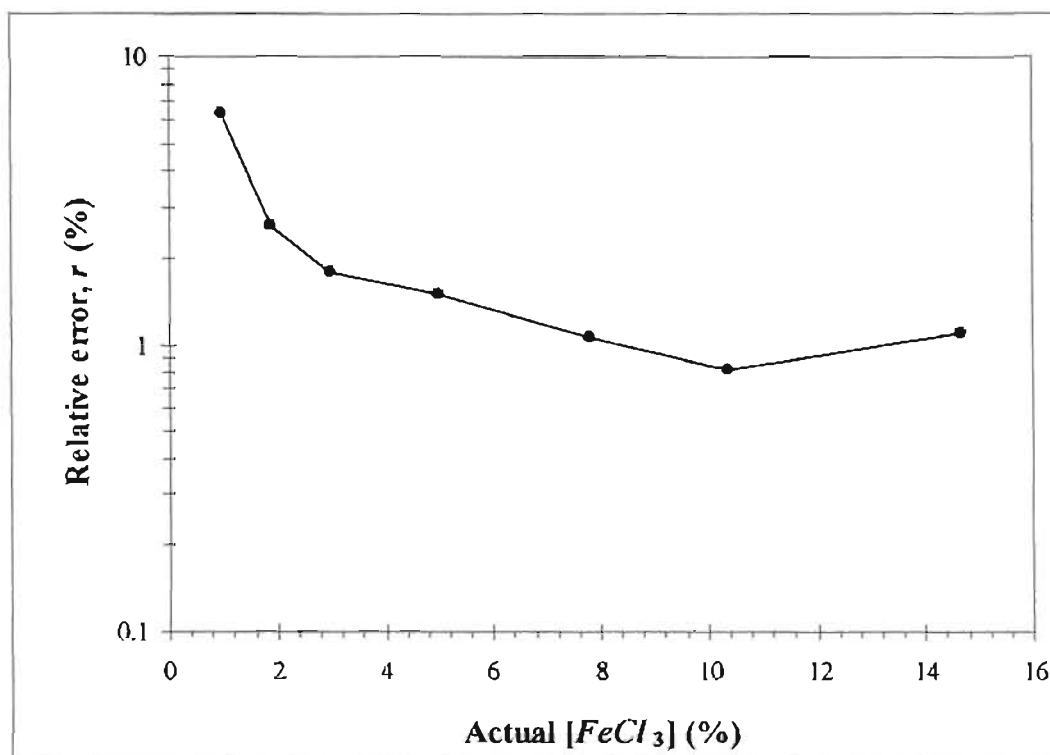
Figure 30: Variation of the relative error of predicted [*FeCl₃*] with actual [*FeCl₃*].

5.3.5. Summary

This concludes the demonstration of the principle of *DuET* using a simple binary mixture of water and ferric chloride.

DuET was successfully demonstrated as a method to determine the concentration of ferric chloride from a measurement of the transmitted low- and high-energy beams through the aqueous solutions. An $\mathfrak{R}^2$-value of 0.9996 was obtained when the calibration equation was assessed with the test spectra.

Additional calculations included determination of the mass attenuation coefficients of water and ferric chloride at the low- and high-energies. The μ-values at 662 keV for water and ferric chloride were close to theoretical values. However, the experimentally-determined μ-values at the low-energy were quite different to the theoretical values. This discrepancy could be attributed to scattered photons being counted under the low-energy peak, due to the "broad beam"-geometry. A second possible reason was that the low-energy peak is actually a multiplet, which the *NaI*-detector cannot resolve. However, the determination of possible values of μ still give values that are ~2.5 times smaller than the experimentally-determined value.

5.4. *DuET* measurements of Soil in Cane-samples

5.4.1. *DuET* measurements of Soil in Cane (t_I = 400 s)

This set of measurements involved a batch of ten soil in cane-samples with *Empangeni*-soil concentrations ranging from 1.5 % to 41.9 %. Each of the samples was placed in *Sugela*, and 100 consecutive spectra per sample were recorded; the integration time was 400 s per spectrum. Typical transmitted count rates for the soil/cane samples varied between 260 cps and 380 cps for the low-energy beam, and between 1680 cps and 1780 cps for the high-energy beam.

For each sample, the 100 spectra were split into calibration and test sets, as was done for the ferric chloride spectra (§5.3.4). The calibration set was used to obtain the calibration equation (31). The test set was then used in conjunction with the calibration equation to compare the soil concentrations obtained via *DuET* with actual concentrations.

The R-value for each recorded spectrum was obtained. For calibration, the 50 R-values for each soil concentration were averaged, and corresponding standard deviations calculated. Equation (31) was then fitted to the data consisting of soil concentration, average R-values and corresponding standard deviations. The fitting parameters, obtained from CurveFit, were:

$$a = 2.5580 \pm 0.0003, \qquad b = 2.0208 \pm 0.0005, \qquad c = 0.4666 \pm 0.0003.$$

The $\Re^2$-value for the fit was 0.9721, which indicated good correlation between data and model. A calibration equation was then formulated; the calibration curve is plotted in **Figure 31**.

The calibration equation was tested by inputting the R-value for each test spectrum into equation (32). A plot of soil concentration determined via *DuET* vs. actual soil concentration is shown in **Figure 32**. Although there appears to be a good correlation with the actual soil concentration ($\Re^2 = 0.9685$), there is a large spread of predicted concentrations for each of the samples.

Figure 31: $DuET$-calibration curve for soil in cane ($t_l = 400$ s). The data points (•) represent average R-values, obtained from the calibration set of 50 spectra per sample, and the error bars represent standard deviations. The line (—) represents a fit of equation (31) to the data.

Figure 32: Comparison of soil concentration determined via $DuET$ with actual concentration for $t_l = 400$ s. The set of R-values, calculated for the test spectra, was fed into equation (32) to obtain the soil concentration. The line (—) represents a linear fit to the data with slope = 1.0006 and intercept = 0.6876. Ideally, the slope and intercept would be unity and zero, respectively. The red dots (•) and the error bars (I) represent mean values and standard deviations, respectively, for the predicted soil concentrations.

57

The results from §5.2.2 indicated that larger integration times resulted in lower relative errors, so it was decided to increase the integration time to 1950 s per spectrum in an attempt to reduce the standard deviations of predicted soil concentrations.

5.4.2. *DuET* measurements of Soil in Cane (t_I = 1950 s)

The number of samples used in this investigation was extended to thirteen: the soil concentrations varied from 0 % to 41.9 %. Each of the samples was placed in *Sugela*, and 100 consecutive spectra per sample were recorded for t_I = 1950 s.

The procedure, that was followed for the analysis of spectra in §5.4.1 above, was repeated for this new set of spectra. The fitting parameters for the calibration equation, obtained from CurveFit, were:

$$a = 2.5118 \pm 0.0001, \qquad b = 3.2012 \pm 0.0003, \qquad c = 1.0203 \pm 0.0002.$$

The $\mathfrak{R}^2$-value for the fit was 0.9808, which indicates good correlation between data and model; the calibration curve is shown in **Figure 33**.

As carried out in the previous section (§5.4.1), the R-values from the test set were fed into equation (32), with the above fitting parameters, to predict soil concentrations. **Figure 34** is a plot of soil concentration predicted via *DuET* vs. actual soil concentration.

Correlation between predicted concentration and actual soil concentration yields $\mathfrak{R}^2$ = 0.9827, which is higher than that for t_I = 400 s ($\mathfrak{R}^2$ = 0.9685). **Figure 34** indicates that the spread of predicted soil concentrations for t_I = 1950 s are lower than that for t_I = 400 s. This difference was quantified by calculating the relative errors for predicted soil concentration; this comparison is shown in **Figure 35**. Clearly, increasing t_I has reduced the relative errors for predicted soil concentrations.
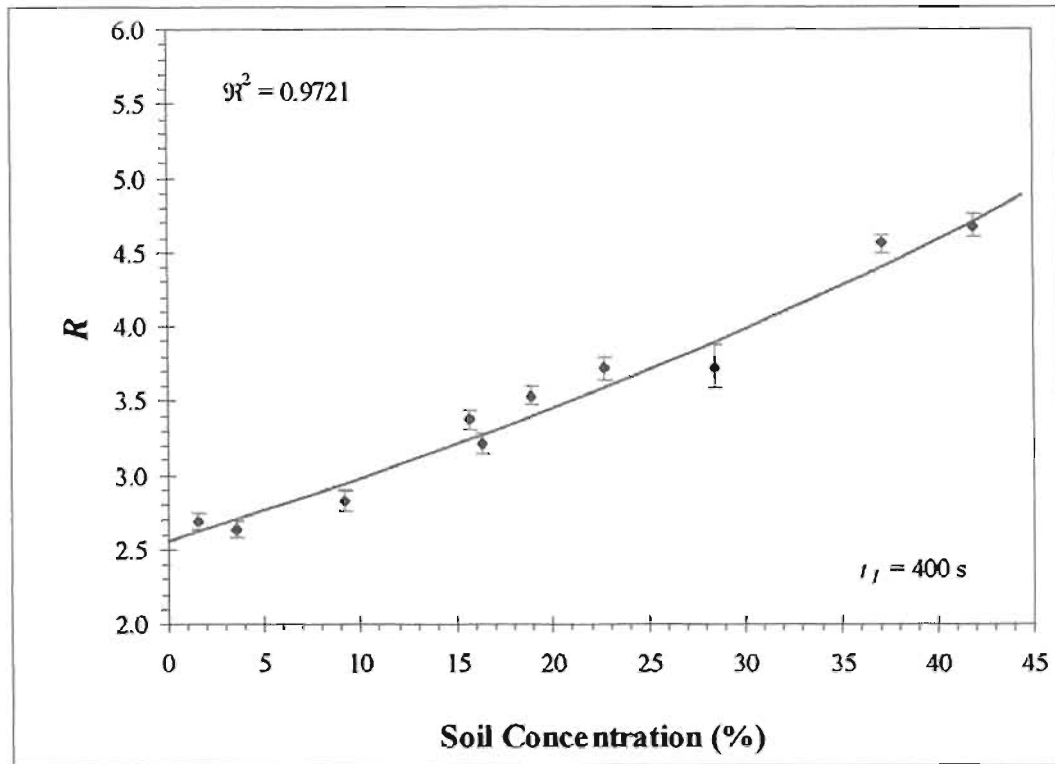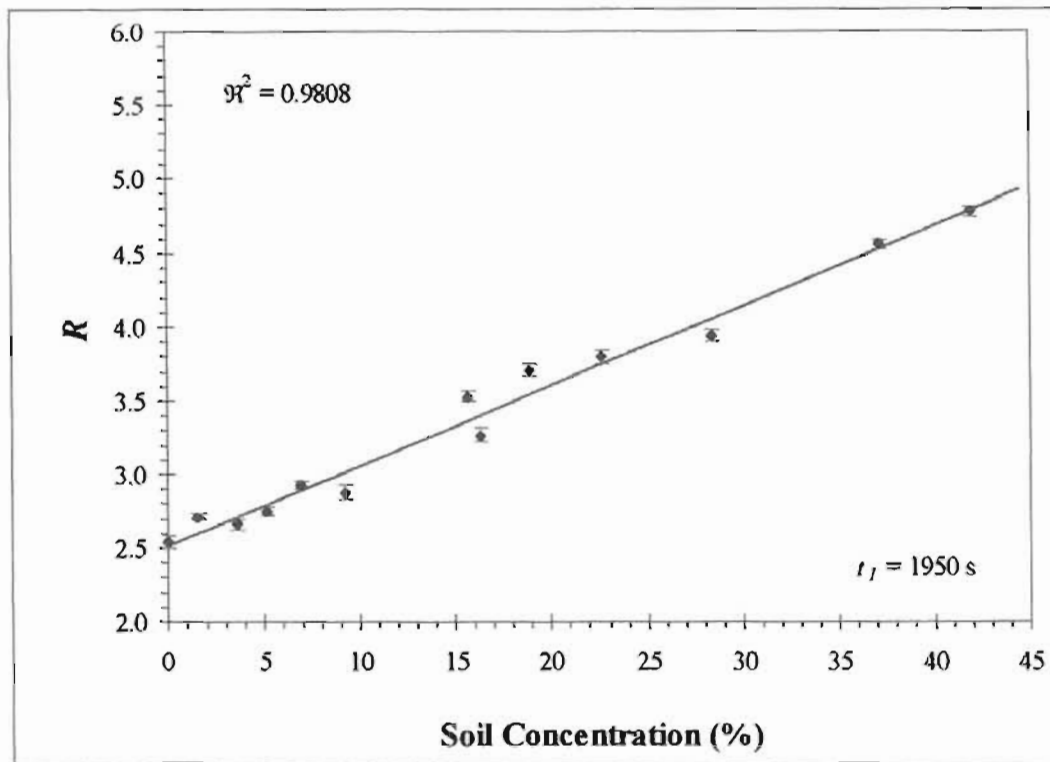
Figure 33: *DuET*-calibration curve for soil in cane (t_l = 1950 s). The data points (•) represent average *R*-values, obtained from the calibration set of 50 spectra per sample, and the error bars represent standard deviations. The line (—) represents a fit of equation (31) to the data.
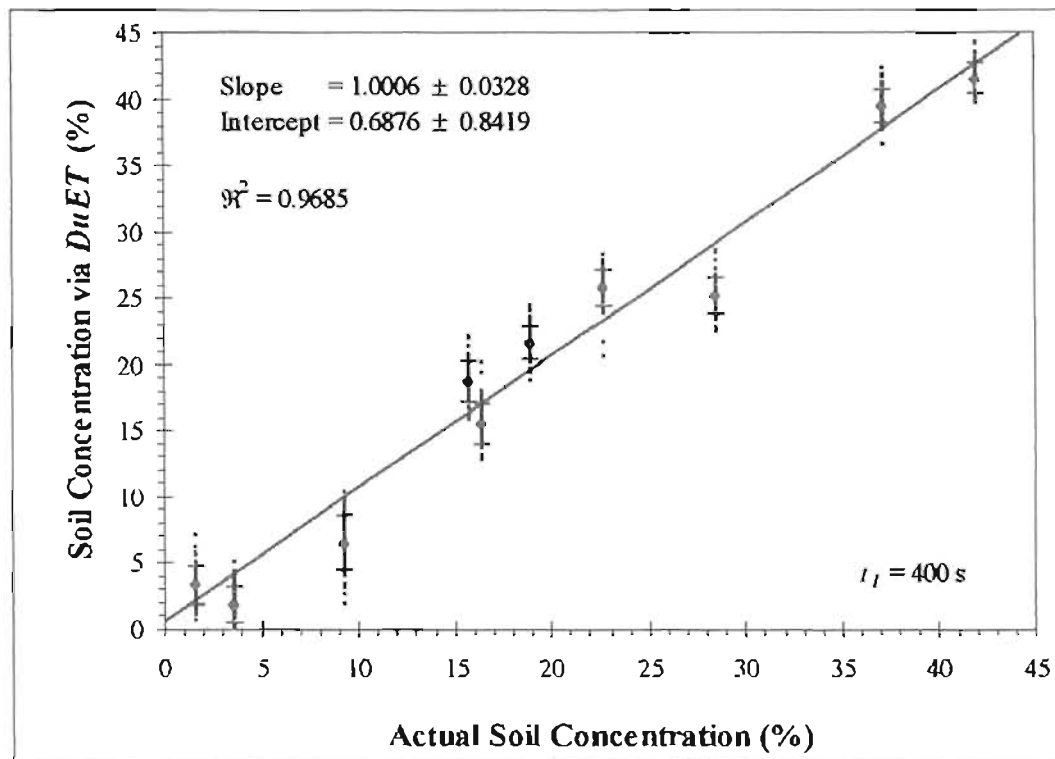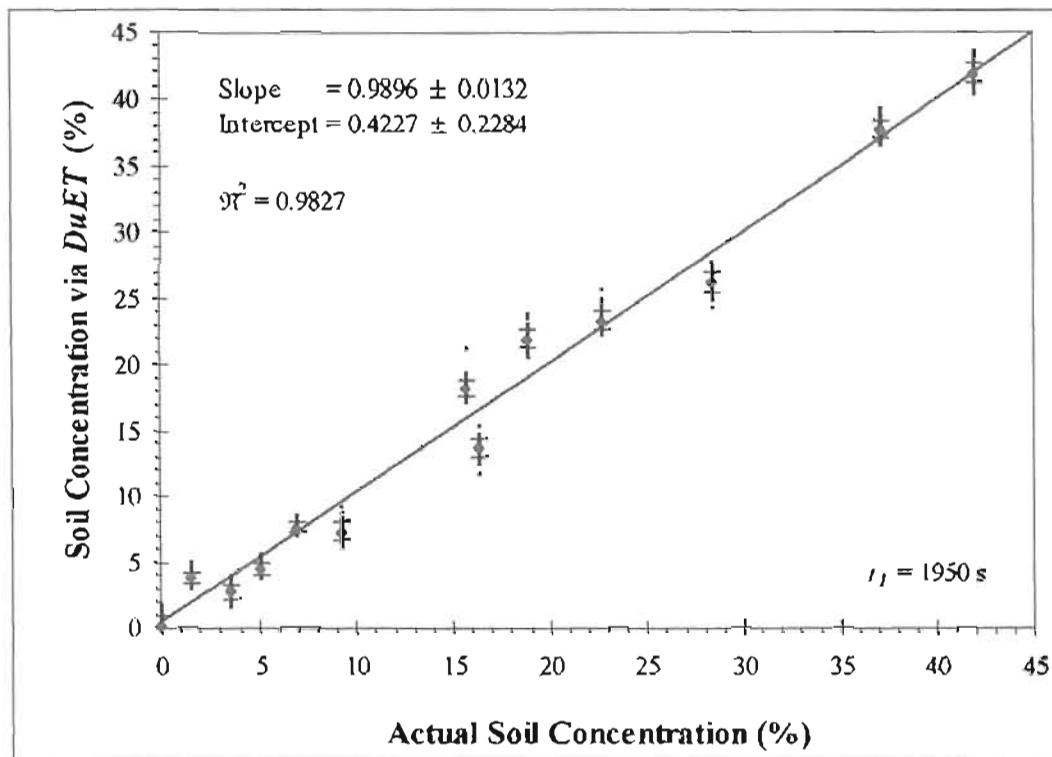

Figure 34: Comparison of soil concentration determined via *DuET* with actual concentration for t_l = 1950 s. The set of *R*-values, calculated for the test spectra, was fed into equation (32) to obtain the soil concentration. The line (—) represents a linear fit to the data with slope = 0.9896 and intercept = 0.4227. Ideally, the slope and intercept would be unity and zero, respectively. The red dots (•) and the error bars (I) represent mean values and standard deviations, respectively, for the predicted soil concentrations.
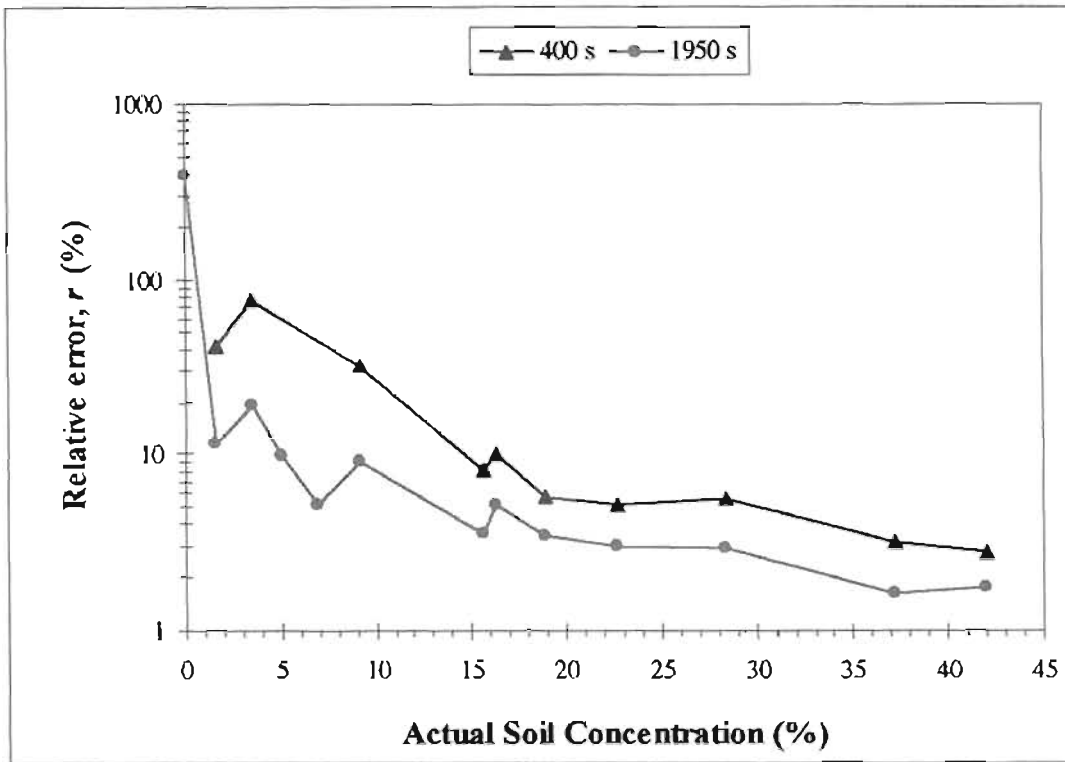
Figure 35: Comparison of the relative errors for predicted soil concentration using *DuET* for t_i = 400 s and t_i = 1950. Increasing the integration time has resulted in lower relative errors in predicted concentrations.

Figure 35 shows that the increase in integration time, equivalent to improving the counting statistics, has improved the proportionality between the predicted concentration and the actual concentration.

The results, shown in **Figure 32** and **Figure 34**, indicate that a strong correlation exists between predicted soil concentration using *DuET* and actual soil concentration. However, values for predicted concentrations conflicted with other values, that is, ambiguous soil concentrations were obtained. It is suggested that these inconsistencies were due to:

1. the scatter of photons (since a "broad beam"-geometry was used); and/or

2. the entire sample volume was not being probed by the source.

To investigate the second possibility, the fraction of the volume of the sample probed by the source was estimated by considering the internal geometry of *Sugela* (shown in **Figure 36** below).

The following assumptions were made:

1. the centre of the source is aligned with the centre of the detector (the source-detector axis); and

2. the sample container is cylindrical, with the centre of the container aligned along the source-detector axis.
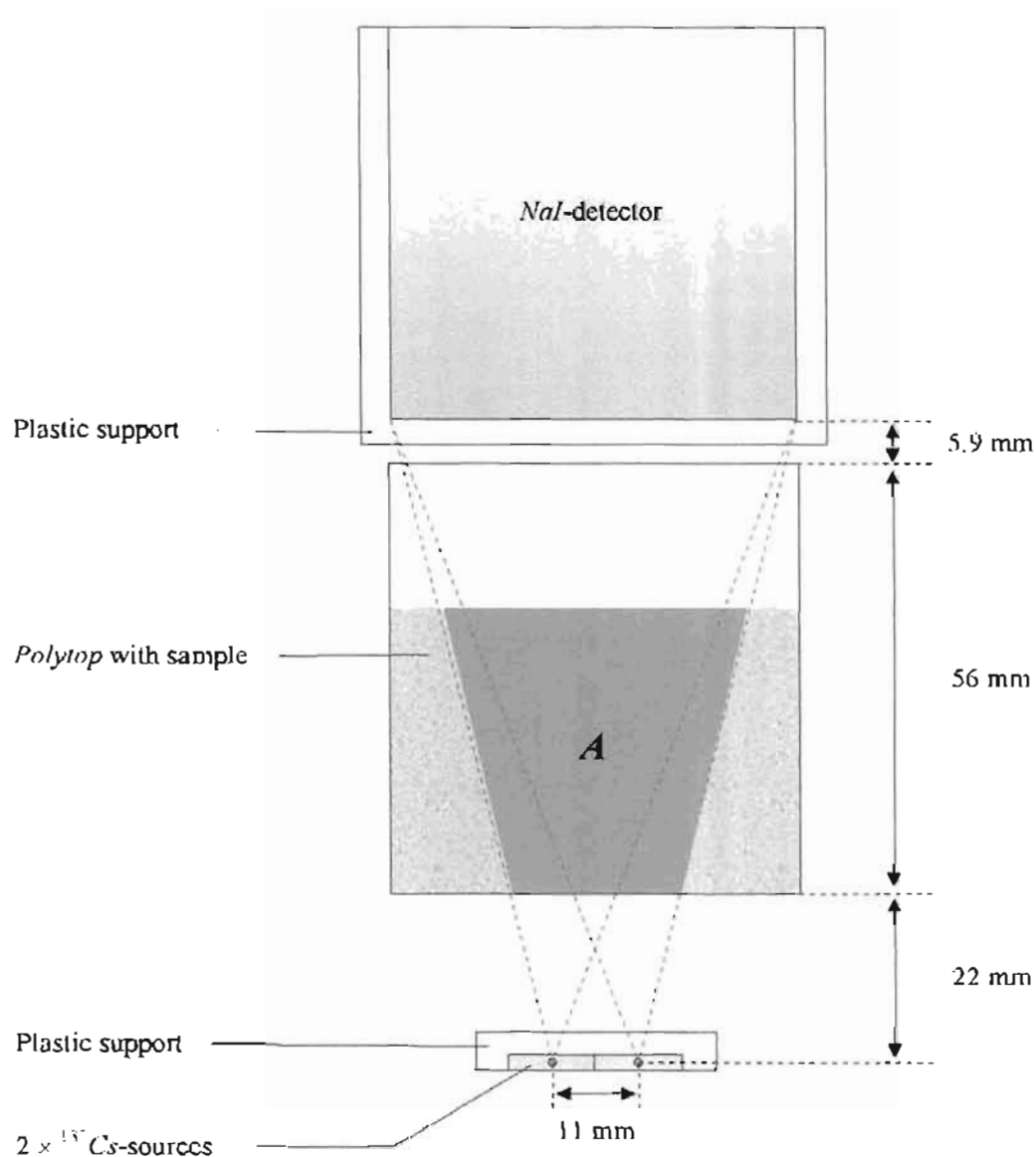
Figure 36: Source-detector geometry within *Sugela*. Region "*A*" indicates the volume of the sample that is probed by the source. Using standard geometrical considerations, it was calculated that *A* has a volume that is less than half of the total volume of the sample.

Using standard geometrical considerations of the arrangement in **Figure 36**, the volume of the sample, as seen by the source, is a frustum of a cone (region "*A*"). The volume of *A* can then be expressed as a fraction of the entire sample volume.

Considering measured heights of all the soil/cane-samples, calculated fractional volume seen by the source varied between about 35 % to 45 %. Thus, only about less than half of the sample is being probed. Secondly, no particular care was taken to ensure that the soil particles were evenly distributed through the sample volume. Thus, soil particles could be located outside region *A* in **Figure 36**. An alternative technique would be to re-distribute the particles (by shaking the sample) and recording multiple spectra per distribution.

The effect of incomplete volume scanning and scatter was probably not severe with ferric chloride due to the aqueous solutions being homogeneous.

5.5. Vertical Profiling

Since the distribution of the soil within the cane is non-homogeneous, this should lead to a variation of the intensity of the gamma rays transmitted through various vertical positions of the sample, placed on the source-detector axis. The following brief investigation was undertaken to determine the variation of *R* as a function of vertical position for a specific sample.

A new experimental layout, shown in **Figure 37** below, was constructed. The source and detector were collimated with 45 mm thick lead slabs, with 7 mm diameter holes drilled through their centres. A ~3.7 MBq ^{137}Cs-source, stronger than those of *Sugela*, was used. The source was encased in plastic.

The sample, containing 37.2 % soil, was incrementally moved to various vertical positions on the source-detector axis such that most of the sample height was spanned. A single spectrum was recorded per position, and the integration time was 1950 s per spectrum.

The primary purpose of collimation is to ensure that the incident beam is narrow to prevent scattering (see **Figure 8**). However, collimation severely reduces beam intensity. In the absence of a sample, the count rates for the low- and high-energy beams were about 20 cps and 300 cps, respectively.

The recorded spectra were analysed in *IDL*. R-values and corresponding σ_R-values were calculated using **(23)** and **(28)**, respectively. The variation of R with vertical position is shown in **Figure 38**.

(a)

(b)
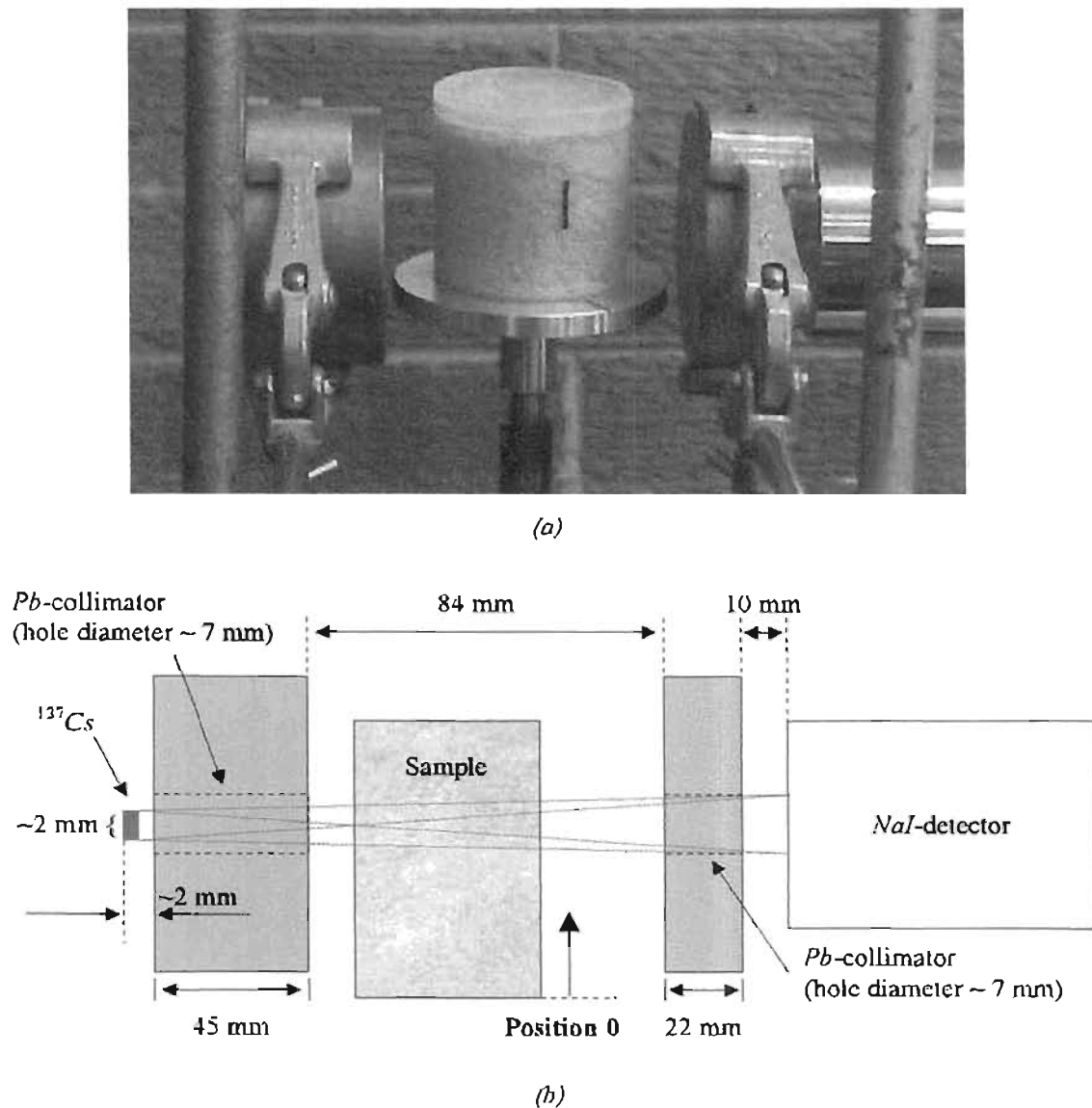
Figure 37: Experimental layout for vertical profiling measurements. *(a)* Picture of apparatus showing a *polytop* placed on top of a cylindrical base that was moved up, and *(b)* a sketch of the geometry. The region of the sample through which the beam passes is indicated by ----- .
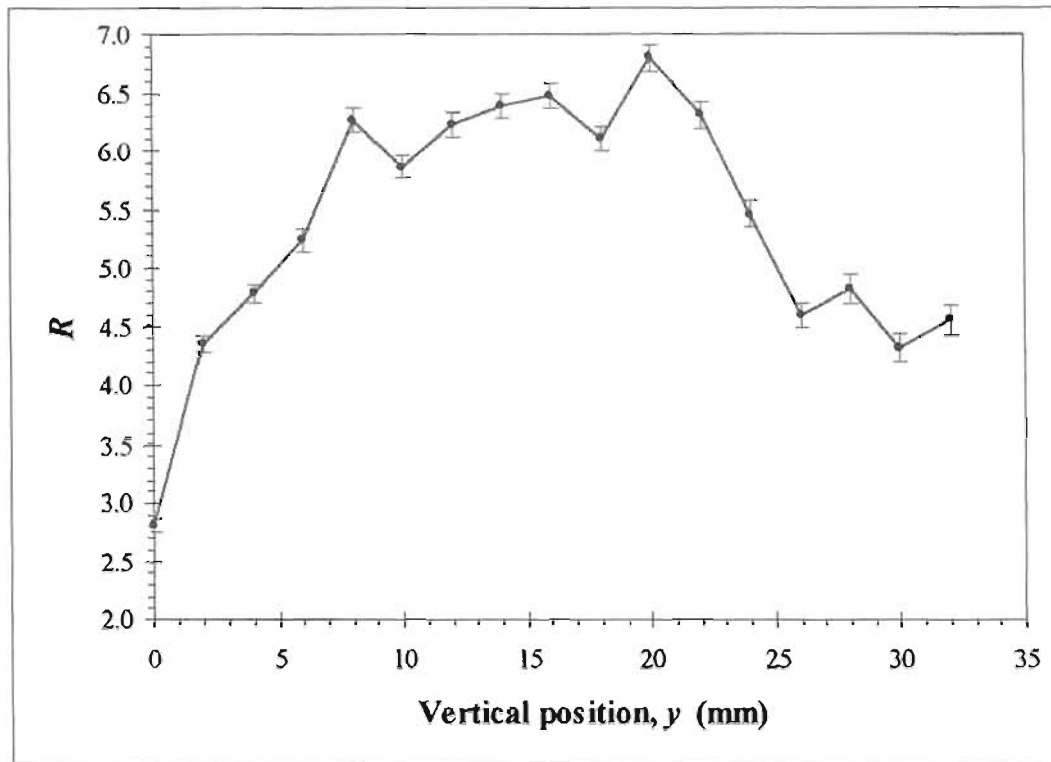
Figure 38: Variation of R with vertical position for a soil concentration of 37.2 %. The error bars are σ_R-values determined from equation (28). The sample was analysed from $y = 0$ mm to $y = 32$ mm.

From **Figure 38**, it can be seen that the R-value varies with vertical position from a minimum of about 2.8 to a maximum of 6.8. This variation is quite large, and will result in large errors in predicting the soil concentrations for the whole sample.

It can thus be concluded that if the entire sample is not probed, then the R-value is non-representative of the average soil concentration in the sample due to the non-homogeneity of the distribution of the particles within the sample volume. This was suspected in **§5.4.2**.

5.6. Dynamic Sampling of Soil in Cane-samples

In the previous section (§5.5), it was experimentally demonstrated that probing a single horizontal slice of a sample can not be assumed to be representative of the whole sample. The work described below is a preliminary investigation into an alternate experimental arrangement for *DuET*, which dynamically moves the sample through the probing gamma beams.

This new experimental layout, depicted in **Figure 39**, has a continuously moving sample platform that rotates a sample up and down through the source-detector axis. This layout was termed *dynamic*, and was conceived so that the incident beam can "see" more of the sample; it was noted in **§5.4.2** that the fixed geometry of *Sugela* enabled only about less than half of the sample to be probed by the source. With this new setup, it was hoped that estimates of soil concentration would be improved.
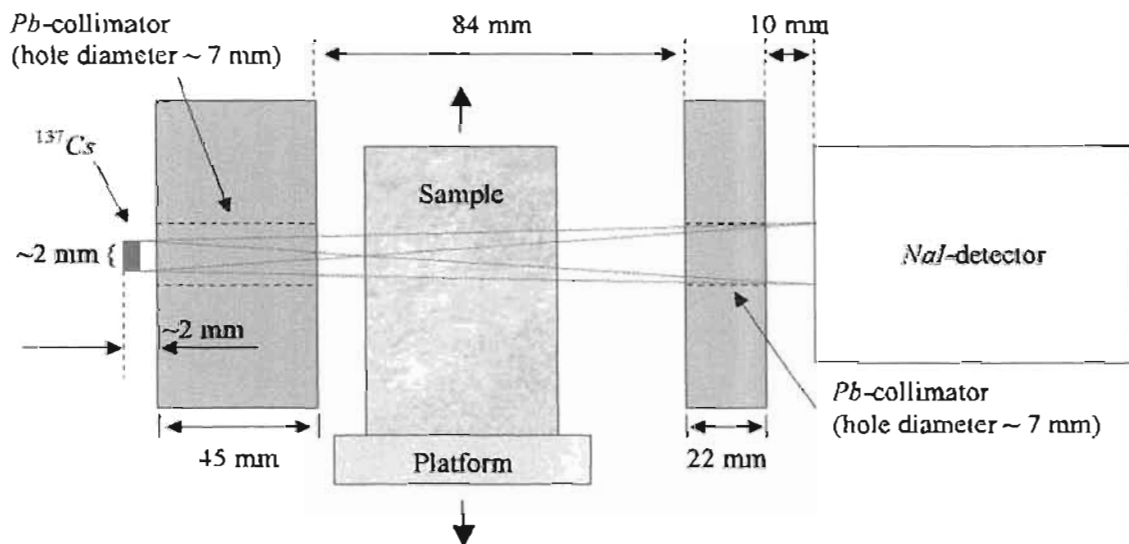
Figure 39: Schematic diagram for *dynamic*-layout. This geometry is identical to that shown in **Figure 37** apart from the sample platform, which could be rotated and moved vertically up and down between two limits (corresponding to the height of the sample). The region of the sample through which the beam passes is indicated by -----. The sample platform was driven by a 6 V DC-motor, which switched direction every time the platform reached limit switches in the vertical direction. The platform rotated at ~7 rev/min. Each revolution corresponded to a vertical displacement of 1 mm. Thus, any fixed point in the sample travels a helical path.

Each of the 13 soil/cane samples was in turn placed on the sample platform for $t_i =$ 3600 s. A single spectrum per sample was recorded.

The count rates were much lower than that recorded with *Sugela* (§5.3 and §5.4) due to the collimators (as used in **Figure 39**): in the absence of a sample, the count rates for the low- and high-energy beams were about 20 cps and 300 cps, respectively.

Following the analysis of the recorded spectra, the R-values and corresponding σ_R-values were calculated using **(23)** and **(28)**, respectively. Equation **(31)** was fitted to the data using *IDL*'s CurveFit-routine. The fitting parameters were:

$$a = 3.0330 \pm 0.0001, \qquad b = 2.0421 \pm 0.0001, \qquad c = 0.5713 \pm 0.0001.$$

Figure 40 shows a plot of the variation of R with soil concentration for this *dynamic*-arrangement. There is a strong correlation between the data and the model represented by **(31)** since the $\mathfrak{R}^2$-value is 0.9828.
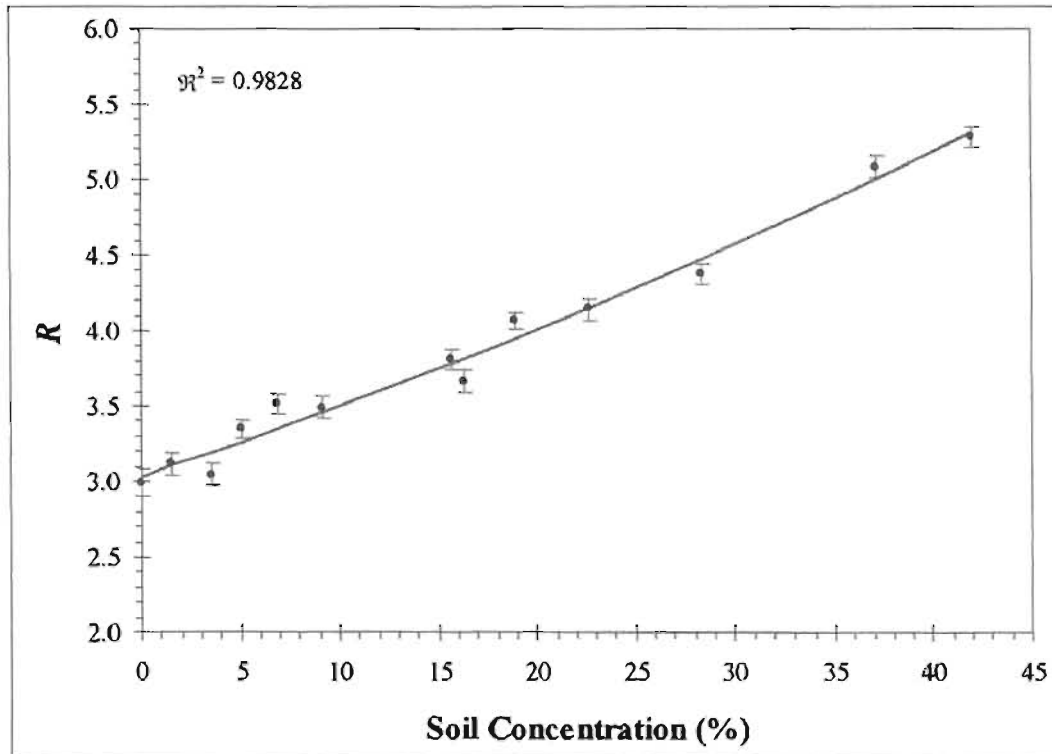
Figure 40: Variation of R with soil concentration using the *dynamic*-setup. Each data point represents the result from a single measurement for an integration time of 3600 s. The error bars are σ_R-values determined from equation **(28)**. The line (—) represents a fit of equation **(31)** to the data.

Inputting the R- and corresponding σ_R-values in equation (32), the soil concentrations were then predicted. This was not a rigorous testing of the calibration equation since a proper (and more complete) test set of spectra was not recorded. The predicted soil concentration vs. actual concentration is plotted in **Figure 41**.
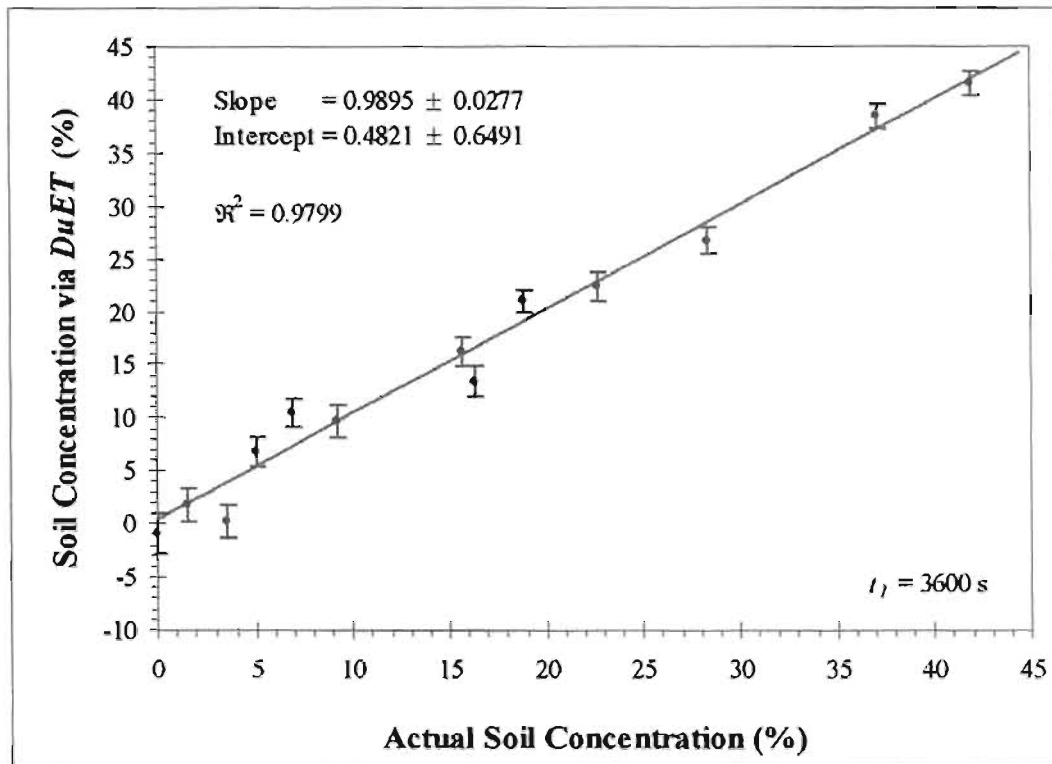
Figure 41: Comparison of predicted soil concentration via *DuET* with actual concentration using the *dynamic*-setup. The set of R-values, used to create the calibration equation, was fed into equation (32) to obtain soil concentrations. The error bars were calculated by feeding $(R + \sigma_R)$ and $(R - \sigma_R)$ in equation (32) to obtain minimum and maximum values for predicted soil concentrations. The line (—) represents a linear fit to the data with slope = 0.9895 and intercept = 0.4821.

Although a linear trend exists between predicted and actual soil concentration (**Figure 41**), it is not clear whether this dynamic arrangement had any impact in reducing the error bars for soil concentration (c.f. **Figure 34**). A more conclusive comparison could be obtained by using a stronger source, stronger collimation (i.e. smaller beam diameter) and recording more spectra per sample.

5.7. Summary

DuET was successfully demonstrated as a technique to measure the relative concentrations of the components of a binary mixture. This was confirmed by using a homogeneous mixture of water and ferric chloride (**Figure 29**).

The *DuET*-technique was then applied to the problem of measuring the amount of soil in a soil/cane-mixture. Although strong correlation existed between R and soil concentration, testing of calibration equations revealed large variations in predicted concentrations for different soil concentrations (**Figure 32** and **Figure 34**). These large deviations were not encountered for the ferric chloride-measurements. The incomplete probing of the sample volume together with the influence of scatter due to the "broad beam"-geometry were suggested as possible causes for the variation of the predicted soil concentrations.

Vertical profile-measurements on a single sample showed that the non-homogeneous distribution of soil particles within the cane resulted in a wide range of R-values being calculated for the same sample.

An improved experimental arrangement was constructed in order to move the whole sample through the incident low- and high-energy beams. However, a further investigation is required to determine whether such an arrangement improves estimates of soil concentration. The implementation of multi-detector configurations, similar to that suggested in [20], might be able to compensate for the use of "broad beam"-geometries.

6. The Analysis of *DuET*-spectra via Artificial Neural Networks

6.1. Introduction

The standard approach to analysing experimental data is to relate the observables via one or more mathematical relations. This then enables the prediction of outcomes for a given set of inputs. However, in practice, the variables of real systems have tolerances. Therefore, imposing a mathematical function upon the system is too rigid, and this can lead to large deviations between expected and actual results. Another problem often encountered is that the functional form of the defining equations cannot be easily determined.

The *artificial neural network* (*ANN*) can be used as an alternative to representing systems via inflexible mathematical functions. This approach also represents a significant paradigm shift with respect to scientific methodology: an *ANN* can be visualised as a "black box" that accepts inputs and produces required outputs, and the inner mechanisms of this "black box" need not be understood. Therefore, any number of variables can be fed into the *ANN*, with the hope that the neural network is able to create the correct input-output mapping.

The *Discrete Wavelet Transform* (*DWT*) has, in recent years, become a powerful signal-processing tool; its most notable application is in data reduction.

As an alternative to using curve-fitting and regression for analysing *DuET*-spectra, described under **Chapter 5**, it was decided to explore the use of an *ANN*. However, using the entire 2048 channels of the *DuET*-spectra as inputs to an *ANN* would cause the neural network to perform inefficiently. It was therefore necessary to reduce the number of input variables. This task was to be performed by the *DWT*.

Using this *DWT-ANN* methodology will enable determination of the relative concentrations *directly* from the *DuET*-spectra without any intermediate curve-fitting

and regression. This method can also be generalised to any application involving large data sets with many input variables.

6.2. Artificial Neural Networks

6.2.1. Overview

There are many possible configurations (or *topologies*) of *ANNs*; these vary according to the requirements of a specific application. The type of *ANN* that was used for the present work was the *multi-layer perceptron* (*MLP*) or *multi-layer feed-forward neural network*. The *MLP* is regarded as one of the most popular network topologies in use today due to its ability to learn almost any input-output mapping.

A good introduction to the multi-layer feed-forward neural network is given in [21]. A review of some example applications of *ANNs* to problems in chemistry are also presented. References to spectroscopic applications involving *ANNs* are also included.

Morgan *et al.*[22] described an application of neural networks for the determination of the electron temperature, T_e and density, N_e of a plasma. The inputs to the *ANN* are the intensities of nine spectral lines. Another *ANN* was trained to calculate plasma line ratios, given T_e and N_e as inputs.

The analysis of gamma spectra via neural networks is not new. Olmos *et al.*[23] used the *associative memory* neural network-topology to automatically identify and quantify the radionuclide components in a mixture.

Keller *et al.*[24] proposed a system incorporating a gamma spectrometer coupled to an artificial neural network. The unit was to perform real-time, automatic identification of concentrations of a set of radioisotopes. The neural network component was to prevent the need for often time-consuming and complicated mathematical curve-fitting to obtain the required concentrations. No data reduction of the input spectra to the neural network was to be performed.

From [24], it has been gathered that an *ANN*-approach is suited to those cases where fast processing speeds are required and the need for extreme precision is not significant.

An important advantage of an *ANN* is that no matter how long it takes to train (hours or even days), once trained the output is quickly computed by a simple matrix multiplication of the input variables.[22]

6.2.2. Training and Testing of an *ANN*

Most neural network topologies, including the *MLP*, involve exposing the *ANN* to a set of input data with known output values. This is termed the *training* (or *learning*) *phase*. A *weight matrix*, which relates the input variables to the output space, is continually adjusted in order to minimise the error function between the desired outputs and that which the network predicts. The error function or *mean squared error (MSE)* is usually defined by [16]

$$MSE = \frac{1}{NP} \sum_{j=1}^{P} \sum_{i=1}^{N} \left(d_{ij} - y_{ij} \right)^2 , \qquad (33)$$

where P is the number of output processing elements (the outputs), N is the number of exemplars (or elements) in the training data set, y_{ij} is the network output for exemplar i at processing element j, and d_{ij} is the desired output for exemplar i at processing element j.

The training process requires large amounts of data and/or time (depending on network topology and complexity of the problem). The training data must span a reasonable range of typical data, and must not contain any spurious or ambiguous information. In general, the *ANN* cannot be expected to perform successfully when faced with data outside the range with which it was trained. The input-output mapping created by an *ANN* is generally a non-linear one.

---

[16] Adapted from *NeuroSolutions v4.13* Online Help; *NeuroDimension, Inc*; 2001: http://www.nd.com

Cross-validation is one of the methods used to prevent *overtraining* from occurring[21]. An *ANN* is said to have been overtrained when it loses the ability to generalise. In other words, the *ANN* learns individual training exemplars, and is thus unable to interpolate or extrapolate beyond the training data. Cross-validation data, which is a smaller representative training set, is provided during training so that learning is terminated when the *MSE* of the cross-validation set increases.

After the training phase, the ability of the network is tested with a set of *unseen* data that was not used for training. If the network performs adequately, it can then be implemented in the application. Otherwise, the *ANN* may need to be redesigned.

*ANN*s were initially designed to be implemented in hardware, that is, executed by analog multipliers given various inputs. However, many software programs have been written recently that *simulate* the workings of neural networks. The software package that was used for the current investigation was *NeuroSolutions*[17].

6.3. The Discrete Wavelet Transform

6.3.1. Overview

The *Discrete Wavelet Transform*[25] is a mathematical operation that involves multiple matrix multiplications of a given data vector and a *wavelet coefficient matrix (WCM)*. The *WCM* embodies two operations equivalent to low- and high-pass filtering. In general, the *DWT* acts on a data vector having a length equal to a power of two, producing a vector of the same length.

The elements of the *WCM* are characteristic of a set of specific *basis functions* that defines the mapping from one vector space to another. There are infinitely numerous basis functions but with respect to the *DWT*, the functions of interest are those that satisfy specific conditions[25]; these basis functions are termed *wavelets*. The wavelet basis used for the current investigation was *Daubechies-6* (also known as *DAUB6* or D_6), named after its discoverer, Ingrid Daubechies.

---

[17] *NeuroSolutions v4.13* released by *NeuroDimension, Inc.*: http://www.nd.com

D_6 has six coefficients: c_0, c_1, c_2, c_3, c_4, c_5. A typical *WCM*, representing the basis of D_6 is shown in **(34)** below.

$$W_8 = \begin{pmatrix} c_0 & c_1 & c_2 & c_3 & c_4 & c_5 & & \\ c_5 & -c_4 & c_3 & -c_2 & c_1 & -c_0 & & \\ & & c_0 & c_1 & c_2 & c_3 & c_4 & c_5 \\ & & c_5 & -c_4 & c_3 & -c_2 & c_1 & -c_0 \\ c_4 & c_5 & & & c_0 & c_1 & c_2 & c_3 \\ c_1 & -c_0 & & & c_5 & -c_4 & c_3 & -c_2 \\ c_2 & c_3 & c_4 & & & & c_0 & c_1 \\ c_3 & -c_2 & c_1 & -c_0 & & & c_5 & -c_4 \end{pmatrix} \quad (34)$$

W_8 will act on a data vector with a length of 8. Blank entries represent zeroes.

The structure of W_8 is intriguing. The first row consists of

$$c_0, c_1, c_2, c_3, c_4, c_5 \quad (35)$$

while the second row consists of

$$c_5, -c_4, c_3, -c_2, c_1, -c_0. \quad (36)$$

Subsequent, odd and even rows are formed by two-column shifts of the six elements in **(35)** and **(36)**, which represent the low- and high-pass filtering, respectively (as mentioned earlier).

The results of the low-pass filtering **(35)** are termed the *smooth-components* (denoted by s_i and S_i in the following discussion), and that of the high-pass filtering **(36)** are the *detail-components* (denoted by d_i and D_i).

Since any *WCM* is defined to be *orthogonal*, the inverse matrix is simply obtained by taking the transpose[18] of the *WCM* [25].

---

[18] The transpose of a matrix is obtained by converting all columns to rows or rows to columns.

6.3.2. Implementing the *DWT*

The *pyramidal algorithm*[125] is one of the methods used to compute the *DWT*. It involves applying the wavelet coefficient matrix, like W_8 in **(34)**, *hierarchically* in a process of multiple matrix multiplications and permutation of coefficients.

Consider a data vector of 8 ($= 2^3$) elements: $Y = \{y_i, i = 1, 2, ..., 8\}$. Let W_N represent an ($N \times N$)-wavelet coefficient matrix. **Figure 42** describes the process of the pyramidal algorithm. The first step involves applying W_8 to Y. The result is a matrix M_1 of length 8 consisting of *smooth-* and *detail*-terms as denoted by s_i and d_i, respectively. The elements of M_1 is then permuted such that the s_i-terms are ordered and placed before the d_i-terms. The resulting matrix is labelled O_1. W_4 is then applied to the first half of O_1 such that the d_i-terms are left unaffected. M_2 is then formed, and then permuted. The process continues until a trivial number of s_i-terms (usually two) remain. The result is a set of the remaining *smooth*-components (S_1 and S_2 in **Figure 42**) and all the *detail*-coefficients (d_i and D_i) that were collected through the process; the resulting components are referred collectively as the *wavelet coefficients*[125].

$$Y \xrightarrow{W_8} M_1 \xrightarrow{\text{Permute}} O_1 \xrightarrow{W_4} M_2 \xrightarrow{\text{Permute}} O_2$$
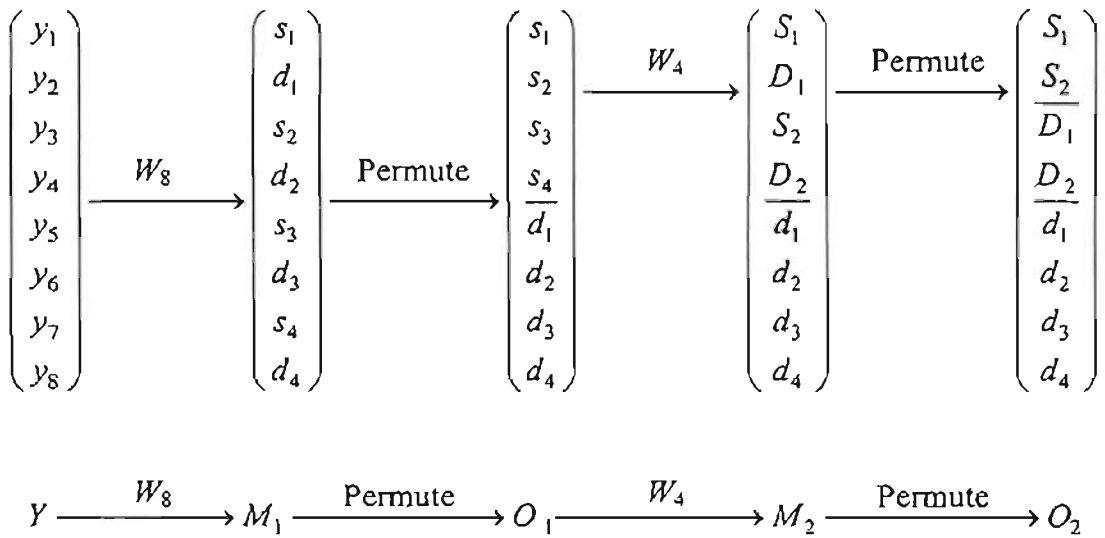
Figure 42: Demonstration of the pyramidal algorithm to obtain the *DWT* of a vector of length 8.

If the number of coefficients of the wavelet basis exceeds the length of W_N, then the coefficients of the basis are combined to form a new set. This is usually encountered at the higher levels of the hierarchy, for example using D_6 to produce W_4.

The process carried out in **Figure 42** can be reversed to recover the original data vector by carrying out the *inverse DWT* using the inverse of W_N. The inverse of W_N is simply its transpose (mentioned earlier in §6.3.1).

6.3.3. Application of the *DWT* to Data Reduction

The power of the *DWT* lies in its ability to transform the input data to a space where the data is represented *sparsely*, that is, the transform space consists mostly of zero (or near-zero) coefficients. Hence, the original data can be satisfactorily approximated by truncating the small (near-zero) wavelet coefficients and then returning to the original space via the inverse *DWT*. The *DWT* was applied in [26] to reduce *NIR* [19]-spectral data for predicting glucose concentrations of aqueous solutions.

To demonstrate data reduction using the *DWT*, a cusp (**Figure 43(a)** [20]) and a Gaussian (**Figure 44(a)**) were each sampled on a vector of length $2^{10} = 2048$. The *DWT* using D_6 was applied to each of the two functions; this was implemented in *IDL*. The wavelet coefficients are also plotted in **Figure 43(a)** and **Figure 44(a)**. Due to the data vector being split into two after each permutation, various levels of hierarchy will appear within the channel ranges[21]: 1024 to 2047, 512 to 1023, 256 to 511, and so on. For a data vector of length 2^N, there will be N such levels.

Figure 43(b) and **Figure 44(b)** are plots of the absolute values of the wavelet coefficients, sorted in decreasing order of magnitude. For the *DWT* of the cusp, 294 out of 2048 coefficients were larger than 10^{-4} while only 95 coefficients were larger than 10^{-4} for the Gaussian. Therefore, the cusp can be represented quite adequately by only 294 coefficients instead of 2048, with the remaining coefficients set to zero.

In general, however, the data reduction has to take into account the positions of the major components as well. Thus, for the cusp, 2 × 294-numbers have to be stored to approximate the function accurately.

---

[19] Near-infrared

[20] Based on an example given in [25].

[21] The *x*-values range from 0 to 2047.
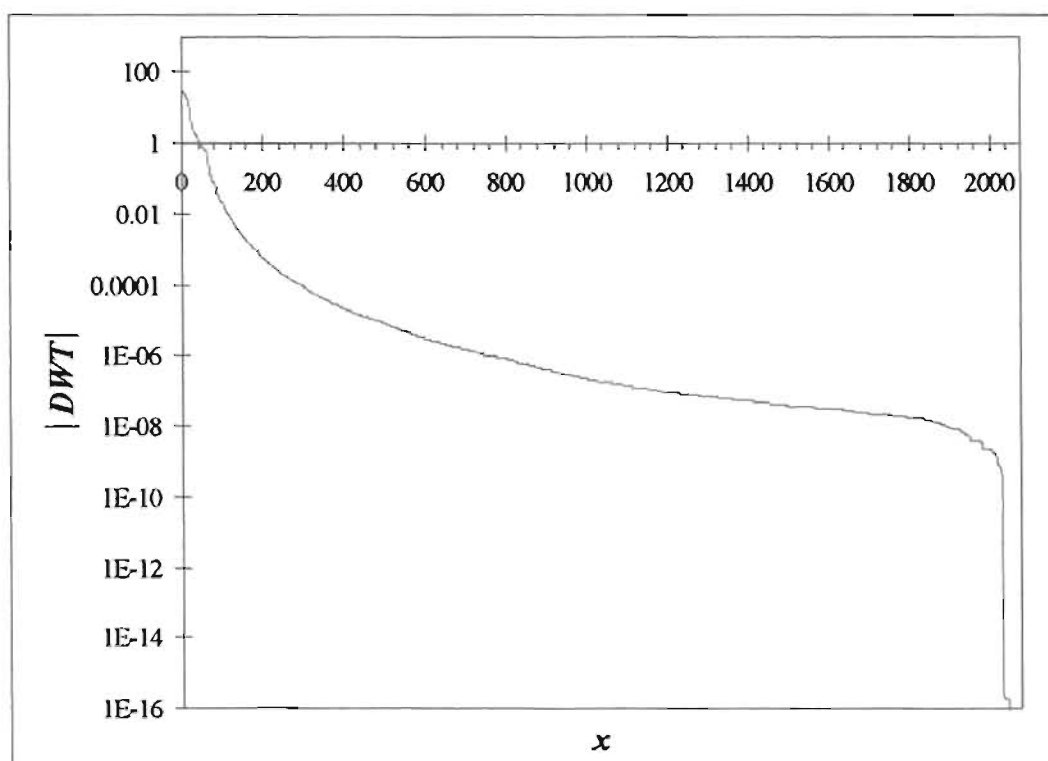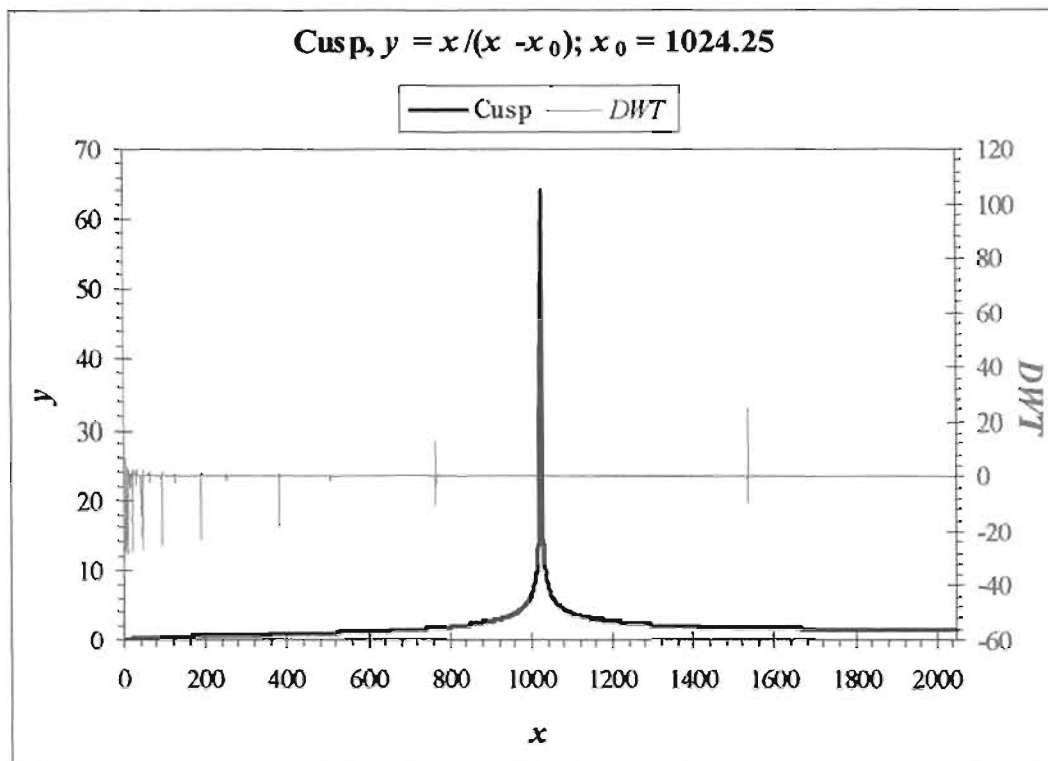
Figure 43: *(a)* A cusp, and its *DWT*. *(b)* |*DWT*| in descending order of magnitude.

Gaussian, $y = \exp\{-0.5 \times [(x - x_0)/w]^2\}$; $x_0 = 1024$; $w = 20$
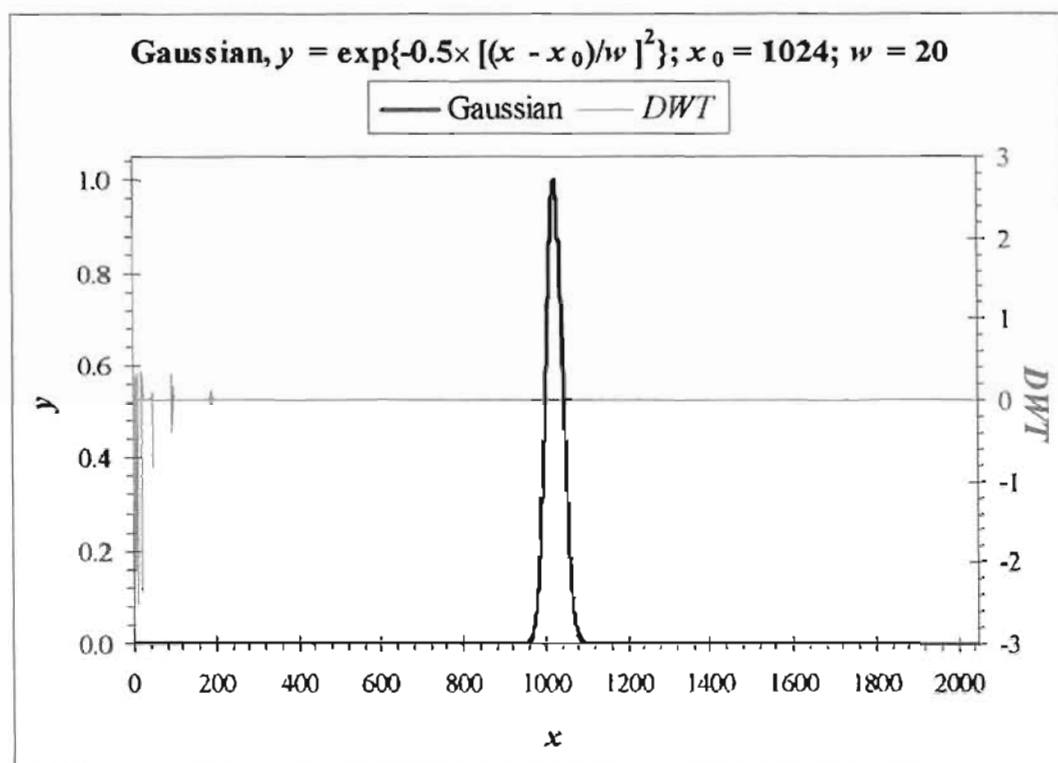
(a)
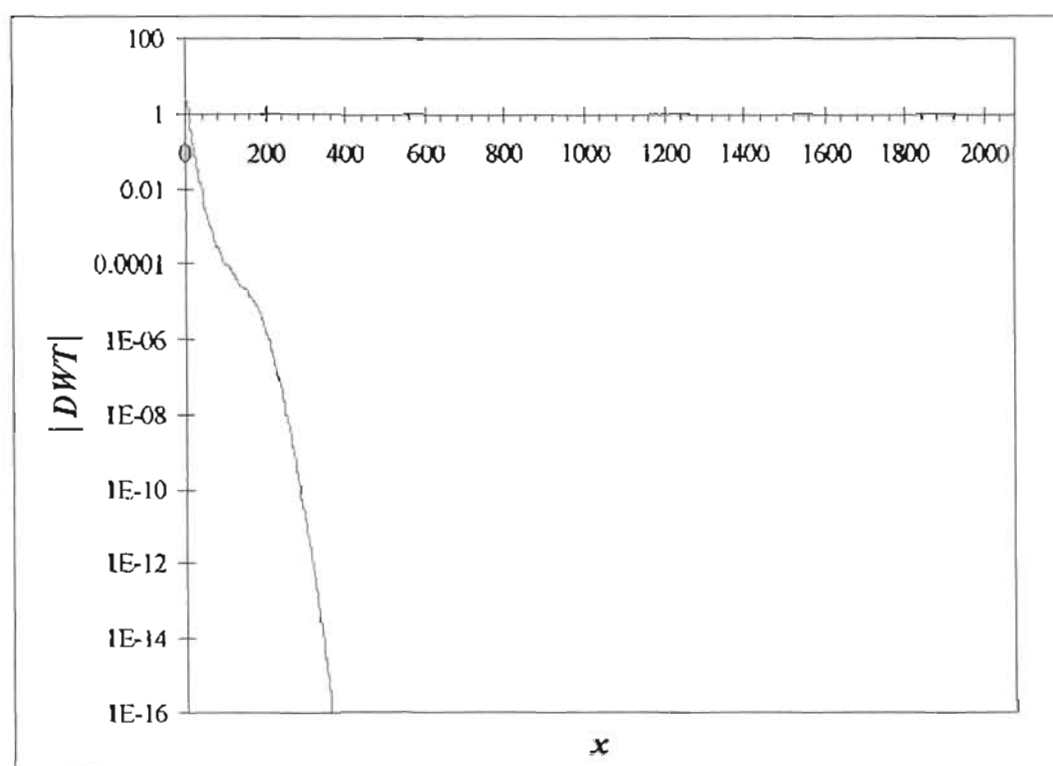
(b)

Figure 44: (a) A Gaussian, and its DWT. (b) $|DWT|$ in descending order of magnitude.

To demonstrate the power of the *DWT* for the reduction of spectral data, **Figure 45** and **Figure 46** compare *DuET*-spectra, consisting of 2048 channels of data, that were reconstructed using 36 and 68 wavelet coefficients, respectively.
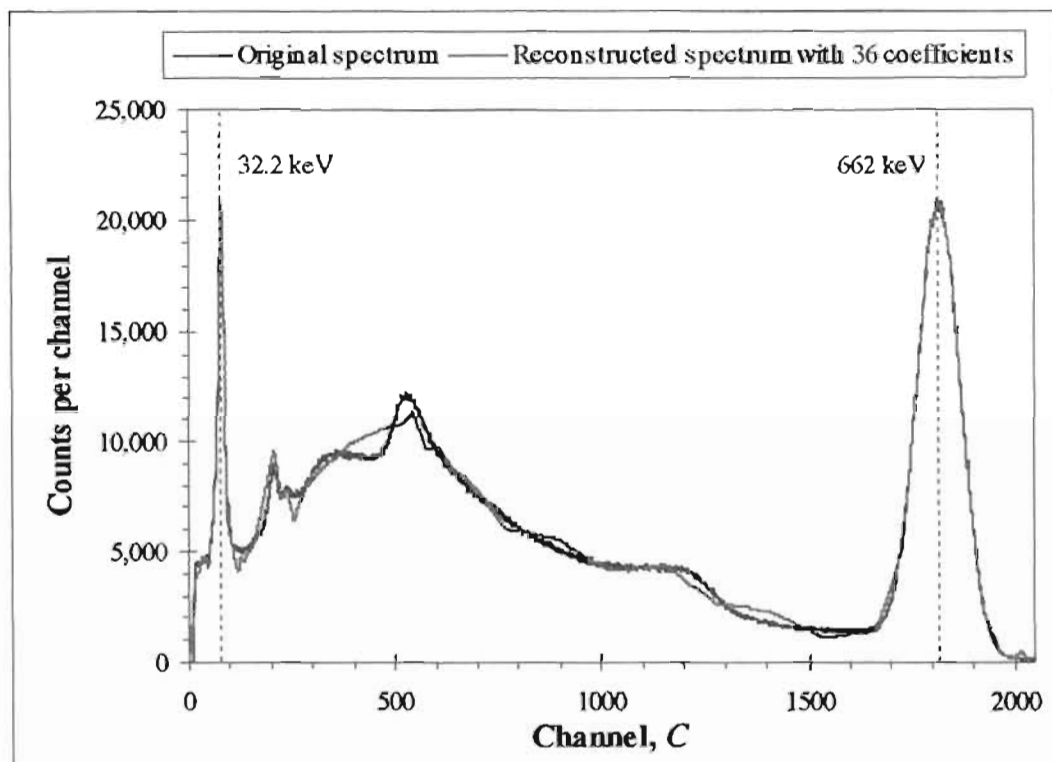
Figure 45: Original and reconstructed spectra. The reconstruction used 36 major wavelet coefficients.
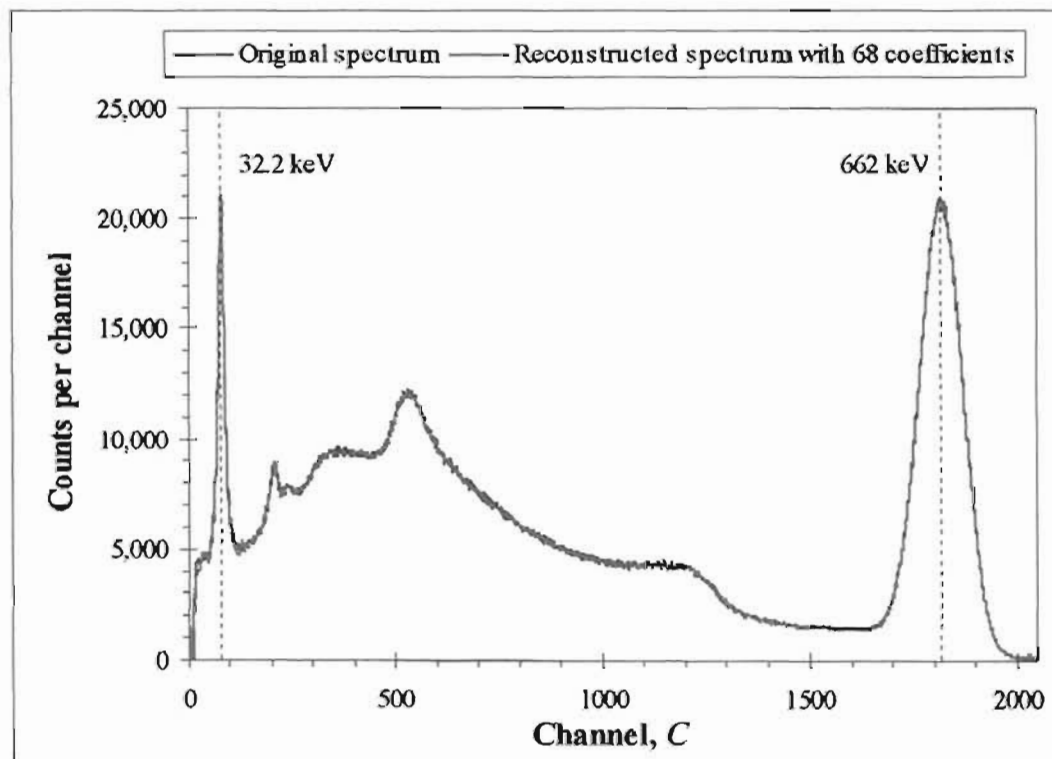
Figure 46: Original and reconstructed spectra. The reconstruction used 68 major wavelet coefficients.

It is clear that the spectrum reconstructed with 68 wavelet coefficients (**Figure 46**) matches the original data better than the reconstruction using 36 coefficients (**Figure 45**). However, the reconstruction with 36 coefficients adequately matches the original spectrum at 32.2 keV and 662 keV, which represent the regions of interest for *DuET* in this work.

6.4. Methodology

The *DWT* was first applied to each *DuET*-spectrum to reduce the number of input variables to the neural network. The major wavelet coefficients (those having the greatest amplitude in each level of the hierarchy, §6.3.3) were then extracted, and fed into a trained neural network to predict the relative concentration of the required component. The positions of the wavelet coefficients were not included. This method is expressed diagrammatically in **Figure 47**.

Input spectrum

Apply the *DWT* to spectrum

Extract major wavelet coefficients

Artificial Neural Network (*ANN*)

Concentration of required component
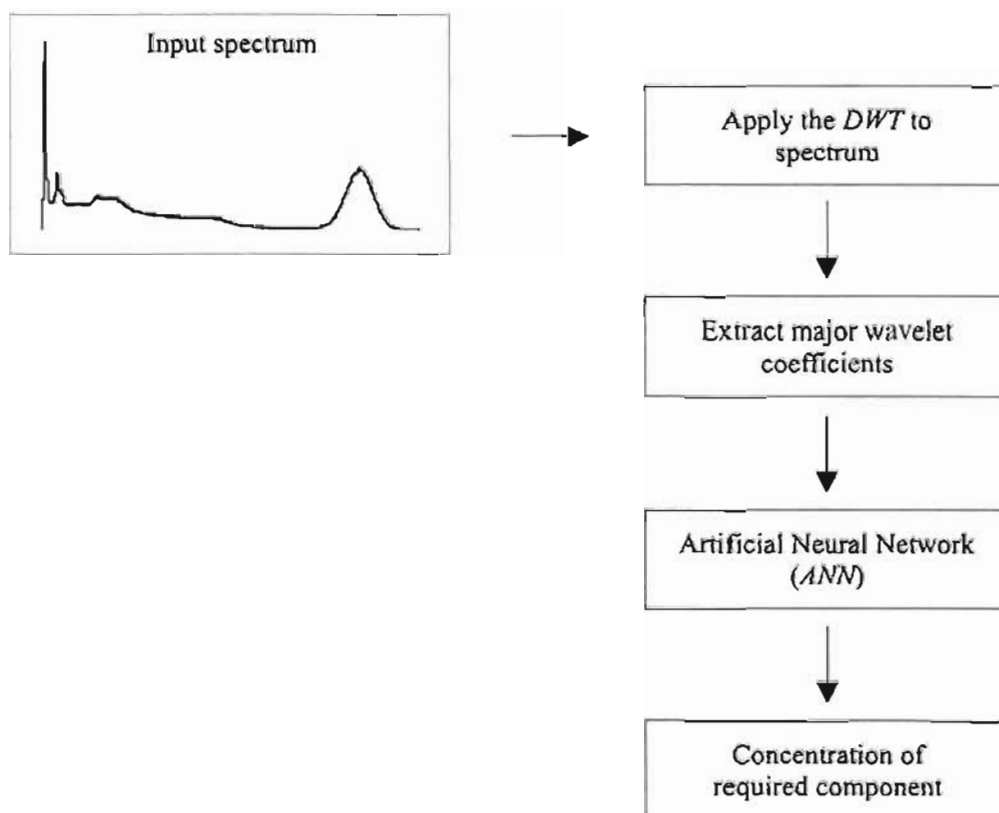
Figure 47: Analysis of *DuET*-spectra using the *DWT-ANN* approach.

6.5. Determining Concentration of Ferric Chloride via the *DWT-ANN*

The *DuET*-spectra of ferric chloride (described in §5.3) were used for this investigation: a total of 280 spectra (40 spectra per sample) were available.

The first step involved dividing the spectra equally into a training set and a testing set. A cross-validation set, using 5 spectra per sample from the training set, was also created to prevent overtraining of the *ANN*.

An *IDL*-program (see **Appendix D** for source code) was written to read the spectra, apply the *DWT* and produce the major wavelet coefficients. The 2048 channels of data for each spectrum were reduced to 36 wavelet coefficients.

An *MLP* was designed in *NeuroSolutions*, the neural network simulator. The *ANN* was trained with the 140 training spectra. Once a low value for the *MSE* had been achieved, the reliability of the *ANN* was assessed by feeding it the testing set to predict the concentration of ferric chloride.

The results of the testing are shown in **Figure 48**; the correlation between actual and predicted values is excellent ($\Re^2 = 0.9985$). The linear fit has a slope of 0.9844 and the intercept is 0.0560. Ideally, the slope and intercept would be unity and zero, respectively. Therefore, the *ANN* performed well on the unseen (test) data.

A comparison of the relative error of [$FeCl_3$] predicted with the *ANN* and that determined via regression is shown in **Figure 49**. The results for the neural network compare quite well to that obtained via regression, which did yield better results.

Therefore, it can be concluded that the problem of estimating the concentration of $FeCl_3$ from a given *DuET*-spectrum can be adequately performed by the *DWT-ANN*.
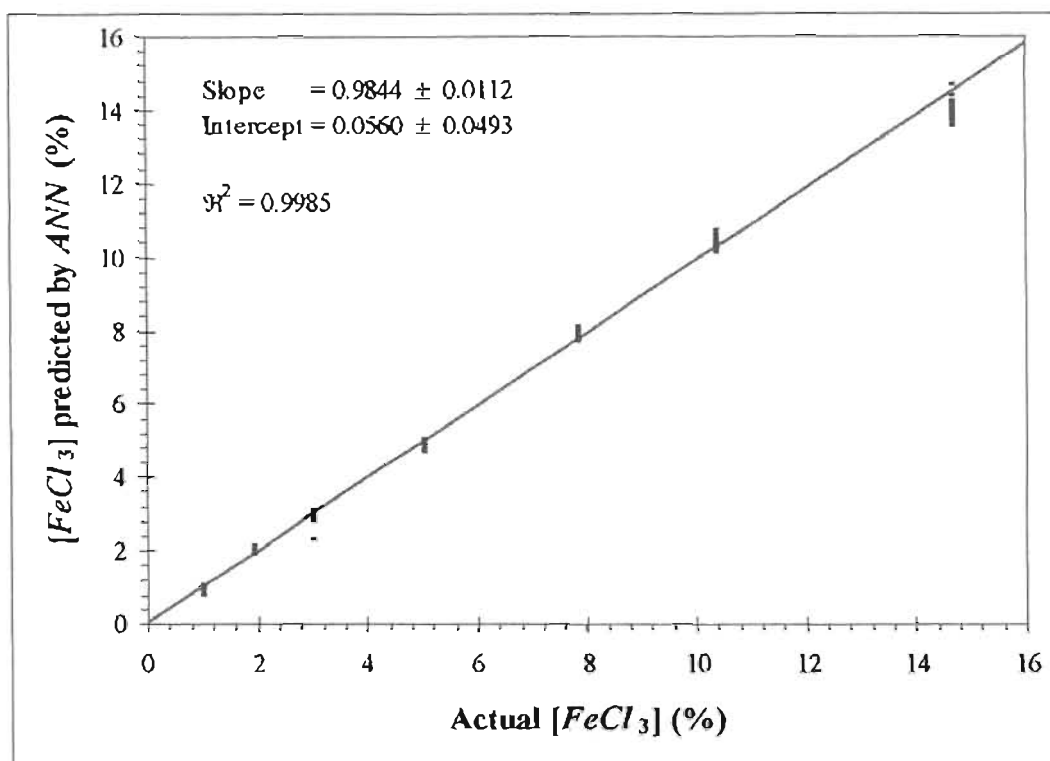
Figure 48: Comparison of concentration of $FeCl_3$ predicted by an *ANN* with the actual concentration. The line (—) represents a linear fit to the data. The slope = 0.9844 and the intercept = 0.0560. Ideally, the $\Re^2$ and the slope would be unity, and the intercept would be zero.
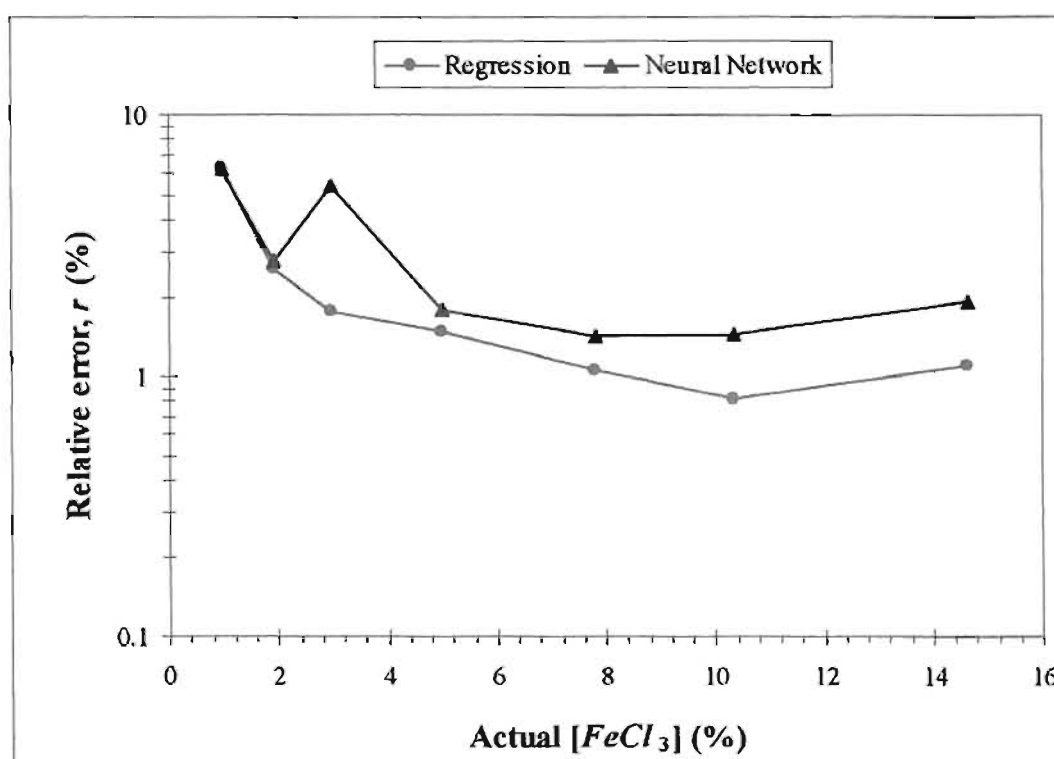
Figure 49: Comparison of relative error of $[FeCl_3]$ predicted by an *ANN* with that determined via regression. The value of r spikes at 2.98 % due to the outlier seen in **Figure 48**.

6.6. Determining Concentration of Soil in Cane via the *DWT-ANN*

The *DuET*-spectra for the soil/cane-samples (§5.4.2) were used for this investigation. There were 13 soil in cane-samples, and 100 spectra were recorded per sample.

Firstly, the data was split into three sets for training (40 spectra per sample), cross-validation (10 spectra per sample) and testing (50 spectra per sample).

The *IDL*-program, that was used for the ferric chloride spectra in §6.5, was executed to read the *DuET*-spectra, apply the *DWT* and produce 36 major wavelet coefficients.

The same *MLP*, that was used in §6.5, was implemented with the exception that it was trained with the soil in cane-data. After a low value for the *MSE* was obtained, the *ANN* was tested.

The results are shown in **Figure 50**; the correlation between actual and predicted values is excellent ($\Re^2 = 0.9860$). The linear fit has a slope of 0.9866 and the intercept is 0.4320; ideally, the slope and intercept would be unity and zero, respectively. Therefore, the *ANN* had performed well on the test data.

Comparing **Figure 50** and **Figure 34**, for the predicted soil concentrations using *ANN*s and regression, respectively, it can be seen that the spread of values is similar. This suggests that both techniques could be influenced by a common experimental variability.

A comparison of the relative error of the soil concentration predicted by the *ANN* with that determined via regression is shown in **Figure 51**. The results for the neural network compare quite well to that obtained via regression. The regression technique, with lower relative errors over most of the range, appears to perform slightly better than the *DWT-ANN* approach. However, if the *DWT-ANN* is implemented in hardware, the speed of processing is advantageous.
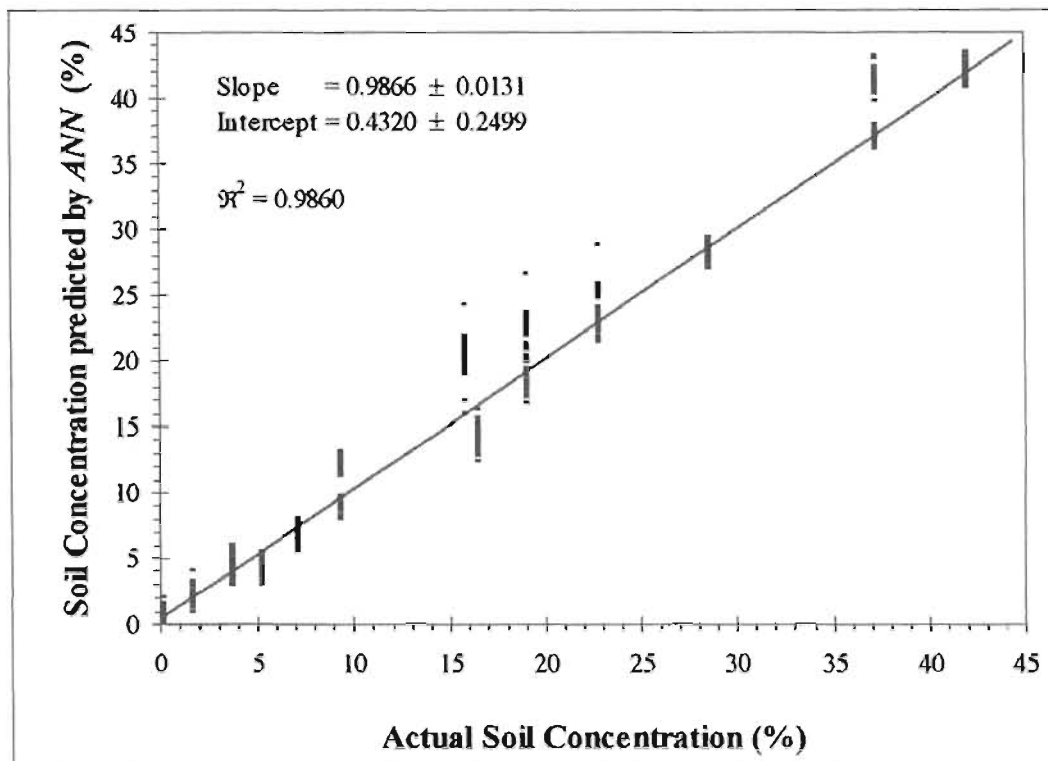
Figure 50: Comparison of soil concentration predicted by an *ANN* with the actual concentration. The line (—) represents a linear fit to the data. The slope = 0.9866 and the intercept = 0.4320. Ideally, the $\Re^2$ and the slope would be unity, and the intercept would be zero.
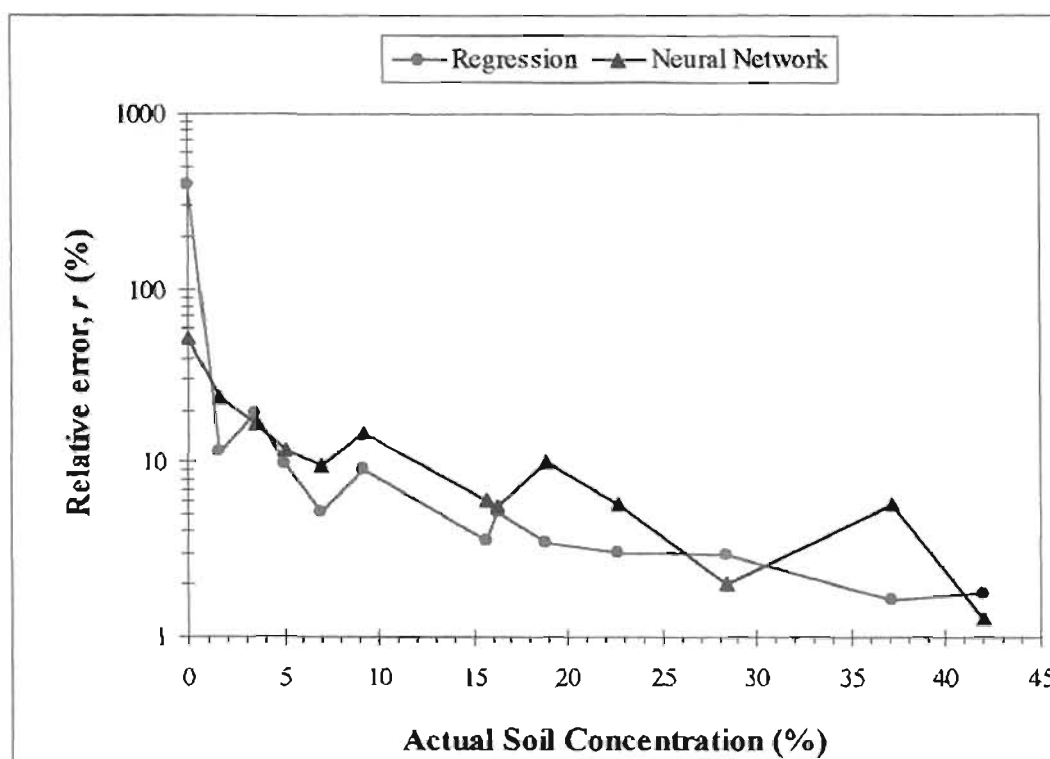
Figure 51: Comparison of relative error of the soil concentration predicted by an *ANN* with that determined via regression. Regression performed slightly better than the *DWT-ANN*.

6.7. Summary

It was shown that the *DWT* coupled with an *ANN* is a powerful tool for the analysis of *DuET*-spectra. The *DWT-ANN* was capable of predicting concentrations of ferric chloride in aqueous solutions and the amount of soil in cane from *DuET*-spectra. Good correlation was obtained between predicted and actual concentrations for both sample sets. Upon comparison with the regression technique, the neural network approach performs similarly but with slightly larger relative errors.

The *DWT-ANN* methodology can be generalised to other types of spectra. Specific information can be obtained directly without executing tedious, intermediate steps.

Finally, it must be stated that no attempt was made to optimise the number of wavelet coefficients or study other neural network topologies: a foundation for future work is thus provided. In so doing, the *DWT-ANN* approach could be improved.

7. X-ray Imaging

7.1. Introduction

X-ray imaging was briefly introduced in §1.5. This chapter describes a preliminary investigation into applying X-ray imaging to the soil in cane-problem. The work that was carried out was not intended to be extensive; rather it can it described as a "proof-of-principle" initiative. A more comprehensive work would involve a large variety of samples, X-ray parameters and image analysis techniques.

7.2. Overview of X-ray Production and Spectra
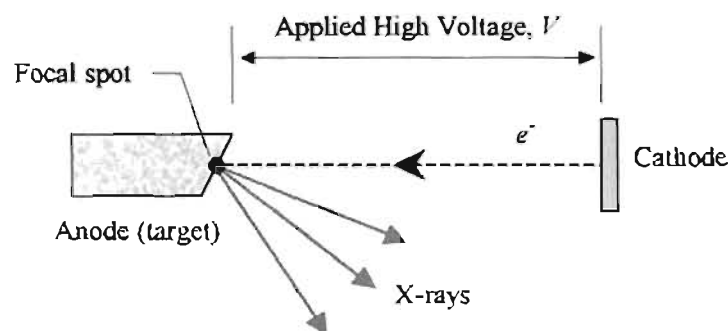
Figure 52: Principle of X-ray production.

The principle of X-ray production is illustrated in **Figure 52**. A high voltage is applied across the X-ray tube between the cathode and anode (or *target*). Electrons are emitted from the cathode via thermionic emission, and are accelerated across the potential to the focal spot of the anode.

The incident electrons strike the target, and X-rays are generated by two distinct processes. The first process involves an interaction between an incident electron and a target nucleus. The positive nucleus attracts the electron, which is then deflected from its original path. The electron may lose energy and be slowed down when its direction changes. The kinetic energy lost by the electron is emitted in the form of radiation, known as *bremsstrahlung* ("braking radiation" in German). Bremsstrahlung forms a

continuum ranging from 0 keV to the maximum energy attained by the incident electrons before striking the target.[27]

The second process of X-ray generation is due to a collision between an incident electron and electrons in the inner shells of the target atoms. The atomic electron is expelled, and a vacancy is created. The target atom has become a positive ion and is unstable. Electrons from higher shells fill the vacancy, and emit *characteristic X-rays* in the process (as previously described for *EDS* in §4.1). The characteristic X-rays constitute a *discrete* (or *line*) spectrum.[27]

Filters are usually inserted in the path of the X-rays to absorb the lower energy X-rays. This is necessary, especially for medical diagnosis, where the purpose is to reduce the dose of X-rays to the patient.[28]

A semi-empirical X-ray spectrum[28] is shown in **Figure 53**. The major characteristic X-ray lines (at 59, 67 and 69 keV) for the tungsten (*W*)-target can be clearly seen superimposed upon the X-ray continuum due to bremsstrahlung.
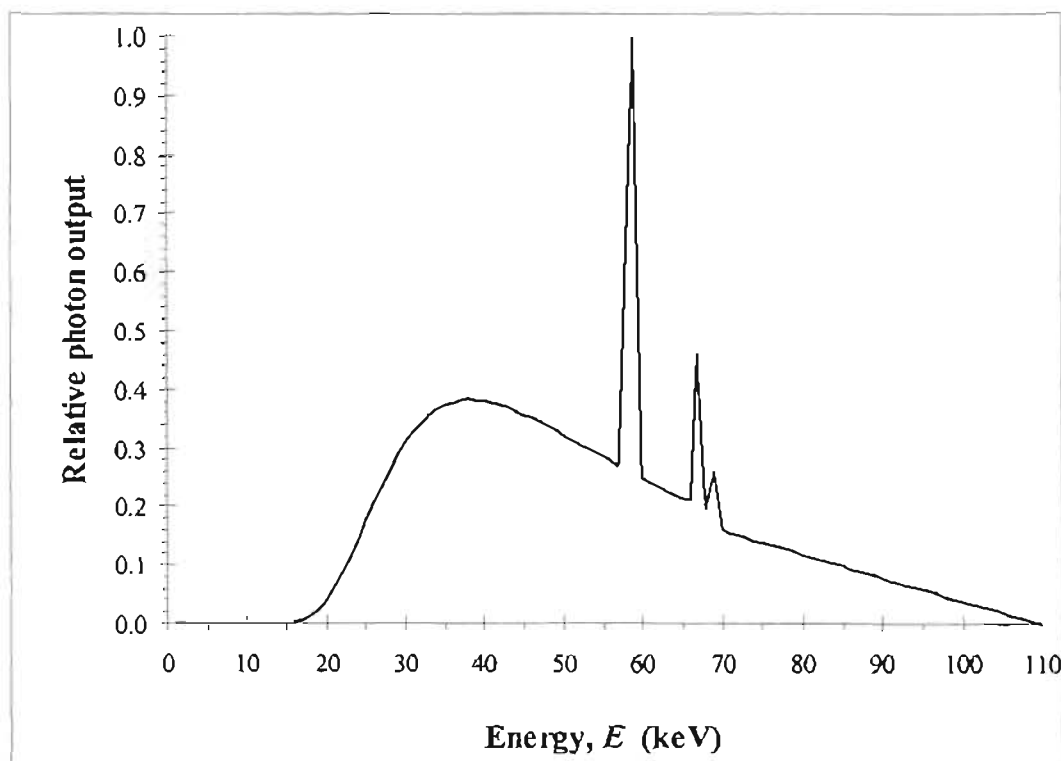
Figure 53: A semi-empirical X-ray spectrum typical of that used for standard radiography[28]. The accelerating voltage was 110 kV, the target was tungsten (*W*) and a 3.0 mm *Al*-filter was used. The peaks, at 59, 67 and 69 keV, correspond to characteristic X-ray emissions due to interactions of the incident electrons with the atoms of the tungsten target.

Mammography, a derivative of conventional X-ray radiography, is used for the identification of tumours in human breast tissue. The maximum X-ray energies are quite low (20 – 40 keV) in comparison to the energies used for chest X-ray imaging (100 – 140 keV).

For mammography units, the target material of the X-ray tube and filters are usually made of molybdenum (*Mo*). This ensures that the emission spectrum consists mainly of the strong characteristic lines of *Mo* (17 and 19 keV). **Figure 54** shows a semi-empirical X-ray spectrum typical of that used for mammography.
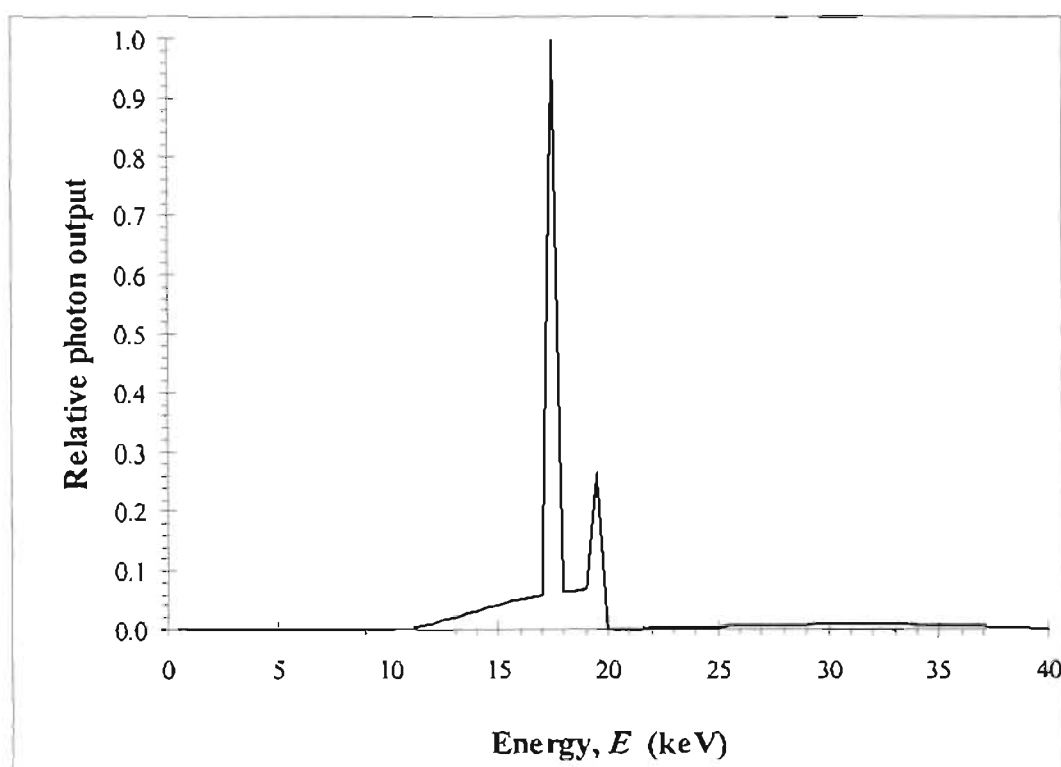
Figure 54: A semi-empirical X-ray spectrum typical of that used for mammography[28]. Mammography utilises low-energy X-rays so as to improve contrast between cancerous regions and healthy breast tissue. For the above spectrum, the accelerating voltage was 40 kV, and a *Mo*-target with 1.0 mm *Be*- & 0.06 mm *Mo*-filters were used. The characteristic X-ray lines of *Mo* (at 17 and 19 keV) can be clearly identified.

Commercial mammography units possess a higher resolution than their high-energy counterparts used for chest radiography in order to allow radiographers to identify the small, characteristic features of breast cancer.

7.3. Apparatus

The X-ray measurements were carried out at Addington Hospital (Durban) using a commercial mammography unit. **Table 10** summarises the description and settings of the apparatus. The geometry of the experiment is shown in **Figure 55**.

Table 10: Description and settings of the apparatus used for X-ray imaging of soil in cane.[22]

Mammography unit	*Philips MammoDiagnostUC*
High Voltage (kV)	23
Exposure (mAs)	80
Focal spot size of electron beam (mm)	0.3
Target	*Mo*
Filter	*Mo*
Film-type	*Kodak MinR 2000* with green-emitting screen
Source-film distance (cm)	~90
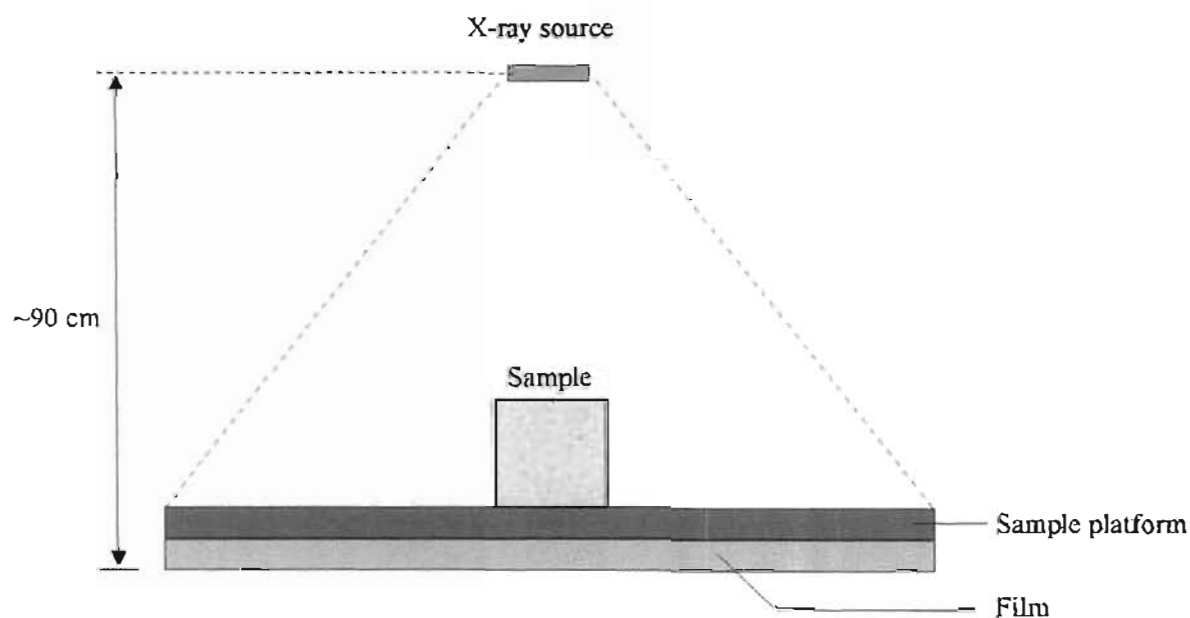
Figure 55: Side view of the experimental layout for the X-ray imaging of soil in cane-samples.

---

[22] Private communication: Dr. William Rae. Addington Hospital, RaeW@dohho.kzntl.gov.za

7.4. Methodology

The interactions and concepts described in §2.1 also apply to X-rays.

Due to the differences in attenuation coefficients between soil and sugar cane (as seen in **Figure 21**), it was anticipated that exposing the samples to low-energy X-rays will result in images with a large amount of contrast between soil and cane. In other words, the soil should appear as white (underexposed) regions on the radiograph.

Image analysis of a digitised version of the radiograph will involve integrating the intensities of image pixels – this integrated pixel value would then be related to the soil concentration (larger integrated values should indicate larger soil concentrations, and vice-versa).

The investigation involved measurements on two separate occasions: *Phase I* was a preliminary exercise to determine if mammography was capable of distinguishing soil from the cane. Based on the results of the preceding phase, *Phase II* was then undertaken with a larger set of samples.

7.5. *Phase I*: Initial Investigation

7.5.1. Experimental Method

Six soil/cane-samples were chosen for this study: the soil concentrations were 0, 1.5, 3.5, 9.2, 18.9 and 37.2 %. The *polytops*, containing the samples, were placed on the sample platform in a 2 × 3-array (**Figure 55**), and imaged simultaneously since the film area was quite large (approximately *A4*-size[23]). The first radiograph was labelled *Radiograph #1*. A second radiograph, *Radiograph #2*, was recorded after the samples were shaken and rearranged on the sample platform.

---

[23] The *A4*-standard has dimensions 297 mm × 210 mm.

The radiographs were digitised on an *Epson GT-12000* scanner with a built-in transparency adapter, and the resulting images were stored as 600 dpi[24], 256 level, gray-scale bitmaps.

7.5.2. Analysis

A digitised version of *Radiograph #2* is shown in **Figure 56**. The soil particles (whitish regions) can be clearly distinguished from the sugar cane (dark regions). The soil concentration of each sample is indicated alongside each sub-image.

The procedure, that was used for the analysis of the digitised radiographs, is described below.

1. Each of the sub-images, representing each sample, was extracted from the radiographs, and saved as 256 level, gray-scale bitmaps. See **Figure 57***(a)*.

2. A circular region-of-interest (*ROI*) was defined for each image. The *ROI* was the area to be used for subsequent image analysis, and was chosen to be as large as possible (but avoiding the regions corresponding to edges of the *polytops*).

3. Pixels outside the *ROI* were set to a value of 255 (corresponding to a colour of white). See **Figure 57***(b)*.

4. If necessary, an image filter was applied to the image to enhance the contrast between soil and cane.

5. The intensities of the pixels within the *ROI* were summed. The sum is termed the *integrated pixel intensity*, I_p.

The above procedure was implemented in *IDL*; the source code is listed under **Appendix E**.

---

[24] Dots per inch
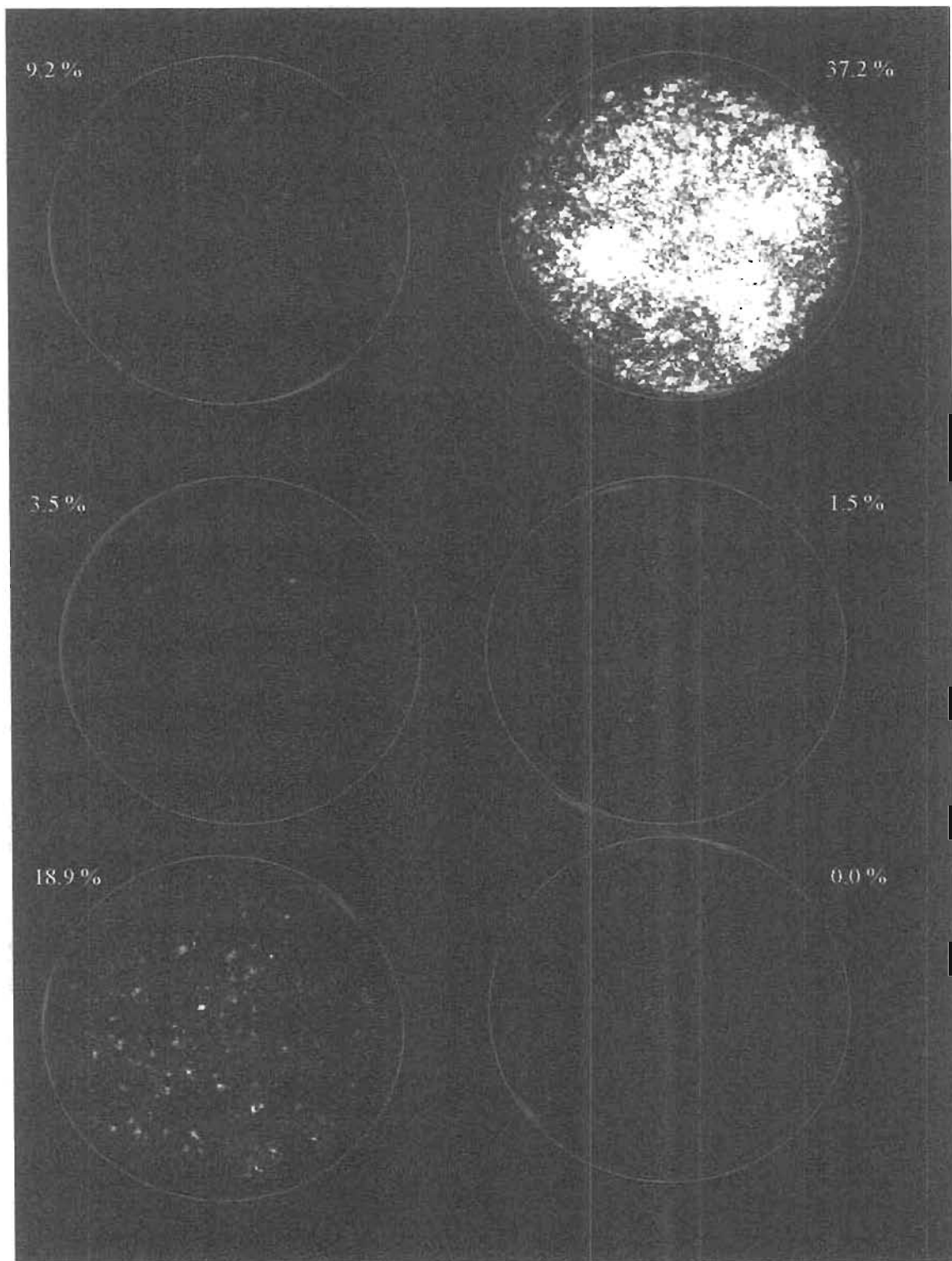
Figure 56: A digitised version of *Radiograph #2*. The soil concentration of each sample is indicated. The white overlays were superimposed upon the image to indicate the borders of the *polytop* sample containers. White regions within the overlays correspond to soil particles.

91
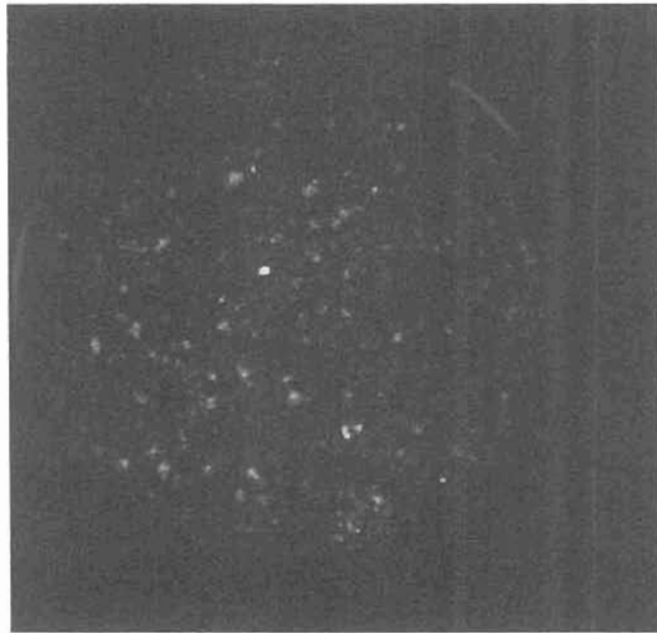
(a)
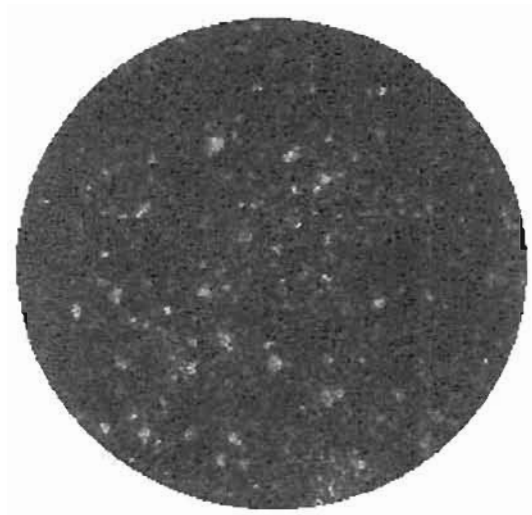
(b)

Figure 57: *(a)* Digitised gray-scale sub-image of a sample containing 18.9 % of soil. The soil particles appear as white regions while the cane show up as black regions. *(b)* False-colour image of *(a)*, created in *IDL* to enhance the subtle variations in the gray-scale intensity.

7.5.3. Results

Figure 58 shows the results of the analyses of *Radiographs #1* and *#2*.
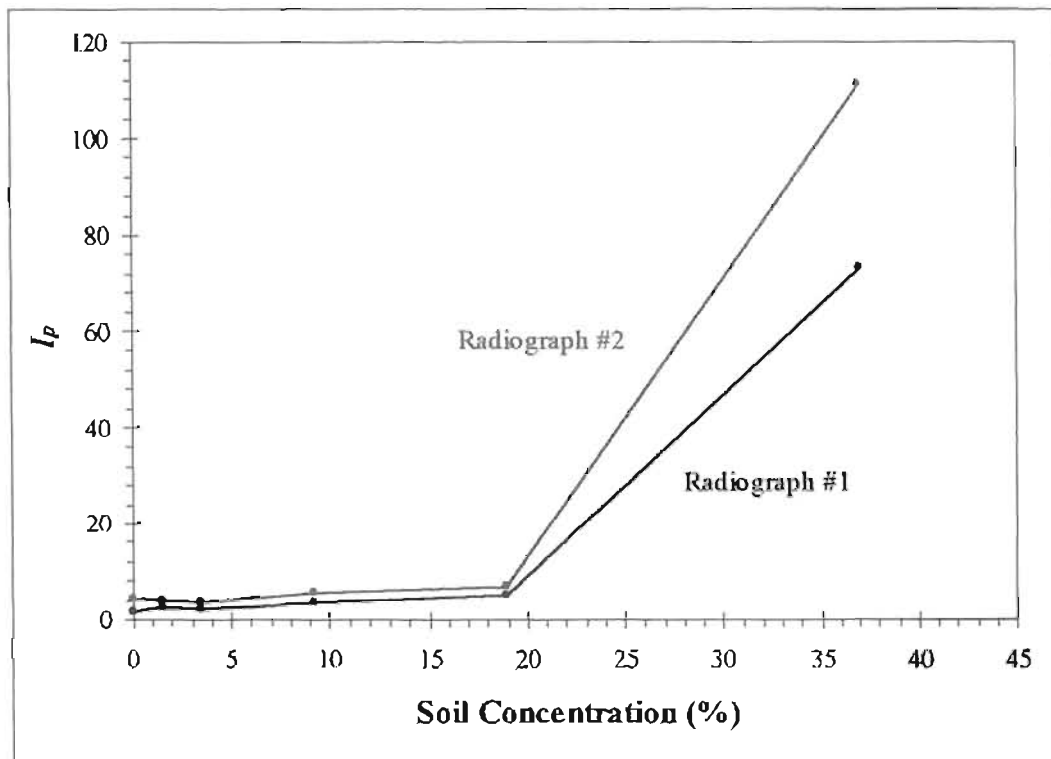
Figure 58: Plot of Integrated pixel intensity, I_p vs. soil concentration for *Radiographs #1* and *#2*, recorded in *Phase I*. No contrast enhancements were applied to the images. The I_p-values for *Radiograph #2* are greater than those for *Radiograph #1* – this could be due to differences in recorded X-ray intensities.

It can be clearly seen in **Figure 58** that higher I_p-values indicate higher soil concentrations, as expected. However, for low soil concentrations ($\lesssim 5$ %), I_p does not appear to change much.

After this initial work, it appeared that X-ray imaging was quite promising. Although it was unable to adequately quantify the low soil concentrations ($\lesssim 5$ %), the technique was demonstrated as one that can clearly distinguish the soil (white regions) from the cane (black regions).

The sample set that was used for *Phase I* was quite small, and the next logical step was to increase the range of soil concentrations (§7.6).

7.6. *Phase II*: Extended Investigation

7.6.1. Experimental Method

The 13 soil/cane-samples, that were used for *DuET*-measurements (§5.4.2), were imaged. Four radiographs were recorded with the apparatus and settings described under **Table 10**. Some samples were imaged more than once.

7.6.2. Analysis

The analysis of the digitised images followed the same procedure listed in §7.5.2.

7.6.3. Results

Figure 59 shows the results from analysis of the radiographs. Visually, the values of I_p increase with increasing soil concentrations. An exponential function, of the form $y = c_0 \cdot exp(c_1 \cdot x)$, was fitted to the data[25], where x and y represent soil concentration and I_p, respectively, and c_0 and c_1 are the fitting parameters.
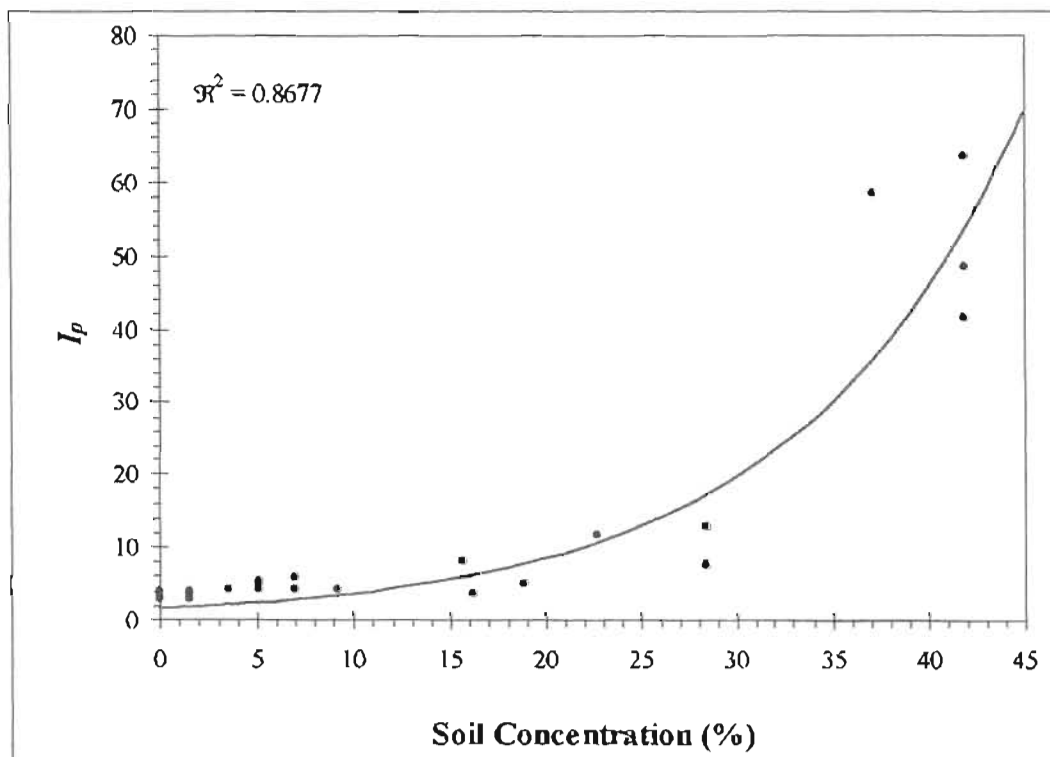
Figure 59: Plot of Integrated pixel intensity, I_p vs. soil concentration (*Phase II*). The line (—) represents an exponential fit to the data. $\Re^2 = 0.8677$, signifying a reasonable correlation.

---

[25] The fitting was performed in *IDL* using the `CurveFit`-routine.

The fitting parameters were:

$$c_0 = 1.5890, \qquad c_1 = 0.0841.$$

Returning to **Figure 59**, the larger soil concentrations appear to have different I_p-values for repeated measurements of the same sample (e.g. sample with 41.9 % soil). The reason for the variation of I_p-values needs to be understood.

A plot of I_p vs. soil mass is shown in **Figure 60**. An exponential function, of the form $y = c_0 \cdot exp\left(c_1 \cdot x\right)$, was fitted to the data. The fitting parameters were:

$$c_0 = 2.4252, \qquad c_1 = 0.4076.$$

The value of $\mathfrak{R}^2$ was 0.9498, indicating a better correlation than that obtained for I_p vs. soil concentration in **Figure 59**. This suggests that the mass of the soil can be directly measured using X-ray imaging. In general, it can be expected that varying soil-types (due to differences in density and elemental composition) will result in different relationships (that is, different values for the fitting parameters).
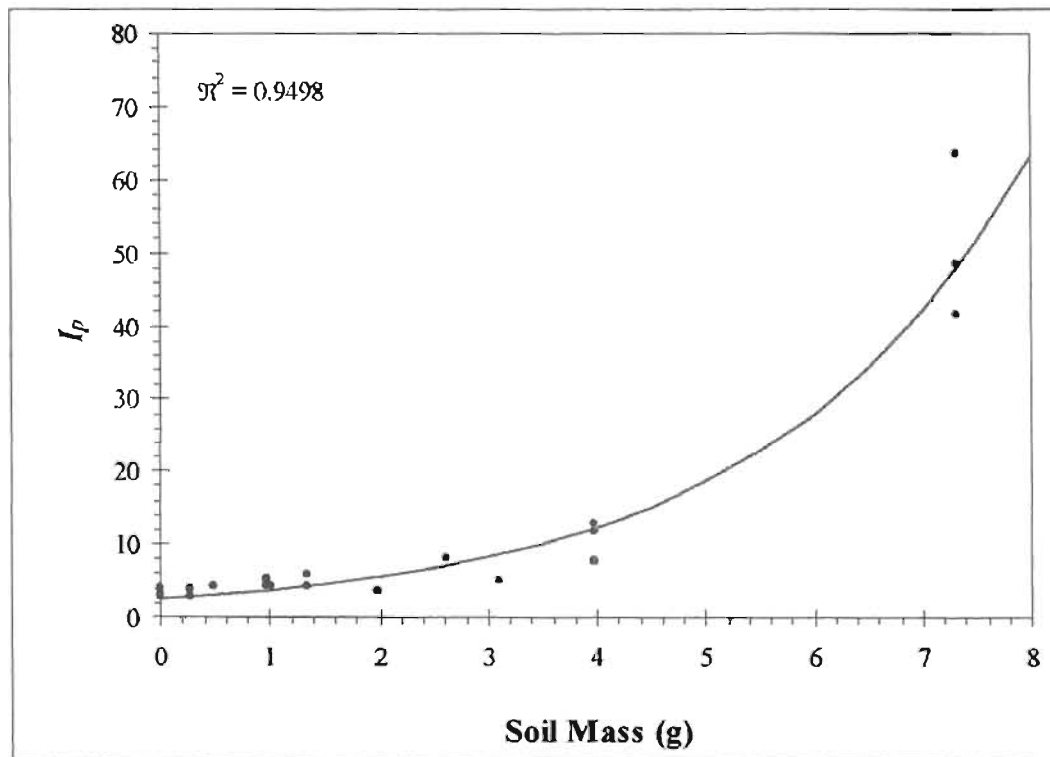
Figure 60: Plot of Integrated pixel intensity, I_p vs. soil mass (*Phase II*). The line (—) represents an exponential fit to the data. $\mathfrak{R}^2 = 0.9498$, signifying good correlation between the model and data.

It was naturally assumed that the X-rays had sufficiently penetrated the samples. However, insufficient exposure results in *saturation*, where the pixel values equal the maximum allowed value of 255. Then the integrated pixel intensity is larger and non-representative of the soil concentration. Increasing the X-ray exposure is expected to reduce the amount of saturated pixels. Future work could involve investigating the effect of exposure on variables like sample thickness and soil concentration.

The possible non-uniformity of the X-ray beam intensity across the film area must also be considered. This effect was briefly investigated by separating the images according to position of the corresponding sample on the platform (either top or bottom). **Figure 61** is a sketch of the top view of a typical sample layout (as seen by the X-rays): the *bottom layer* consists of samples 1 to 3, and the *top layer* consists of samples 4 to 6.
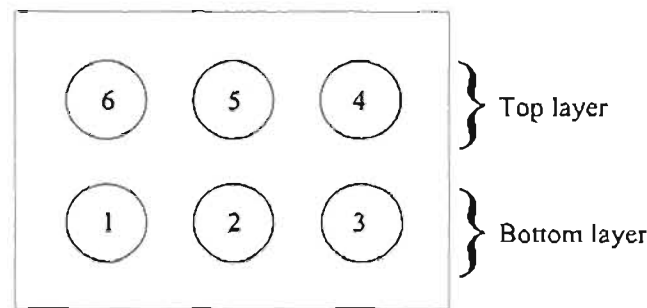
Figure 61: Sketch showing top view of samples on platform. With reference to the diagram, the *bottom layer* consists of samples 1 through 3 and the *top layer* consists of samples 4 through 6.

Figure 62 shows a plot of I_p vs. soil concentration after the sub-images for the samples were separated according to their positions on the sample platform. For most of the samples, those located in the top layer had higher I_p-values than those placed in the bottom layer. Thus, the X-ray beam could have been less intense over the top layer than the bottom layer since possible saturation could have resulted in higher I_p-values.
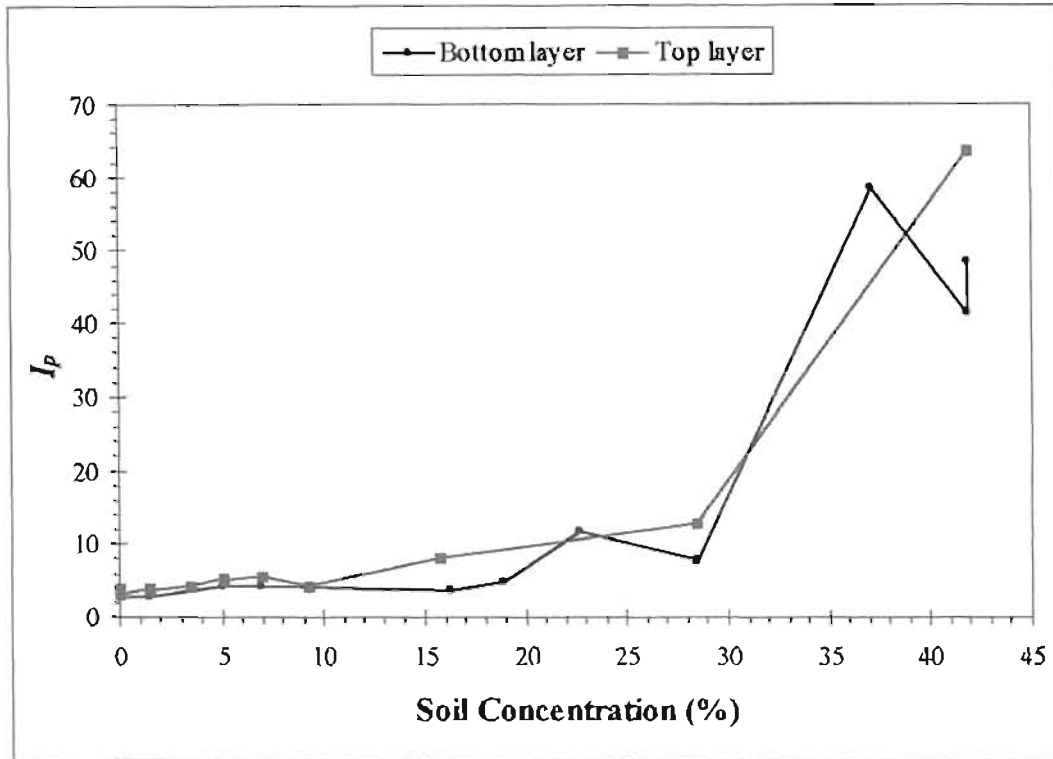
Figure 62: Variation of I_p with soil concentration. The images were grouped according to sample position, either belonging to the top or bottom layer (**Figure 61**). Samples placed on the top layer appear to have higher I_p-values than those samples placed on the bottom layer. This could indicate that the X-ray intensity was less intense over the top layer.

7.7. Summary

X-ray imaging was investigated as a technique to quantify soil in cane. Recorded radiographs showed a high contrast between the soil particles (white regions) and the sugar cane (dark regions). Significant contrast between soil particles and sugar cane is more visible for 18.9 %, 37.2 % and 41.9 % soil concentrations. However, there is hardly any systematic change of the white regions for the 1.5 %, 3.5 % and 9.2 % soil concentrations.

Attempts at relating the integrated pixel intensity, I_p, to actual soil concentrations were partially successful: a trend was observed but sensitivity to low concentrations needs to be investigated and improved

A plot of I_p vs. soil mass was produced. An exponential function was fitted to the data; the $\mathfrak{R}^2$-value was 0.9498. This good correlation suggests the possibility of using X-ray imaging to determine the mass of soil within a sample.

The reason for large differences in I_p-values (in *Phase II*) for the same sample needs to be understood. One reason is that pixel saturation, due to the X-rays not sufficiently penetrating the samples, increases I_p resulting in non-representative soil concentrations. Another possibility is that the X-ray beam intensity could not have been uniform over the area of the sample platform. Consequently, I_p-values appear to be dependent upon sample position.

X-ray imaging shows much promise, and future work could involve a study of various X-ray settings (filters, energy, exposure) with more soil-types and cane varieties.

The industrial use of X-rays is widespread (see §1.5), and therefore supports the possibility of developing an X-ray system for quantifying soil in cane. This technique is well suited to an on-line implementation, and is expected to satisfy all the requirements of a soil monitor, listed in §1.2.7.

8. Ashing

8.1. Introduction

The *DuET* and X-ray techniques have been investigated with the objective of measuring the amount of soil in the cane that is delivered to the sugar mills. In order to better evaluate these two techniques, it is necessary to understand the ashing technique which is currently used in the mills. For this purpose, the soil/cane-samples, that were used for *DuET* and X-ray imaging, were submitted to *SMRI* for ashing analysis.

The ashing technique essentially involves an incineration of the sample, and an analysis provides an estimate of the soil content in the original sample.

8.2. Ashing of Soil in Cane-samples

The thirteen soil in cane-samples (described in §3.3) were ashed following the procedure listed under **Appendix A**, with the exception that the moisture content of the original samples were not taken into account.

The ratio of the mass of the ash to the initial mass of the sample is termed the *total ash*. A plot of total ash concentration vs. actual soil concentration is shown in **Figure 63** for the 13 soil/cane-samples. The ash concentration correlates very well with the soil concentration ($\mathfrak{R}^2 = 0.9992$). Hence, the high regard that the sugar industry holds for the ashing method.

Ashing, however, takes a long time and its accuracy is dependent upon many factors (§1.2.6). Due to the requirement of small sample sizes (~50 g), the technique is inherently prone to the sampling issues that were mentioned in §1.3.4. It must be emphasised that the entire cane consignment needs to be adequately sampled to obtain an accurate estimate of the delivered soil mass.
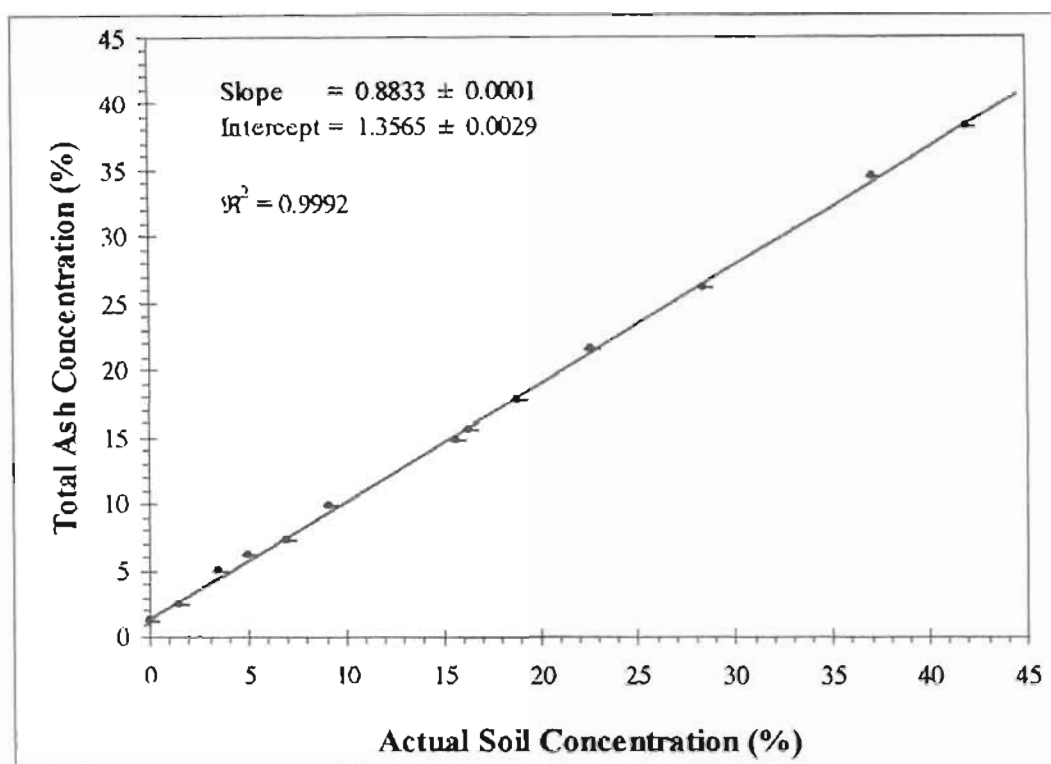
Figure 63: Results of ashing of the soil in cane-samples used for *DuET* and X-ray imaging. The ash concentration correlates very well with the actual soil concentration ($\Re^2 = 0.9992$). It can be seen that the total ash concentration for clean cane (0 % soil) is non-zero (1.2 %), and only applicable to this cane sample and, in general, will vary for different cane varieties, growing regions and climates.

9. Discussion and Conclusion

9.1. General Summary

DuET and X-ray imaging were applied to the soil in cane-problem. These techniques were investigated as possible non-destructive alternatives to the current ashing method.

Ashing was shown to produce a good correlation between total ash content and actual soil concentration. Hence, the current attractiveness of the technique for estimating soil in cane. However, the technique requires small samples, long processing times and its accuracy is dependent upon many factors (including cane variety). A technique, not influenced by factors that affect ash content, will be ideal.

DuET was demonstrated as a technique capable of determining the relative concentrations of the components of a binary mixture. This was clearly shown with the use of homogeneous, aqueous ferric chloride-solutions. *DuET* was thereafter applied to the soil in cane-problem. Strong correlation, between the predicted soil concentration using *DuET* and the actual soil concentration, was obtained. Thus, *DuET* was responding to changes in soil concentration, as required.

However, there were large variations in the predicted soil concentrations using *DuET* such that there were overlapping across the samples. Together with contributions from scatter (due to the "broad beam"-geometry), it was suspected that the gamma beams were not probing the entire sample, and this was responsible for the large variation in predicted concentrations. A moveable sample platform was designed with the intention to reduce the large variations in predicted concentrations. However, a more comprehensive investigation is required to determine whether such an arrangement improves soil estimates.

A comparison between the results from ashing and *DuET* is given in **Figure 64** below. The soil concentration determined via *DuET* varies linearly with the total ash concentration since the $\Re^2$-value is 0.9791. Therefore, *DuET* performs as well as the

ashing method. However, *DuET* offers additional advantages over ashing since *DuET* is:

1. *Faster*: *DuET*-spectra were recorded for a time of ~35 minutes per spectrum (t_i = 1950 s). The analysis of a *DuET*-spectrum is of the order of seconds. The processing time can be reduced with stronger sources. Ashing, on the other hand, takes approximately 2½ hours per sample[29].

2. *Scalable*: In principle, the sampling volume analysed with *DuET* can be increased by using larger detectors, larger sample platforms and stronger sources. Ashing is restricted to 50 g-samples[29].

3. *Non-destructive*: Samples analysed with *DuET* are not affected in any way while ashing destroys the sample.
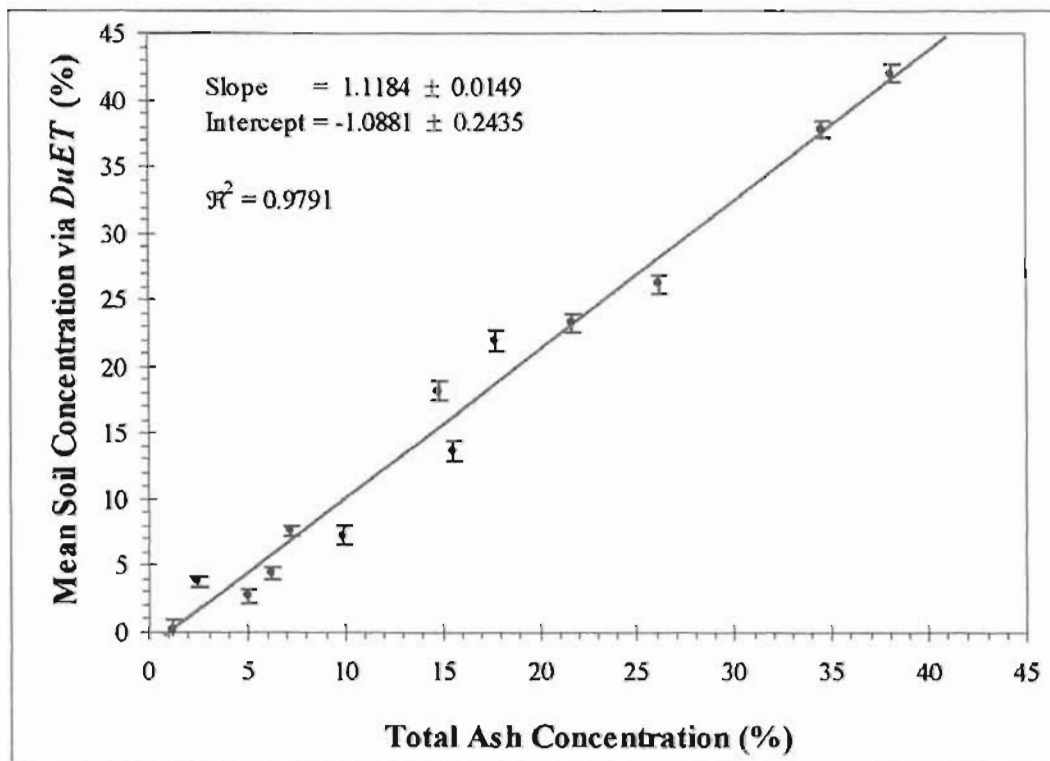
Figure 64: Comparison between *DuET* and ashing. The mean soil concentration via *DuET* was calculated for t_i = 1950 s (**Figure 34**). The line (—) represents a linear fit to the data.

From the literature survey that was carried out, it appeared that X-ray imaging had not previously been applied to the soil in cane-problem. Low-energy X-ray imaging was shown to be capable of distinguishing soil from cane. The recorded radiographs provided a visual confirmation of the presence of soil: the soil particles appeared as white regions superimposed upon black regions, which represented sugar cane. Digitised images of the radiographs were analysed using image processing techniques in order to relate the integrated pixel intensity, I_p, to the actual sample concentration. Reasonable correlation was attained between I_p and soil concentration ($\mathfrak{R}^2 = 0.8677$), and also between I_p and soil mass ($\mathfrak{R}^2 = 0.9498$).

X-ray imaging can be quite robust as it may be relatively independent of the cane variety or soil-type. The author believes that the long-term solution to the soil in cane-problem should embody some form of X-ray imaging, similar to *MobileSearch*, an existing commercial device that is used for similar large-scale measurements (**Figure 4** in §1.5). If such an implementation is feasible, then an entire truckload of sugar cane can be analysed quickly and accurately to detect soil before the cane is transported to the mills. The scanning would probably take place at a weigh-station. In this way, since the entire truck would be analysed, the potential problem with sampling (emphasised in [5]), would be avoided.

Although *DuET* and X-ray imaging both show promise of future success, more research is anticipated before either technique can be industrialised: much effort is always expected when transferring a technique from the laboratory to industry as it requires much planning, redesign and patience. A *DuET*-system is expected to cost less than an X-ray-system to implement and maintain. With respect to *DuET*-systems that measure ash in coal, such machines cost around R 200,000[26]. On the other hand, X-ray systems, may cost about 10 to 20 times more. A *MobileSearch*-unit, due to its uniqueness on the market, costs around R 20 million (about US$ 2 million)[27].

---

[26] Private communication: James Asbury, *Scantech Limited*, j.asbury@scantech.com.au

[27] http://www.pseag.org/Resource_Document_HTML/Explosives_Detection/inspection.htm

9.2. Future Work

As mentioned in §9.1, *DuET* and X-ray imaging both require further research. The first step would be to extend the sample set to include many cane varieties and soil samples from all cane-growing regions in South Africa. Then, with respect to *DuET*, a database of calibration equations, relating *R*-values to soil concentration, can be compiled.

9.2.1. *DuET*

The most pressing issue surrounding *DuET* is the need to reduce the large variation of predicted soil concentrations, seen in **Figure 32** and **Figure 34**. Such large variation was not seen in the investigation involving ferric chloride (**Figure 29**). Therefore, effects due to scatter and incomplete volume sampling, need to be ruled out as possible causes for the large deviation.

Although it was expected that collimation in *DuET* would improve results, this could not be confirmed since stronger sources were not available (a stronger source is required since collimators reduce incident source intensity). A $10 - 20$ times stronger source is required for use with proper source-detector collimation for the *dynamic*-layout, described in §5.6. However, collimators (usually made of lead) result in increased scatter due to X-ray fluorescence. Therefore, this additional scatter must also be reduced; this could be accomplished by covering the lead with copper[28] to attenuate the emissions from *Pb*. The characteristic energies of copper are small (~ 9 keV [17]), and should not significantly contaminate the *DuET*-spectra.

It is possible to scale *DuET* up by using larger detectors, wider platforms and line sources[29] in order to analyse larger samples. In addition, integration times can be reduced by using stronger sources (however, at the expense of more shielding for

---

[28] Suggested by R.J. de Meijer, *Kernfysisch Versneller Instituut*: demeijer@kvi.nl

[29] "Line sources" possess a finite extension along a specific axis as opposed to the standard point sources, which are spherically-shaped with small diameters.

safety reasons)[30]. Therefore, *DuET* would then be able to handle a large mass of sample per analysis, in contrast to the 50 g required for the ashing method.

Monte Carlo-techniques should be applied to model *DuET* in order to optimise source strengths, shielding, sample volumes and source-detector distances.

9.2.2. *DWT-ANN*

With respect to wavelet compression, there is a need to investigate other basis functions since there may exist a basis that may perform better than *DAUB6*, which was used for the current work.

On the same note, a general method is required to identify the most suitable basis for a specific application. This will complement the *DWT-ANN* methodology, which can be applied to any type of spectrum (infra-red, gamma, X-ray fluorescence).

Spectral drift is a property of radiation detectors, where the peak positions (as seen on an *MCA*, for example) move with changes in temperature. Therefore, processing the *DuET*-spectra can become problematic if auto-stabilisation routines are not available. However, it is anticipated that the *DWT-ANN* approach would be insensitive to such drifts since only major features (and not their positions) are extracted by the *DWT* and used by the *ANN*. This assumption, however, requires more confirmation.

Finally, it is hoped to implement the *DWT-ANN* method in hardware via microprocessors.

---

[30] For the conventional *DuET*-systems using [231]*Am* and [137]*Cs*, the sources are encapsulated in stainless steel. This encapsulation is necessary to prevent environmental contamination. However, for a single-source *DuET*-system using only [137]*Cs*, the stainless steel would almost completely absorb the 32.2 keV emissions, yielding the technique unusable. A private communication with Corrie Claase (*NECSA*) revealed that their envisaged single-source *DuET*-system will use a beryllium window, which will provide source encapsulation without comprising the intensity of the 32.2 keV-line.

9.2.3. X-ray Imaging

A more comprehensive study of X-ray imaging would involve investigating the effects of various X-ray settings, including choice of target and filters, X-ray energy and exposure.

The use of *digital X-ray imaging*, where radiographic film is replaced by *CCD* [31]-technology, is expected to simplify the technique. Although radiographic film has a higher resolution than digital radiography, the digital approach may be adequate to identify soil in cane. In any case, it is impractical for an on-line application of X-ray imaging to use radiographic film.

X-ray backscatter, one of the techniques used by *MobileSearch*, should also be investigated as a method for quantifying soil in cane. Alternatively, it could be applied to solving the inverse problem, that is, determining the purity of sugar cane since the technique is suited to low-Z elements.

Another technique that may warrant investigation is *X-ray Computed Tomography* (*XCT*). Like X-ray radiography, *XCT* has its roots in medicine. The entire volume of the sample (or patient) is scanned by a moving source-detector gantry. The resulting transmission spectra (or images) are then used to construct a three-dimensional representation of the sample. Basically, this method is an extension of X-ray imaging but the arrangement is similar to that described under §5.6, the *dynamic*-layout used for *DuET*. Therefore, with respect to the soil in cane-problem, the samples can be imaged, and the soil distribution can be determined.

---

[31] Charge-coupled device

10. References

[1] Industry Directory 2000 / 2001 for the *South African Sugar Association*; 2000.

[2] Wienese, A. and Reid, M.J.; *"Soil in cane: Its measurement, its effects on milling, and methods of removal"*; Internal Report of the Sugar Milling Research Institute (*SMRI*); 1997.

[3] Mathew, P.J., Fuelling, T.G., Dow, J.C., Phillips P.L. and Noble, A.G.; *"A Soil Monitor for Sugar Cane"*; **Proceedings of 1994 Conference of Australian Society of Sugar Cane Technologists**; Pages 307-313; 1994.

[4] Bacchi, M.A. and Fernandes, E.A.N.; *"Natural radionuclides as dirt tracers in sugar cane consignments"*; **Journal of Radioanalytical and Nuclear Chemistry 235 (Nos 1-2)**; Pages 179-183; 1998.

[5] Fernandes, E.A.N. and Bacchi, M.A.; *"Nuclear and Conventional Methods for Soil Determination in Sugar Cane Industry"*; **Biological Trace Element Research**; Pages 643-648; 1994.

[6] *Ortec* Application Note (*AN34*) – *"Experiments in Nuclear Science"*; July 1971.

[7] Fernandes, E.A.N., Bacchi, M.A., Filho, V.F.N. and Simabuco, S.M.; *"X-ray fluorescence for soil characterization in shredded cane"*; **Int. Sugar Jnl.**; Vol. 97; Nos 1154E; Pages 92-95; 1995.

[8] *Berthold Industrial Systems*:
http://berthold.com.au/industrial_pages/LB420.html

[9] *Scantech Limited*: http://www.scantech.com.au/tech/let/default.htm

[10] *Nuclear Technology Products, NECSA*:
http://www.radioisotopes.co.za/products/radiation_tech.htm#Kangela

[11] Suzuki, T., Kitsutaka, R., Muto, T. and Morisaki, S.; *"Determination of the Purity of Gold Alloys Using Gamma-Ray Transmission Techniques"*; **Japanese Journal of Applied Physics 37 (Part 1)**; Pages 6242-6247; 1998.

[12] Bartle, C.M.; *"Comparison of the response of raw wool to simultaneous neutron and gamma (neugat) transmission and simultaneous dual energy γ-ray (gamgat) transmission"*; **Applied Radiation and Isotopes 50**; Pages 859-866; 1999.

[13] *Bone Measurement Institute (BMI)*:
http://www.bonemeasurement.com/hcp/technologies/dxa.html

[14] Knoll, G.F.; *"Radiation Detection and Measurement"*; John Wiley & Sons; Inc.; 1979.

[15] Berger, M.J. and Hubbell, J.H.; *"XCOM: Photon Cross Sections on a Personal Computer"*; June 1991.

[16] El-Kateb, A.H.; *"Determination of γ-spectrometric parameters for some chloride salt solutions"*; **Annals of Nuclear Energy 28**; Pages 113-124; 2001.

[17] *CRC Handbook of Chemistry and Physics* (50th edition); The Chemical Rubber Co.; 1969.

[18] Krane, K.S.; *"Introductory Nuclear Physics"*; John Wiley & Sons, Inc.; 1988.

[19] Nothnagel, G.; *"Suggestion for a program of comparative tests to evaluate the performance of the Sugela ash monitor"*; Internal *NECSA* report; 1997.

[20] Åbro, E., Khoryakov, V.A., Johansen, G.A, and Kocbach, L.; *"Determination of void fraction and flow regime using a neural network trained on simulated data based on gamma-ray densitometry"*; **Meas. Sci. Technol. 10**; Pages 610-630; 1999.

[21] Svozil, D., Kvasnička, V. and Pospíchal, J.; *"Introduction to multi-layer feed-forward neural networks"*; **Chemometrics and Intelligent Laboratory Systems 39**; Pages 43-62; 1997.

[22] Morgan, W.L., Larsen, J.T. and Goldstein, W.H.; *"The Use of Artificial Neural Networks in Plasma Spectroscopy"*; **J. Quant. Spectrosc. Radiat. Transfer**; Vol. 51; No. 1/2; Pages 247-253; 1994.

[23] Olmos, P., Diaz, J.C., Perez, J.M., Garcia-Belmonte, G., Gomez, P. and Rodellar, V.; *"Application of neural network techniques in gamma spectroscopy"*; **Nuclear Instruments & Methods in Physics Research A312**; Pages 167-173; 1992.

[24] Keller, P.E., and Kouzes, R.T.; *"Gamma Spectral Analysis via Neural Networks"*; **Nuclear Science Symposium & Medical Imaging Conference: 1994 *IEEE* Conference Record**; Vol. 1; Pages 341-345; *IEEE* Press; 1994.

[25] Press, W.H., Teukolsky, S.A., Vetterling, W.T., B.P. Flannery; *"Numerical Recipes in C: The Art of Scientific Computing"* (2nd edition); Pages 591 – 602; Cambridge University Press; USA; 1992.

[26] McNulty, C.S. and Mauze, G.; *"Applications of Wavelet Analysis for Determining Glucose Concentration of Aqueous Solutions Using NIR Spectroscopy"*; **HPL-98-63**; Hewlett-Packard Laboratories; 1998. **http://www.hpl.hp.com/techreports/98/HPL-98-53.html**

[27] Curry, T.S., Dowdey, J.E., and Murry, R.C.; *"Christensen's Introduction to the Physics of Diagnostic Radiology"* (3rd edition); Lea & Febiger; Philadelphia, 1984.

[28] Birch, R., Marshall, M., and Ardran, G.M; *"Catalogue of Spectral Data for Diagnostic X-rays"*; Pages 2, 36, 57; Hospital Physicists' Association; UK; 1979.

[29] *"Laboratory Manual for South African Sugar Factories"* (3rd edition); Pages 240-241; South African Sugar Technologists' Association; South Africa; 1985.

Appendix A: The Ashing Method

The *Ashing Method* is the current technique used by South African factories to estimate soil in cane. The following procedure was extracted directly from [29]. By considering the times listed under the experimental procedure below, the total measuring time for ashing is about 140 minutes per 50 g sample.

Estimation of Soil in Cane or Bagasse

- **General**

There is no direct method available to determine soil in cane or bagasse. The current method of estimating soil is to ash the sample and compare the ash content with the ash content of a clean sample. For this purpose certain assumptions have to be made, e.g. for clean, bone dry cane and bagasse, a value of 2 % ash can be assumed.

The sub-sample to be ashed may conveniently be taken from the SICB sample and the moisture of the sample as obtained by SICB may be used.

Apparatus: Light duty balance

Glazed vitreosil basin (400 cm^3 capacity, 62 mm deep)

Perforated lid to fit basin (made of stainless steel type 316, 0.9 mm thickness and perforated with 2 mm holes, spaced 20 mm apart)

Tongs

Muffle furnace (850 $°C^{32}$), vented to fume cupboard

Desiccator (200 mm ϕ)

- **Procedure**
  - (a) Weigh 50.00 g of sample into a clean, dry and pre-weighed basin.
  - (b) Cover the basin with the lid and put it in the muffle furnace for 10 minutes.

---

[32] The method has been recently modified such that the temperature used is 650 °C.

(c) Remove the lid from the basin and leaving the door of the furnace slightly open (ca. 10 mm) to facilitate air circulation, heat for another 35 minutes.

(d) Replace the lid on the basin, remove the basin from the furnace and cool for 2 minutes on an asbestos sheet before transferring to the desiccator for 90 minutes.

(e) Place the basin, with lid, on the balance, then remove the lid and weigh the basin plus ash.

(f) Calculate ash % sample.

- **Example**

  (a) Bagasse

Mass of bagasse	=	50.00 g
Mass of basin plus ash	=	214.61 g
Mass of basin	=	213.85 g
Mass of ash	=	0.76 g
Moisture % bagasse	=	53.00

  $$\text{Ash \% dry matter} = \frac{0.76 \times 100}{50.00 \times (100 - 53)} \times 100$$

  $$= 3.23$$

  Report as 3.2 %

  Subtract 2 % from 3.2 % to obtain soil % dry matter.

  Soil % dry matter = 3.2 - 2.0
  $$= 1.2$$

  (b) Cane

Mass of cane	=	50.00 g
Moisture % cane	=	69.52
Mass of basin plus ash	=	215.33 g
Mass of basin	=	213.84 g
Mass of ash	=	1.49

  $$\text{Ash \% dry matter} = \frac{1.49 \times 100}{50.00 \times (100 - 69.52)} \times 100$$

  $$= 9.78$$

  Report as 9.8 %

  Soil % dry matter = 9.8 - 2.0 = 7.8

Appendix B: Analysis of *DuET*-spectra in *IDL*

- **General considerations for determining peak area**[14]

After each peak in the recorded spectrum has been identified (the 32.2 keV- and 662 keV-lines of ^{137}Cs, for example), the next step is to examine the region surrounding each peak in order to determine their areas. To accomplish this task, many automated techniques have been developed. The algorithms can be sub-divided into two groups:

1. those which carry out a direct summation of the data points between specified limits; and
2. those which obtain the area from a fitted analytical function.

In either of the above approaches, the contribution due to the continuum, upon which each peak is superimposed, must be subtracted from the spectrum. The data in the channels on either side of each peak are normally used to *define* the continuum. Thereafter, a linear or quadratic function is assumed to represent an estimated continuum in the region under the peak. A channel-by-channel subtraction of the continuum then produces corrected data for the following steps.

For the first method of *direct summation*, the number of channels over which the data will be summed, must be chosen. In principle, the summation should be performed over all channels significantly above the continuum. However, in practice, it is normally limited to a given number of channels on either side of the peak centroid.

The second method is more popular: the area under the peak is obtained from an analytical fit to the points comprising the peak. Most assumed shapes involve a primary Gaussian function with a small (often exponential) additive component to represent tailing on the low-energy side of the peak (due to incomplete charge collection within the detector). The fitting is usually done by least-squares methods, and the peak area is derived from the fitting parameters.

If the effects due to the background continuum and peak tailing are not significant (or can be adequately subtracted out), then most peaks can be treated as a simple Gaussian:

$$y = y_0 \cdot exp\left[\frac{-(x - x_0)^2}{2\sigma^2}\right], \tag{37}$$

where y is the height of the Gaussian at channel x, the maximum height is denoted by y_0, the peak centroid is located at x_0 and σ is the width of the distribution.

- **Fitting peaks in *IDL***

IDL is a powerful programming language that facilitates the analysis of data due to its large library of mathematical routines. With respect to *DuET*-spectra, the information required are the areas under the low- and high-energy peaks. The standard *IDL*-routine, GaussFit, was implemented. GaussFit computes a non-linear least-squares fit to a function $f(x)$, where $f(x)$ is a linear combination of a Gaussian and a quadratic function:

$$f(x) = A_0 \cdot exp\left[-\frac{1}{2}\left(\frac{x - A_2}{A_2}\right)^2\right] + A_3 + A_4 \cdot x + A_5 \cdot x^2, \tag{38}$$

where A_0 is the height of the Gaussian, A_1 is the centroid, A_2 is the width, A_3 the constant term, A_4 the linear term and A_5 is the quadratic term.[33]

For *DuET*-spectra, GaussFit was executed to fit a Gaussian over a linear background (the quadratic term was not used). The procedure is outlined below.

1. The spectrum is smoothed using a boxcar average with a width of 11.

2. The background spectrum, recorded separately, is subtracted from the sample spectrum.

3. The low- and high-energy peak centroids are located.

4. Symmetric regions around each peak centroid are chosen.

5. The GaussFit-routine is executed for each peak.

6. The area under each peak is calculated using the fitting parameters.

The fitting of **(38)** to the low- and high-energy peaks of a typical *DuET*-spectrum are shown below in **Figure 65** and **Figure 66**, respectively.

---

[33] Obtained from the *IDL* Online Help for *IDL 5.4.*; Research Systems, Inc.; 2000.
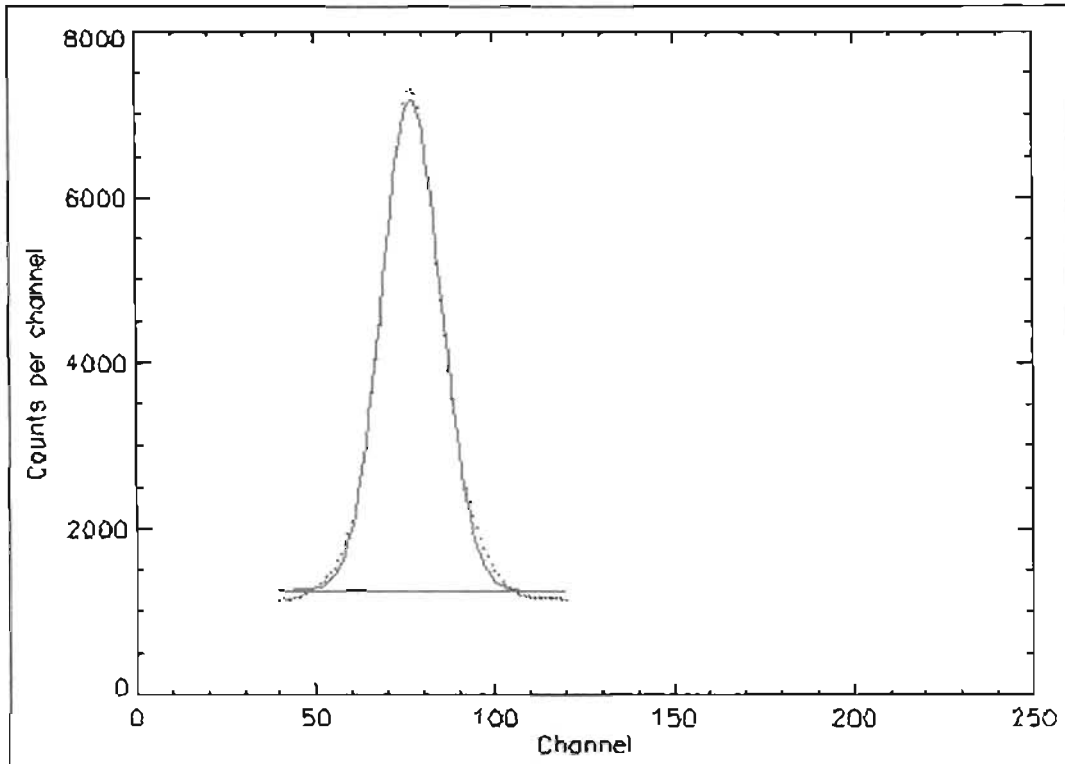
Figure 65: Fitting of a Gaussian to the low-energy peak of a typical *DuET*-spectrum. The blue dots (•) are data points, the red line (—) is the fitted Gaussian above a linear background, shown in green (—).
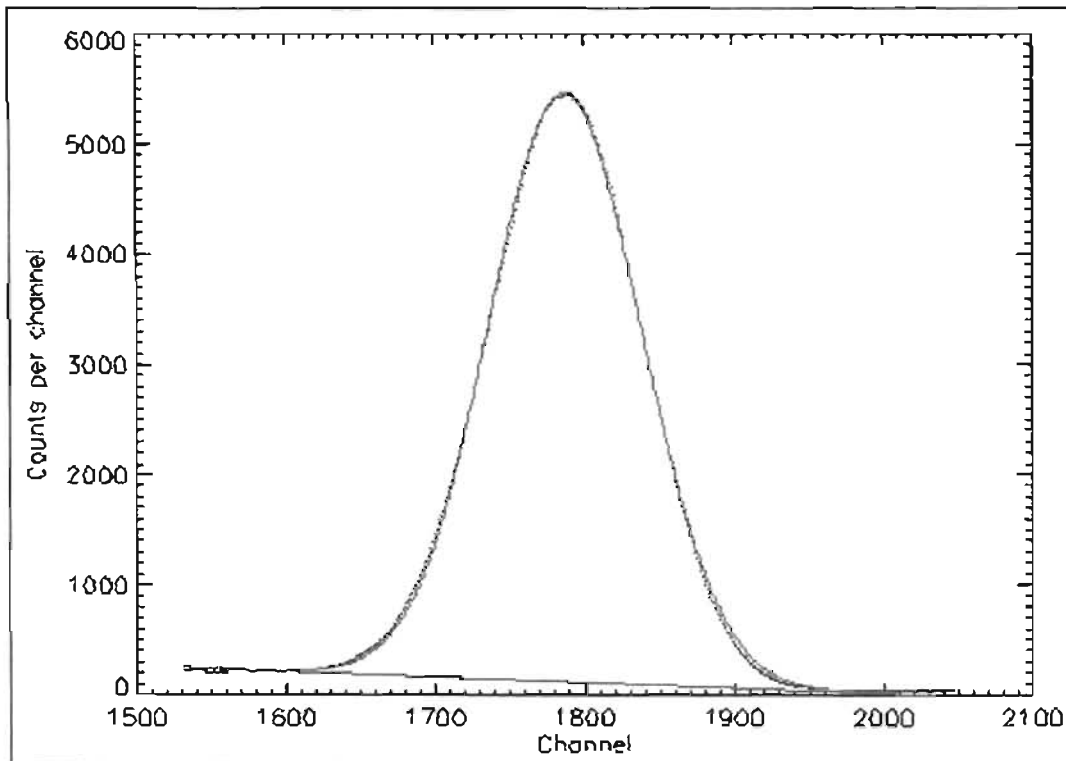
Figure 66: Fitting of a Gaussian to the high-energy peak of a typical *DuET*-spectrum. The blue dots (•) are data points, the red line (—) is the fitted Gaussian above a linear background, shown in green (—).

Appendix C: Chemical Composition of Ferric Chloride

The ferric chloride, that was used for demonstrating the principle of *DuET* (§5.3), had the following chemical composition (as provided by the manufacturer).

Name: Ferric Chloride

Formula: $FeCl_3.6H_2O$

Assay	99	%
Water-insoluble substances	0.02	%
Substances not precipitated by NH_4OH	0.1	%
Free Chloride (Cl)	0.005	%
Sulphate (SO_4)	0.01	%
Ferrous salts (Fe)	0.01	%
Heavy metals (Pb)	0.005	%

Appendix D: Data Reduction via the *DWT* in *IDL*

The major *DWT*-coefficients for the *DuET*-spectra were obtained in *IDL*; the source code is listed below.

```
function BCDtoLong, Low, Mid, High

        return, long(low mod 16) + $
                        long(ishft(low,-4))*10 + $
                        long(mid mod 16)*100 + $
                        long(ishft(mid,-4))*1000 + $
                        long(high mod 16)*10000 + $
                        long(ishft(high,-4))*100000
end

; -----------------------------------------------------------------------------

pro wv_band, y, y_out, S_coef, W_coef, comp, count

; Band filtering of the wavelet transform.

N = size(y, /n_elements)
Wy = wv_dwt(y, S_coef, W_coef, 0, 0, /double)    ; Implement wavelet transform.

i = 2
Wy2 = fltarr(N)
Wy2 [0:(2.0^i) - 1] = Wy [0:(2.0^i) - 1]

end_range = 0

while end_range lt N-1 do begin

        start_range = (2.0^i)
        end_range = (2.0^(i+1)) - 1

        level = fltarr(N)
        level [start_range:end_range] = Wy [start_range:end_range]

        ncomp = comp[i]

        sv = reverse(sort(abs(level)))
        sv_reduced = sv[0:ncomp-1 > 0]

        Wy2 [sv_reduced] = Wy [sv_reduced]

        i = i + 1

endwhile

; -----------------------------------------------------------------------------

show_recon_plot = 1

if show_recon_plot eq 1 then begin
        x = findgen(N)
        recon = wv_dwt(Wy2, S_coef, W_coef, 0, 0, /inverse, /double)

        window, 2
        plot,   x, y, /nodata, xstyle=1, xrange=[0, 250], color=0, $
                        background=255, xtitle='Channel', ytitle='Counts per channel'
        oplot, x, y, color=50
        oplot, x, recon, color=230

        window, 0
        plot,   x, y, /nodata, xstyle=1, xrange=[1000, N], color=0, $
                        background=255, xtitle='Channel', ytitle='Counts per channel'
        oplot, x, y, color=50
        oplot, x, recon, color=230

        window, 1
```

```
        plot,   x, y, /nodata, xstyle=1, xrange=[0, N], color=0, $
                    background=255, xtitle='Channel', ytitle='Counts per channel'
        oplot, x, y, color=50
        oplot, x, recon, color=230

        print, 'MSE = ', total((y - recon)^2)

endif

; --------------------------------------------------------------------------------

loc = where(Wy2 ne 0, count)
y_out = fltarr(count)
y_out = Wy2[loc]

openw, 2, 'C:\2001\IDL\Sugela\Test.txt'
printf, 2, 'Number of wavelet coefficients used for reconstruction = ', count
printf, 2, 'y'
printf, 2, format = '(f50)', y
printf, 2, 'recon'
printf, 2, format = '(f50)', recon
close, 2

end

; ================================================================================

; Main Program

t0 = systime(1)
device, decomposed=0
loadct, 39

; --------------------------------------------------------------------------------

N=2048

levels = fix(alog(N)/alog(2))
comp = fltarr(levels)

; comp = [0,0,4,8,16,32,33,0]          ; ORIGINAL

; comp = [0,0,4,4,4,8,8,0]             ; 19/9/2001 - Part 1 (36 coefficients)
; comp = [0,0,4,8,16,16,16,0]          ; 19/9/2001 - Part 2 (68 coefficients)

comp [0] = 0
comp [1] = 0
comp [2] = 4
comp [3] = 8
comp [4] = 16
comp [5] = 16
comp [6] = 16
comp [7] = 0
comp[8:levels-1] = 0

;count = fix(total(comp))

; --------------------------------------------------------------------------------

; Wavelet basis function.

;wv_fn = wv_fn_haar(1, S_coef, W_coef, 0, 0)        ; order = 1          [1]
wv_fn = wv_fn_daubechies(3, S_coef, W_coef, 0, 0)   ; order = 1, 3, 7, 8, 12 [24]
;wv_fn = wv_fn_symlet(6, S_coef, W_coef, 0, 0)      ; order = 1, 6        [15]
;wv_fn = wv_fn_coiflet(5, S_coef, W_coef, 0, 0)     ; order = 1, 5 [5]

; --------------------------------------------------------------------------------

ext = '30*.spm'

path2spm = 'C:\2001\IDL\Sugela\'                    ; Location of .SPM-data files.
path = 'C:\2001\IDL\Sugela\'                        ; Output directory.
f_name = '30_1r1.txt'

file_list = findfile(path2spm + ext, Count = count_files)
openw, 1, strcompress(path + f_name, /remove_all)
```

```
; --------------------------------------------------------------------------

for i = 0, count_files-1 do begin

        f_name = file_list[i]

        ; Reading in data from .SPM-data files.
        y = 1.0*reform(read_binary (f_name, data_start=512, data_type=3, data_dims=[1, N]))

        ; Get integration time from file.
        openr, 2, f_name
        e_time = bytarr(3)
        readu, 2, e_time
        close, 2

        elap_time = BCDtoLong(e_time(0), e_time(1), e_time(2))

        ; Execution of DWT and band-filtering of wavelet coefficients.
        wv_band, y, y_out, S_coef, W_coef, comp, count

        sample = long(strmid(f_name, strlen(path2spm), 2))

        case sample of
                6: conc = 18.87
                7: conc = 37.15
                8: conc = 22.65
                9: conc = 3.51
                10: conc = 15.68
                11: conc = 9.17
                12: conc = 16.31
                13: conc = 28.4
                14: conc = 41.94
                15: conc = 0
                16: conc = 1.55
                17: conc = 5.05
                18: conc = 6.92

                30: conc = 0.98
                37: conc = 1.91
                38: conc = 2.98
                39: conc = 5.00
                40: conc = 14.65
                68: conc = 10.35
                73: conc = 7.82
        else: print, 'Sample does not belong to ferric chloride or soil/cane set.'
        endcase

        format_str = '(f12.4,' + string(size(y_out, /n_elements)) + 'f12.4)'
        printf, 1, format = format_str, conc, y_out

        print, i+1      ; Program status counter.

endfor

close, 1

;print
print, 'I have used ', strcompress(string(count), /remove_all), ' wavelet
coefficients.'
print
print, 'Program finished in ', systime(1) - t0, ' seconds'

end
```

Appendix E: Analysis of Radiographs in *IDL*

The X-ray radiographs (recorded under §7.5.1 and §7.6.1) were analysed in *IDL*; the source code is listed below.

```
; Last update: 06 September 2001

; Notes:

;       "dev_x" represents deviation from image centre in x-direction.
;       "dev_y" represents deviation from image in y-direction.
;       "R" represents the radius of the circle to be used for the region-of-interest
;       (force "long"-type).

; -----------------------------------------------------------------------------------

t0 = systime(1)                 ; Get "start" time.

device, decomposed=0
loadct, 39

; Set program parameters.
factor = 5              ; Scaling factor to reduce image-size for viewing purposes.
log_plot = 0            ; Displays ln I vs. %Sand
zero_exterior = 1       ; Set pixels outside ROI to value of 255 (white).
apply_binary = 0
apply_log = 0           ; Take logarithm of image-data.
apply_median = 0        ; Apply median filter to image.
width = 3               ; Width for median filter.
apply_histeq = 0        ; Perform histogram equalisation on image.
norm_type = 0           ; Normalisation type.
apply_sqrt = 0          ; Take the square root of image-data.
apply_sobel = 0         ; Apply Sobel-filter to image.
apply_roberts = 0       ; Apply Roberts-filter to image.
apply_atan = 0          ; Take the arctangent of image-data.
apply_leefilt = 0       ; Apply Lee-filter to image.

; -----------------------------------------------------------------------------------

; Folder containing images to be analysed.
folder = 'C:\My Documents\Backup\2001_Support\Mammography\Images_Set_02\'

; -----------------------------------------------------------------------------------
; Output current settings to screen.
print
print, 'folder = ', folder
print, 'apply_binary =          ', apply_binary
print, 'apply_log =             ', apply_log
print, 'apply_median =          ', apply_median
print, 'width =                 ', width
print, 'apply_histeq =          ', apply_histeq
print, 'norm_type =             ', norm_type
print, 'apply_sqrt =            ', apply_sqrt
print, 'apply_sobel =           ', apply_sobel
print, 'apply_roberts =         ', apply_roberts
print, 'apply_atan =            ', apply_atan
print, 'apply_leefilt =         ', apply_leefilt
print

; -----------------------------------------------------------------------------------
; Output current settings to results-file.
get_lun, out_lun
openw, out_lun, folder + 'Results_' + strcompress (string(long(systime(1))),$
        /remove_all) + '.csv'

printf, out_lun, 'folder,', folder
printf, out_lun, 'apply_binary,', apply_binary
printf, out_lun, 'apply_log,', apply_log
printf, out_lun, 'apply_median,', apply_median
printf, out_lun, 'width,', width
```

```
printf, out_lun, 'apply_histeq,', apply_histeq
printf, out_lun, 'norm_type,', norm_type
printf, out_lun, 'apply_sqrt,', apply_sqrt
printf, out_lun, 'apply_sobel,', apply_sobel
printf, out_lun, 'apply_roberts,', apply_roberts
printf, out_lun, 'apply_atan,', apply_atan
printf, out_lun, 'apply_leefilt,', apply_leefilt
printf, out_lun
printf, out_lun, 'File, Pixels, min_roi, max_roi, R, %Sand, I'

; -----------------------------------------------------------------------------

; Read support data from data_file (contains image list with dev_x, dev_y, R)

;data_file = folder + 'Set_01.csv'
;data_file = folder + 'Set_02.csv'
data_file = folder + 'G4_6.csv'

if file_test(data_file) eq 1 then begin

    ; Get number of files to process.
        openr, in_lun, data_file, /GET_LUN

        file_counter = 0
        temp = ''

        while not(eof(in_lun)) do begin
                readf, in_lun, temp
                file_counter = file_counter + 1
        endwhile

        free_lun, in_lun

        ; --------------------------------------------------------------

        openr, in_lun, data_file, /GET_LUN

        n_files = file_counter-1      ; Subtract 1 (due to header).

        file_list = strarr(n_files)
        d = intarr(4, n_files)

        temp_file = ''
        dev_x = 0
        dev_y = 0
        R = 0
        S100 = 0

        header = ''
        readf, in_lun, header

        for i = 0, n_files-1 do begin
                readf, in_lun, format='(4(i, ":"), a9)', dev_x, dev_y, R, S100,$

                temp_file

                file_list[i] = temp_file
                d[0, i] = dev_x
                d[1, i] = dev_y
                d[2, i] = R
                d[3, i] = S100
        endfor

        free_lun, in_lun

        file_list = strcompress(file_list, /remove_all)

        start_index = 0
        end_index = n_files-1

        Sand = 1.0*d[3, *]/100
        I = fltarr(n_files)
endif else      begin
        print
        stop, 'Support file not found. Press Ctrl-R to reset.'
endelse
```

```
; -------------------------------------------------------------------------------

; Process all images.

for counter = start_index, end_index do begin

    ;print, 'Processing image # ', counter+1

        file = file_list[counter]

        dev_x = long(d[0, counter])
        dev_y = long(d[1, counter])
        R = long(d[2, counter])

        img = read_bmp(folder + file)
        siz = size(img, /dimensions)

        W = siz[0]
        H = siz[1]

        new_W = fix(1.0*W/factor)
        new_H = fix(1.0*H/factor)

    ; Co-ordinates of centre of circle.
        x0 = fix(W/2) + dev_x
        y0 = fix(H/2) + dev_y

    ; Pre-processing of image.
        if apply_median eq 1 then img = median(img, width)
        if apply_log eq 1 then img = alog(img+1)
        if apply_sqrt eq 1 then img = sqrt(abs(img))
        if apply_sobel eq 1 then img = sobel(img)
        if apply_roberts eq 1 then img = roberts(img)
        if apply_atan eq 1 then img = atan(img)
        if apply_leefilt eq 1 then img = leefilt(img, 5, 5)

    ;print, ' Pre-processing complete.'

    ; -------------------------------------------------------------------------------

    ; Get min- and max-values in ROI.

        img_min = 1.0*min(img)
        img_max = 1.0*max(img)

        if apply_binary eq 1 then begin
                img(where(img le 0.6*img_max)) = 0
                img(where(img gt 0.6*img_max)) = 255
        endif

        min_roi = img_max
        max_roi = img_min

        pixels = 0.0    ; Initialises "pixels", the number of pixels in ROI.
        sum = 0.0       ; Initialise "sum".

        for x = 0L, W-1 do begin
                for y = 0L, H-1 do begin

                        if (x-x0)^2 + (y-y0)^2 le R^2 then begin

                        ;if img[x,y] ge img_max then img[x,y] = 0
                        ; Zero out saturated pixels.

                        if img[x,y] ge max_roi then max_roi = img[x,y]
                        if img[x,y] le min_roi then min_roi = img[x,y]

                                pixels = pixels + 1
                                sum = sum + 1.0*img[x,y]

                        endif else begin
                                if zero_exterior eq 1 then img[x,y] = 255
                                ; Zero out all pixels not falling within ROI.
                        endelse

                endfor ; { y }
        endfor ; { x }
```

```
        ;print, '      Found min and max-values.'
        ;print, '      Number of pixels in ROI = ', pixels

        ; -------------------------------------------------------------------

        ; Quantify ROI.

        case norm_type of
                ; no min-max normalisation (norm_type = 0)
                0: sum = 1.0 * sum

                ; min-max normalisation type #1.
                1: sum = 1.0 * sum * max_roi

                ; min-max normalisation type #2.
                2: sum = 1.0 * sum * (max_roi - min_roi)

                ; min-max normalisation type #3.
                3: sum = 1.0 * atan(sum)

                ; min-max normalisation type #4.
                4: sum = 1.0 * alog(sum+1)

                ; min-max normalisation type #5.
                5: sum = 1.0 * sum / max_roi
endcase

        if apply_histeq eq 1 then begin
                img = hist_equal(img, minv=0.1*max_roi, maxv=max_roi, binsize=2)
                sum = total(img)
        endif

        I[counter] = 1.0*sum/pixels

        ;print, '      Completed ROI quantification.'

        ; -------------------------------------------------------------------

        window, 0, xsize=new_W, ysize=new_H, title=file
        tvscl, congrid(alog(img+1), new_W, new_H)

        print, file, ':        (pixels, min_roi, max_roi, x0, y0, R, %Sand, I) = ', $
                long(pixels), min_roi, max_roi, x0, y0, R, Sand[counter], $
                I[counter], fix(systime(1) - t0), ' seconds'

        printf, out_lun, format='(a10, a1, i0, 2(a1, f0), a1, i0, 2(a1, f0))', file,$
                ',', long(pixels), ',', min_roi, ',', max_roi, ',', R, ',',$
                Sand[counter], ',', I[counter]

        ;stop, 'Stop encountered. counter =', counter

endfor ; { counter }

free_lun, out_lun

; -------------------------------------------------------------------

if log_plot eq 1 then begin
        window, 1, title='Plot of ln I vs. %Sand'
        plot, sand, alog(I), /nodata, color=0, background=255, $
                title='ln I vs. %Sand', xtitle='%Sand', ytitle='ln I'

        oplot, sand, alog(I), color=230, psym=-5
endif else begin
        window, 1, title='Plot of I vs. %Sand'
        plot, sand, I, /nodata, color=0, background=255, $
                title='I vs. %Sand', xtitle='%Sand', ytitle='I'

        oplot, sand, I, color=230, psym=-5
endelse

print
print, format = '(a29, f10.2)', 'Total running time (s) = ', systime(1) - t0

end
```